UNCLASSIFIED

AD NUMBER
ADB008266

LIMITATION CHANGES

TO:

Approved for public release; distribution is unlimited.

FROM:

Distribution authorized to U.S. Gov't. agencies only; Test and Evaluation; AUG 1975. Other requests shall be referred to Air Force Flight Dynamics Lab., Wright-Patterson AFB, OH 45433.

AUTHORITY

AFWAL ltr 9 Mar 1984

AD *B008266*

AUTHORITY: *AFWAL Ltr, 9 Mar 84*

AFFDL-TR-75-52

EVALUATION OF INTEGRATED FLIGHT CONTROL/WEAPON DELIVERY FUNCTIONS FOR TACTICAL DATA SYSTEMS

AUGUST 1975

DDC
RECEIVED
DEC 31 1975
A

TECHNICAL REPORT AFFDL-TR-75-52
FINAL REPORT FOR PERIOD MAY 1974 — AUGUST 1975

Prepared for
AIR FORCE FLIGHT DYNAMICS LABORATORY
Air Force Systems Command
Wright-Patterson Air Force Base, Ohio 45433

NOTICE

When Government drawings, specifications, or other data
are used for any purpose other than in connection with a
definitely related Government procurement operation, the
United States Government thereby incurs no responsibility
nor any obligation whatsoever; and the fact that the govern-
ment may have formulated, furnished, or in any way supplied
the said drawings, specifications, or other data, is not to
be regarded by implication or otherwise as in any manner
licensing the holder or any other person or corporation,
or conveying any rights or permission to manufacture, use,
or sell any patented invention that may in any way be related
thereto.

Copies of this report should not be returned unless
return is required by security considerations, contractual
obligations, or notice on a specific document.

This technical report has been reviewed and is approved
for publication.

RALPH E. GUTH
Project Engineer

PAUL E. BLATT
Chief
Control Systems Development Branch
Flight Control Division
AF Flight Dynamics Laboratory

AIR FORCE - 21-11-75 - 100

REPORT DOCUMENTATION PAGE	READ INSTRUCTIONS BEFORE COMPLETING FORM

1. REPORT NUMBER 79	2. GOVT ACCESSION NO.	3. RECIPIENT'S CATALOG NUMBER
AFFDL-TR-75-52		

4. TITLE (and Subtitle)
EVALUATION OF INTEGRATED FLIGHT CONTROL/WEAPON DELIVERY FUNCTIONS FOR TACTICAL DATA SYSTEMS.

5. TYPE OF REPORT & PERIOD COVERED
Final Research and Development May 1974 to April 1975

6. PERFORMING ORG. REPORT NUMBER
D2900, MSG55221R

7. AUTHOR(s)
D. K. Eto

8. CONTRACT OR GRANT NUMBER(s)
F33(615)-74-C-3098

9. PERFORMING ORGANIZATION NAME AND ADDRESS
Hughes Aircraft Company
Culver City, California

10. PROGRAM ELEMENT, PROJECT, TASK AREA & WORK UNIT NUMBERS
AF- :2049
Task: 01
Work Unit: 05 17 2049 01

11. CONTROLLING OFFICE NAME AND ADDRESS
Air Force Flight Dynamics Laboratory
Air Force Systems Command
Wright-Patterson Air Force Base

12. REPORT DATE
August 1975

13. NUMBER OF PAGES
134   136 p.

14. MONITORING AGENCY NAME & ADDRESS(if different from Controlling Office)
HAC-Ref-D2900

15. SECURITY CLASS. (of this report)
Unclassified

15a. DECLASSIFICATION/DOWNGRADING SCHEDULE

16. DISTRIBUTION STATEMENT (of this Report)
Distribution limited to U.S. Government Agencies only; Test and Evaluation, June 1975. Other requests for this document must be referred to the Air Force Flight Dynamics Laboratory/FGL Wright-Patterson AFB, Ohio, 45433.

17. DISTRIBUTION STATEMENT (of the abstract entered in Block 20, if different from Report)
Final rept. May 74 - Aug 75,

18. SUPPLEMENTARY NOTES

19. KEY WORDS (Continue on reverse side if necessary and identify by block number)
Human factors, integrated avionics, flight data management, multimission aircraft, pilot workload, man/machine simulation, flight command functions

20. ABSTRACT (Continue on reverse side if necessary and identify by block number)
Portions of a flight command system for a single seat, multiple roll, fighter bomber were simulated in a man/machine simulation facility. The effects of various combinations of manual or automatic aircraft steering and external conditions on system performance and pilot workload were investigated. Portions of an A-7 multimode flight control system, a newly derived autopilot, and an angle rate bombing system were integrated to provide automatic

DD FORM 1473 EDITION OF 1 NOV 65 IS OBSOLETE   UNCLASSIFIED
1 JAN 73

172300

aircraft steering during final approach of an air-to-ground mission.

Conclusions reached as a result of this study indicate that integrated flight control/weapon delivery functions have the potential to improve weapon delivery performance during high stress situations (e. g. , impending air counter-attack, ground fire) by performing some pilot functions automatically.   This allows the pilot to devote more time to other hazards.

FOREWORD

This report was prepared by Hughes Aircraft Company, Culver City, California, Radar Avionics, under U.S. Air Force Contract F33(615)-74-C-9098, initiated under Project 2049, Task 01, and Work Unit 05.

The work was administered under the direction of the Control Systems Development Branch of the Flight Control Division, Air Force Flight Dynamics Laboratory, Air Force Systems Command, Wright-Patterson Air Force Base, Ohio by Ralph E. Guth (AFFDL/FGL), Project Engineer.

This report covers work performed from May 1974 to April 1975. The project was directed by D.K. Eto. The simulation facility integration was directed by J.W. Weber, with analytical support from D.W. Streuber, H.F. Eide, T.A. Bossler, and B. Ulrick. E. Streeter conducted the simulation trials.

This report was submitted by the author in April 1975.

TABLE OF CONTENTS

LIST OF ILLUSTRATIONS

LIST OF TABLES

SECTION I

INTRODUCTION

The overall objectives of the Tactical Data System program are: (a) to demonstrate the **multi-mode** aspects, capabilities, outputs, design validity and crew interface characteristics of a baseline integrated control data management system concept for single pilot, multi-role tactical aircraft projected for the 1975-85 time period; (b) to compare and document the capabilities, advantages and limitations of the baseline system with current systems in present day aircraft; (c) to evaluate those areas of the baseline system concept, which have been identified under Contract F33615-75-C-1262 as being critical to single pilot performance of the complex design mission; (d) to define unique facility requirements and recommendations for implementing integrated flight data management system concepts on the Air Force Flight Dynamics Laboratory simulation facilities; and (e) to provide design criteria to the DAIS program in the area of integrated flight control/weapon delivery steering algorithms.

To meet these objectives the efforts of this study were directed toward a design, implementation, and test of a real-time, integrated flight control/weapon delivery system simulator. The system is implemented in a cockpit mockup with active controls and displays, two digital computers, and an analog computer.

This study focuses on the air-to-ground mission; it mechanizes those functions required to realize an all-automatic weapon delivery capability and also integrates the controls, displays, and symbology required by the pilot to perform some of the air-to-ground attack functions manually. This simulation was then used to measure the pilot's relative workload when the manual/automatic boundary is moved, that is, when manual or automatic aircraft steering are provided to the pilot. In addition, a measure of the pilot's capability to perform an air-to-ground attack using a vertical situation display (VSD), head down, was taken. These simulated attacks were performed under a variety of external conditions, which provided varying pilot workload.

This simulator is an expansion of a simulator that was implemented and tested under Contract F33615-73-C-3123, completed in May 1974 (Reference 1). The present system expands the region of operability to include variable aircraft velocities, altitudes and dive angles, wind disturbances, and sensor noise. The head-down attack capability was added with FLIR or TV imagery, coordinated with aircraft motion, being presented through a VSD. The generic aerodynamic/flight control model of the earlier version was replaced by the A-7D aerodynamics and the flight path (FP) mode of the A-7D multimode flight control system model. The autopilot was modified to be able to handle nonzero wind conditions. A separate autopilot derived using optimal control techniques is available for integration. Because of budget and time constraints, the optimal autopilot was not incorporated into the simulator, but is discussed in Appendix IV.

1

Under Contract F33615-72-C-1262 completed in May 1973 (Reference 2), a baseline integrated data management system concept was developed for a single-pilot, multiple-role tactical aircraft projected for the 1975 to 1985 time period. In that study, a tentative boundary between manual and automatic operations was established for all phases of an air combat mission and a strike mission.

During the study documented in Reference 1, the benefits of automatic target tracking over manual target tracking in both system accuracy and pilot workload became so apparent that automatic tracking was made a system requirement for the present study. With target tracking, an automatic weapon release function can be implemented and is also included in the system design. Thus, manual target tracking and manual weapon release are no longer options in the present system.

The purpose of the man-in-the-loop experiments, performed in the present study, was twofold: 1) to determine the system accuracy under various conditions -- head-up and head-down, manual and automatic aircraft steering, various release conditions, and with avionic sensor noise; and 2) to determine the pilot workload-pilot performance relationship over this operating region.

The designs implemented and tested in this study represent another step in the development of a flight command core of functions and functional requirements. The impetus to the development of these functional requirements is the emergence of digital flight control and avionic systems. Digital flight control systems in aircraft, designed integrally with the aircraft aerodynamics through control-configured vehicle concepts, do not automatically ensure a superior air weapon system. The precise and variable control available to a pilot must be used intelligently and in a timely manner to realize its benefits. The means by which the new capability is exploited is the flight command system. The Tactical Data System of which the autopilot in the present study is a part, provides functions of system status, pilot assist, and automatic flight commands.

The report begins with a summary of the principal outputs, conclusions, and recommendations in Section II, followed by a description of the manned simulations and a discussion of the results (Section III), a description of the simulation hardware and software (Section IV), and concludes with recommendations of a procedural nature.

SECTION II

SUMMARY

The efforts on this study resulted in several outputs considerably different from the outputs documented in Reference 1. These are:

- A real time simulator of a single-seat multirole aircraft in an air-to-ground mode integrating two general-purpose digital computers and an analog computer with a HUD, VSD, and flight controls

- Implementation of an angle rate bombing system, simulated sensor noise, and two Kalman filters to process these noisy measurements.

- Two autopilots, an improved version of one developed for the previous study, and one derived under more generalized conditions.

- System performance measured under various external conditions, and pilot performance versus pilot workload.

The conclusions that apparently are forming from the limited amount of data that was gathered, and analyzed are:

- HUD to VSD and VSD to HUD transitions during the terminal portion of an air-to-ground attack are feasible and do not result in weapon delivery degradation.

- An autopilot function during terminal attack allows the pilot to operate from a VSD (head-down) and still maintain an external target detection performance comparable to that of a pilot operating from a HUD (head-up)

- When limited time is available to perform weapon delivery, and workload increases substantially, an autopilot function serves to improve weapon delivery performance over manually controlled flight.

- Weapon delivery performance is enhanced significantly with an autopilot flight command function when the scenario dictates that the pilot pay close attention to the possibility of air attack. Otherwise, the pilot can do the job manually as well as the autopilot.

- The presence of wind did not significantly affect manual weapon delivery performance. The autopilot performed as well as the pilot in removing the errors.

- If a pilot can detect, acquire, and lock onto a target at a range of 5 to 8 miles, by whatever means, he can deliver a free-fall weapon equally as well head-down as head-up.

3

Recommendations of a procedural nature related to the integration, test, and validation of the simulator are provided in Section V.

Several natural extensions to this effort are recommended, assuming flight test is not a practical reality, to further validate the usefulness of the autopilot flight command function for an air-to-ground mission.

- Have the pilots vary their division of attention between the lights and weapon delivery tasks but keep their attention to the total task, lights and weapon delivery, constant and fully occupied. This procedure will result in a better assessment of workload-performance relationship.

- Incorporate the newly derived autopilot into the simulator to assess its performance in reducing pilot workload.

- Transfer the simulation to a moving base simulator to assess the effect of autopilot-induced aircraft motion on pilot performance.

Additional runs are being run to further substantiate the conclusions drawn from work accomplished to date and a supplement to this report will be published to document the findings.

SECTION III
SIMULATION TESTS

3.1 PURPOSE AND OBJECTIVES

The output of the simulation tests are of two types: total system cross track miss, and pilot workoad versus pilot steering performance. The first type of data shows the impact of the flight command function on the total weapon system task, and the second is intended to clarify the benefits of the flight command function on the pilot's performance and workload. The data output format (Figure 1) shows the relationship between pilot workload and performance for an aircraft with an integrated autopilot for weapon delivery, and one without, for several external conditions. (See paragraph 3. 2.)

The current phase of the tactical data system (TDS) test program broadened the scope of the initial test series by examining the impact of several additional variables on weapon delivery performance and pilot workloads. A head-down weapon delivery capability was added to the basic head-up visual-target simulation. The no-wind condition was modified to provide a range of wind directions and velocities. More realistic conditions were provided with the addition of sensor and mechanization noise. A true air-speed regime from Mach 0.5 to 0.9 was available. The weapon delivery was performed at altitudes of 1000 and 5000 feet in both level or dive profiles. The feasibility of preprogrammed evasive maneuvers was also investigated. In addition, various combinations of these variables were simulated and evaluated.

Two features used in the previous simulation, manual target tracking and manual weapon release, were deleted from the present simulation because they are not usually a part of a modern, single seat weapon delivery system.

The impact of these variables on weapon accuracy and pilot workload during a terminal attack were evaluated in a series of test trials. An individual trial consisted of a terminal attack run initiated at a range of 8 to 9 miles and terminating with weapon release. The trials were performed by experimental test pilots experienced in air-to-ground operations and the use of advanced display and control technology.

Weapon impact accuracy was the prime indicator of mission success. External target recognition was compiled as the measure of pilot workload. Pilot initiated aircraft heading changes were also recorded, but external target recognition was judged to be a better measure of pilot workload. These data were then analyzed for individual and combinations of variables to quantify the impact of TDS features, mission, and environmental factors on overall mission performance. The overall goal is the determination of a set of design criteria which will be applicable to advanced integrated weapon/ delivery flight control systems.
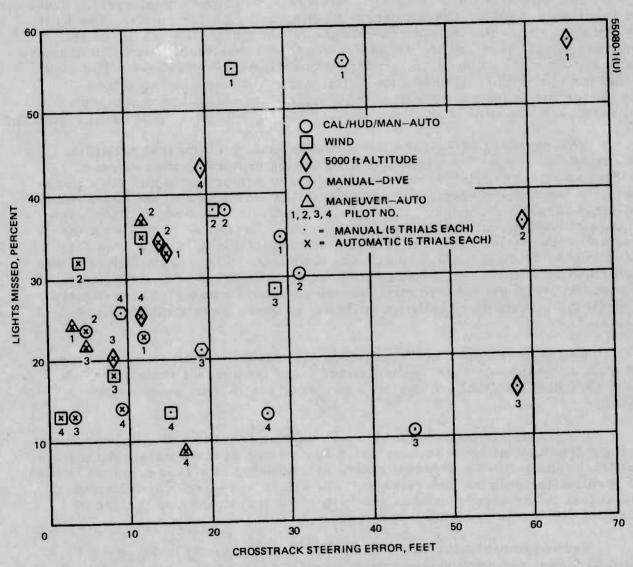
Figure 1. Pilot Workload versus Steering Performance

6

3.2 TEST DESCRIPTION

Terminal Attack Parameters

The TDS simulation of the weapon delivery phase of the fighter-bomber (F-B) mission focused on the terminal attack segment and accommodated the following operational parameters.

1) Range — The simulated attacks were initiated at approximately 8 to 9 miles from the target, or 1 minute out.

2) Airspeed — A range of speeds from Mach 0.5 to 0.9 were available for individual weapon delivery runs. Each run was flown at a constant, preselected airspeed. There was no throttle control available to the subject.

3) Flight Altitudes — The attack was initiated at altitudes of 1000 and 5000 feet. The attack was flown at either a constant altitude or through a dive maneuver. The pilot subject had normal pitch control through the flight stick.

4) Wind — The attacks were conducted in a no-wind environment or with a selected wind condition in terms of velocity or direction.

5) Ground Target — A simulated tank target was used in all attacks. Atmospheric conditions which permitted initial visual detection at a range of approximately 5 miles were assumed.

6) External Targets — Airborne targets were simulated by 20 lights positioned at the 9 through 3 o'clock positions external to the cockpit. Individual lights were illuminated randomly in terms of sequence and time interval. The lights remained on for a period of 1 second, or until extinguished by pilot trigger action. The interval between illumination of the lights was randomly varied from 1 to 5 seconds.

Previous analyses conducted under Contract F33615-72-C-1262 highlighted the criticality of the weapon delivery phase of the F-B mission to overall mission success. During this mission segment, the pilot must manage the tactical sensor, navigation, armament and ECM systems, maintain visual surveillance of potential air-to-air and ground-to-air threats, communicate with a forward air controller and other friendly aircraft, and fly the aircraft. All of these tasks must be performed while attempting to successfully deliver a weapon to a target. The combination of mission criticality and pilot task complexity prompted the selection of this mission segment for simulation and use as a framework for the evaluation of key TDS concepts.

TDS/Simulation System Features

The TDS simulation made a series of system features available to pilot subjects for the conduct of the terminal attack. Included were attack steering, flight control, weapon release, cockpit display, and maneuvering features.

7

1) Attack Steering — Two types of attack steering were provided.

    a) Computed azimuth lead (CAL) — Azimuth steering guidance directed the aircraft to a flight path and weapon release point from which the weapon would impact the target.

    b) Continuous computed impact point (CCIP) — A display presentation of the impact point of the weapon was provided.

2) Flight Control — The pilot had the option of manual flight control (pitch and bank) through a standard flight stick or autopilot flight control. In autopilot, the aircraft flies straight and level until target lockon. Following lockon, the aircraft automatically responded in the lateral direction to attack steering commands up to the point of weapon release.

3) Weapon Release — An automatic weapon release feature was provided.

4) Cockpit Displays — Two displays were provided for flight control and weapon delivery.

    a) Head-up display (HUD) — A HUD was available for simulated visual target acquisition, normal flight control, and attack steering.

    b) Vertical situation display (VSD) — A VSD was provided for simulated TV sensor acquisition of the target, flight control, and attack steering.

5) Attack Maneuvering — Automatic aircraft maneuvers were provided for use during the interval between target acquisition and weapon release when operating on autopilot.

Terminal Attack Tasks

In the conduct of the simulated terminal weapon delivery phase of the F-B mission, the following tasks were required of the pilot subject.

1) Target Sighting — A simulated ground target was presented to the pilot at a range appropriate for the acquisition technique and display device being used. If a visual attack, using the head-up display was being simulated, the target appeared at a range of approximate 5 miles. When a head-down sensor attack was being simulated, the target was presented at ranges up to a maximum of 8 miles. In both cases, the target increased in size as the aircraft approached the target.

2) Target Acquisition — The pilot designated the sighted target for tracking on either the head-up or head-down display. A designation cursor was positioned over the target and simulated sensor lockon was commanded. A finger operated force controller was provided on the throttle for positioning of the cursor and designation (lockon) of the target.

8

3) Target Tracking — Tracking of the target was performed auto-matically by a simulated TDS automatic tracking function.

4) Aircraft Steering — The pilot could fly the aircraft manually or on autopilot throughout the weapon delivery sequence. Following target lockon, weapon delivery steering information was pre-sented on the selected display. The pilot could manually fly the aircraft in response to the steering commands, or the aircraft responded automatically if autopilot had been selected.

The steering symbology, as described in Section 4, represents a minor modification to the symbology used in the initial study. Subjectively, the pilot subjects reported that the new symbology was easier to use. There was no attempt to quantify any per-formance difference between the two symbology configurations. However, since performance was virtually identical, the real impact of the change is felt to be minimal.

5) Bomb Release — Release of the simulated weapon was performed as an automatic TDS function.

6) External Target Recognition — Throughout the weapon delivery segment, the pilot was asked to maintain visual surveillance outside the cockpit. Simulated external targets in the form of lights at selected positions were illuminated periodically. The pilot responded to the light by depressing the trigger located on the control stick..

3.3 STUDY VARIABLES

The experimental program was configured to provide empirical per-formance data relative to a series of TDS features and operating environment variables. Individual variables were evaluated in an initial series of experi-mental trials. These trials were followed by additional series which exam-ined the experimental variables in combination. The basic objective through-out the entire program was that of identifying the impact of individual vari-ables and combinations of variables on weapon delivery performance and pilot workload.

Head-Up/Head-Down Weapon Delivery

The relative merits of simulated head-up (visual), head-down (sensor), and combination head-up/head-down weapon deliveries were evaluated in terms of release point accuracy and pilot workload. This portion of the pro-gram was conducted in three parts:

1) Head-Up versus Head-Down Weapon Delivery — Pilot subjects performed a series of simulated visual weapon deliveries using the HUD. These runs were conducted using CAL and CCIP guidance, and manual and autopilot aircraft steering. The HUD runs duplicated trials performed during the initial contract period and provided a basic bridge between the two study efforts that provided a basis for final evaluation of the total two-part program.

9

A second set of trials was performed head-down using a simulated TV sensor presentation on a VSD. CAL guidance and manual and autopilot steering were used.

A direct comparison of head-up and head-down performance was made in terms of release point accuracy and pilot workload as indicated by external light detection these data provide.

2) Head-Up to Head-Down Transition — The availability of both a HUD and a VSD permitted an initial investigation of the impact of transitioning from a HUD to a VSD during the course of a weapon delivery. This is a significant factor in situations where the visually acquired target passes under the nose of the aircraft prior to reaching a weapon release point. A series of trials were conducted to establish a performance tie to the full HUD or VSD run.

3) Head-Down to Head-Up Transitions — A sensor capability may provide for relatively long-range target detection. The target may appear on the VSD at ranges beyond those at which visual acquisition may be made using the HUD. Therefore, the final HUD/VSD option was that of an initial target acquisition on the VSD with a transition to the HUD for target tracking and aircraft guidance to weapon release. A final set of trials were conducted to provide data for evaluation relative to HUD, VSD, and HUD/VSD performance.

Wind Effects

The initial study series trials were conducted in a no-wind environment. The current series introduced a selected wind component to investigate the potential impact of wind on release point accuracy and pilot workload. A set of trials were performed using the HUD and CAL guidance. The factors which were varied were aircraft steering and wind. The pilot subjects flew the aircraft manually or on autopilot.

Release point accuracy and workload data were compiled for the selected wind conditions and evaluated relative to those data obtained for the earlier no-wind HUD trials.

Altitude

An increase in the altitude at which the weapon delivery is flown typically decreases the time interval available to the pilot between target acquisition and weapon release. A series of trials were directed to the evaluation of the impact on release point accuracy and workload created by raising the initial flight altitude of the weapon delivery run from 1000 to 5000 feet. Release point accuracy data were compared for 1000 and 5000 feet as was external light detection.

Complex Variables

A series of trials were conducted to evaluate release point accuracy and pilot workload under the influence of a combination of the typical

10

operational variables. Wind and altitude were combined with manual and autopilot flight control to provide an increasingly more complete operational context for the performance of the attack run. Accuracy and workload data for the complex variable runs were compared with data for the basic variable runs to identify any change in performance accruing from the buildup in operational factors.

Maneuvering

Automatic diversionary maneuvering was evaluated on a limited basis to demonstrate the feasibility of this feature in an integrated Tactical Data System. Candidate maneuvers were developed during the simulation mechanization effort. Release point accuracy and workload data are compared for nonmaneuvering and maneuvering trials to identify any degradation resulting from the addition of the maneuver.

Dive Profiles

A final series of trials were configured to provide the pilots with an opportunity to initiate a dive toward the target following lockon. The dive maneuver was manually controlled (there is no vertical component in the present guidance techniques) and is performed by nosing over the aircraft to a desired dive angle (or to the target) as dictated by the initial altitude and display/sensor capabilities.

This series is designed to demonstrate basic feasibility. High bomb dive angles are beyond the capabilities of the current simulation and may be considered for future evaluation in a flight test program.

3.4 SUBJECTS AND TRAINING

The four pilots who participated in the initial test series again served as subjects in this study. These pilots have an average of over 6000 hours flight time which includes jet air-to-ground attack experience. They are currently engaged in experimental flight test programs.

The combination of background, plus experience in the initial test series, minimized training requirements. Refresher trials were provided to bring subject performance up to the levels established in the initial program. Additional familiarization was provided in the use of the VSD, in the performance of the dive maneuver, and in the performance of the attack in wind conditions and from a 5000-foot initial altitude. Prerequisite performance standards were established as a training criteria for all subjects prior to initiating the formal test series. .

3.5 STUDY TRIALS

The experimental program consisted of a series of 300 terminal attack trials as shown in Table 1. The standard trial unit was five replications of each condition by four subjects unless otherwise noted. These trials were configured to exercise the seven study variables in the following segments.

11

TABLE 1. TDS EXPERIMENTAL TRIAL MATRIX

Study segment	Variable	Head up versus head down						HUD/VSD VSD/HUD transitions						Wind				Altitude			Maneuver	Dive	Combinations		
Guidance	CAL	X	X			X	X	X	X	X		X	X	X	X	X	X	X	X	X	X	X	X	X	X
	CCIP			X	X																				
Display	HUD	X	X	X	X			1	1	2	2		2	X	X	X	X	X	X	X	X	X	X	X	X
	VSD					X	X	2	2	1	1		1										X		
Aircraft	Manual flt control	X	X	X	X	X	X	X	X	X	X	X	X	X	X		X	X		X		X	X	X	X
	Autopilot			X	X	X	X	X	X	X	X	X	X		X	X			X		X			X	X
Wind	No wind	X	X	X	X	X	X	X	X	X	X	X	X					X	X	X	X	X	X	X	X
	Wind No. 1													X	X	X									
	Wind No. 2													X	X	X	X								
Altitude	1000 feet	X	X	X	X	X	X	X	X	X	X	X	X	X	X	X					X		X	X	X
	5000 feet																X	X	X				X	X	X
	10,000 feet																								
Airspeed	480K	X	X	X	X	X	X	X	X	X	X	X	X	X	X	X	X	X	X	X	X	X	X	X	X
	540K																								
Maneuver	Maneuver																			X					
	Dive																				X				
	Number of trials	20	20	20	20	20	20	10	10	10	10	10	10	20	20	20	20	20	20	20	20	20	10	10	10

12

1) Head-Up versus Head-Down Weapon Delivery — A total of 120 trials were performed. Wind, altitude, and airspeed were constants. Guidance, aircraft steering, and the display media will be varied.

2) HUD/VSD Transitions - 40 trials — Two subjects performed the transition tests. Guidance, wind, altitude, and airspeed were constants. Aircraft steering and display sequences were varied.

3) Wind - 40 Trials — Two wind conditions were evaluated. Guidance, display media, altitude, and airspeed were constants. Wind factors and aircraft steering were varied. Data from the CAL/HUD/no-wind trials (segment 1) were added to the test wind condition for a total evaluation unit of 80 trials.

4) Altitude - 40 Trials — Two altitudes were used. Guidance, display media, wind, and airspeed were constants. Altitude and aircraft steering were varied. Data from the CAL/HUD/ 1000-foot trials (segment 1) were added to the 5000-foot data for a total evaluation unit of 80 trials.

5) Maneuver - 20 Trials — A preprogrammed maneuver was introduced after lockon prior to weapon release. All trials were performed on autopilot with CAL/HUD/no-wind/1000 feet/480K.

6) Dive - 20 Trials — Dive attack runs were initiated from 5000 feet. They were performed under manual flight control with CAL/HUD/no-wind/480K conditions.

7) Combinations - 20 Trials — Two subjects performed the complex variable trials. Guidance and display were constant. Aircraft steering, wind, and altitude will be varied.

3.6 RECORDED DATA

The basic data configuration used in the initial study was retained for this study. Performance data was collected and recorded as an integral feature of the computer based simulation system. Four major data items were recorded.

1) Weapon Impact Accuracy — The key indicator of pilot and system performance was weapon impact accuracy.

2) Target Tracking — Manual cursor positioning actions were recorded as a pilot workload component.

3) Aircraft Steering — The number and magnitude of heading changes made by the subject in steering to the bomb release point were recorded as a second workload component.

4) External Target Detection — The number of external target lights detected by the pilot were recorded as the primary indication of pilot workload.

13

3.7 DATA ANALYSIS

The data values measured during each simulation were printed out at the end of the run. These data were also stored on magnetic tape for later data analysis.

The data were analyzed using both descriptive and inferential statistics. The descriptive statistics included means and standard deviations. Plots were made which describe the relationships between the variables investigated and the various performance measures. A major change in the measure of pilot workload occurred during the current study. An initial evaluation of pilot tracking actions and heading changes revealed that there was no consistent identifiable difference in these workload factors across the series of test conditions. However, there was a clean, statistically significant difference in the detection of external lights as a function of study variables. Therefore, the light detection measure is used as the sole criteria of pilot workload in the data analysis.

An analysis of variance was used to test the reliability of the differences in performance caused by each of the variables for the different performance measures. The Newman-Keuls sequential range test was used to test between levels of variables where three or more levels exist for a variable. Eta values were computed as an index of the practical significance of the variables for the different performance measures. Where appropriate, correlation analysis was employed to test for relationships between the different performance measures, e.g., between release point accuracy and pilot workload.

The recorded and analyzed data form the nucleus from which the results of the simulation were developed and the implications to tactical data system design established.

Head-Up versus Head-Down

Weapon delivery accuracies were virtually identical for head-up and head-down trials. All weapon delivery accuracies in this report are bomb impact accuracies in the cross-track direction only. Since along track errors for all configurations are mechanization errors independent of configuration and not dependent on pilot performance, these were left out of the comparisons in order to show more clearly the effect of different configurations and release conditions. When using the HUD, average cross track miss distances were 14.63 feet when the trial was flown manually, and 8.55 feet when operating on autopilot. When using the VSD, the average cross track miss distances were 14.0 and 8.7 feet (Table 2).

External target detection performance was influenced by operating head-down in using the VSD. As shown in Table 3, when flying manually, 19.3 percent of the lights were not detected when using the HUD. When using the VSD, the undetected lights were 30.8 percent of the total. This twofold increase was statistically significant at the 0.05 to 0.10 level (i.e., the probability of these results occurring by chance is less than 10 percent, but greater than 5 percent).

TABLE 2. HUD VERSUS VSD CROSS TRACK MISS DISTANCE (FEET)

Display	HUD		VSD	
Subject / Flight control	Manual	Automatic	Manual	Automatic
1	13.4	8.8	16.8	7.8
2	12.4	10.0	9.6	8.2
3	16..8	7.6	17.6	14.6
4	16.2	7.8	14.0	4.2
Average	14.6	8.5	14.0	8.7

TABLE 3. HUD VERSUS VSD MISSED LIGHTS

Display	HUD		VSD	
Subject / Flight control	Manual	Automatic	Manual	Automatic
1	10.8	13.4	25.0	14.4
2	12.8	14.6	13.4	17.4
3	29.6	24.4	36.6	25.2
4	24.2	23.4	48.2	38.2
Average	19.3	18.9	30.8	23.8

When operating on autopilot, the trend was visible although not statistically significant. When using the HUD, 18.9 percent of the lights were undetected, and 23.8 percent when using the VSD. It may therefore be concluded that, based on the data above, in-cockpit workloads are significantly greater when using the VSD and flying the aircraft manually. This effect is minimized when the aircraft is flown on autopilot.

HUD-VSD Transitions

A brief series of trials were conducted to demonstrate the feasibility of transitioning between the HUD and the VSD during the course of a

weapon delivery run. As shown in Table 4, when acquiring the target on the HUD and transitioning to their VSD, average cross track miss distances of 15.1 feet (manual) and 9.1 feet (autopilot) were achieved. These results were virtually identical to those achieved when flying the HUD -- 14.6 and 8.5 feet.

When initially acquiring the target on the VSD and transitioning to the HUD, slight improvements to 11.3 feet (manual) and 7.6 feet (autopilot) were realized. This is probably a result of the fact that earlier target acquisitions were made when using the VSD. The earlier acquisition made more time available for maneuvering to the release point and resulted in improved positioning at the weapon release point.

Workloads, as indicated by the number of undetected external targets (Table 5), were comparable to those experienced when using the VSD throughout the trial.

In summary, the use of both the HUD and the VSD during a weapon delivery run is feasible and compatible with the tactical data management features providing steering and flight control.

Wind

It was anticipated that the addition of a wind factor to the weapon delivery task would result in greater miss distance values and/or an increase in the percentage of external target lights that went undetected. The average miss distance values (Table 6) provided mixed results in terms of weapon delivery performance. When the trials were flown manually, average miss distance was 14.63 feet. With the addition of the wind factor, performance was virtually identical - averaging 14.85 feet. On autopilot, a significant difference (>0.001) was recorded with a no-wind average miss distance of 8.55 feet increasing to 15.8 feet with the addition of a wind factor.

The lack of a significant difference in performance when flying manually is subjectively attributable to the observation that the subjects accepted the wind condition as a challenge and simply worked harder at performing the required control actions. This contention is supported by external target detection performance (Table 7). When flying manually, an average 19.3 percent of the lights went undetected in the no-wind trials. When wind was added, 32.8 percent of the lights were not detected. This increase was statistically significant (<0.025) and indicated that the subjects were, in fact, working much harder at the basic weapon delivery task and devoting less attention to the external targets.

On autopilot, the decrease in external target detection was again evident -- 18.9 percent for the no-wind case and 24.7 percent for the trials with wind. While this difference was significant to only a limited degree (0.10 to 0.20), it was indicative of greater attention being directed to the weapon delivery task when a wind factor was present.

In summary, the presence of wind did not significantly influence weapon delivery performance. It appears that additional effort may be required to improve the steering algorithms in compensating for wind. Improved autopilot performance may also serve to reduce the pilot monitoring task and thereby reduce workload.

TABLE 4. DISPLAY TRANSITIONS – CROSS TRACK MISS DISTANCE

Miss distance (feet)		
Transition / Flight control	HUD to VSD	VSD to HUD
Manual	15.1	11.3
Autopilot	9.1	7.6

TABLE 5. DISPLAY TRANSITIONS – MISSED LIGHTS

Missed Lights (percent)		
Transition / Flight control	HUD to VSD	VSD to HUD
Manual	27.3	32.4
Autopilot	33.1	22.6

TABLE 6. WIND/NO WIND CROSS TRACK MISS DISTANCES

Average Miss Distance (feet)

Wind factor / Flight control / Subject	No wind		Wind	
	Manual	Autopilot	Manual	Autopilot
1	13.4	8.8	21.6	14.6
2	12.4	10.0	12.0	17.4
3	16.8	7.6	7.6	18.0
4	16.2	7.8	18.2	13.2
Average	14.6	8.5	14.8	15.8

TABLE 7. WIND/NO WIND MISSED LIGHTS

Missed Lights (percent)

| Wind factor | No wind | | Wind | |
Subject / Flight control	Manual	Autopilot	Manual	Autopilot
1	10.8	13.4	28.2	18.4
2	12.8	14.6	13.0	12.6
3	29.6	24.4	37.6	32.2
4	24.2	23.4	55.0	35.2
Average	19.3	18.9	32.8	24.7

Altitude

As the altitude at which the weapon delivery run is performed is increased, the time interval between a target sighting (assuming a constant detection range) and the weapon release point decreases. In theory, the pilot having less time to maneuver to the release point must maneuver more rapidly and is more likely to incur greater miss distances.

A series of trials were conducted at an altitude of 5000 feet. Average miss distance for these trials was compared with performance at the 1000-foot altitude. As shown in Table 8, when flying manually, average miss distance for the 1000-foot runs was 18.15 feet, and 28.25 feet for the 5000-foot runs. While this difference had only limited significance statistically (0.10), the full impact of the reduced operating time is reflected in the external target detection data shown in Table 9. At 1000 feet, 15.5 percent of the lights were undetected. At 5000 feet, 37.3 percent of the lights were undetected. This significant difference (<0.005) strongly indicates that the weapon delivery task is more demanding at a higher altitude such as 5000 feet when the maneuvering time is reduced.

When flying on autopilot, results were relatively uniform at both altitudes and considerably superior to flying manually in terms of miss distance. Average miss distances of 8.55 feet (1000 feet) and 10.3 feet (5000 feet) were far better than those achieved when flying manually.

These data clearly indicate that when flying manually, workloads, as measured by external target light detection, increase significantly. A major improvement in performance accuracies, when flying on autopilot, was indicated by the miss distance values which were achieved.

TABLE 8. 1000/5000 FEET – CROSS TRACK MISS DISTANCE

Miss Distance

Altitude	1000 feet		5000 feet	
Subject / Flight control	Manual	Autopilot	Manual	Autopilot
1	13.4	8.8	20.6	8.0
2	12.4	10.0	18.2	12.0
3	16..8	7.6	32.6	10.0
4	30.0	7.8	41.6	13.2
Average	18.1	8.5	28.2	10.3

TABLE 9. 1000/5000 FEET – MISSED LIGHTS

Missed Lights

Altitude	1000 feet		5000 feet	
Subject / Flight control	Manual	Autopilot	Manual	Autopilot
1	10.8	13.4	16.0	20.4
2	12.8	14.6	43.4	25.4
3	29.6	24.4	36.0	33.6
4	24.2	23.4	58.2	33.2
Average	19.3	18.9	37.3	27.7

Control/Altitude/Wind Combinations

A brief series of trials were conducted to obtain initial data on the impact of a combination of variables on performance. These trials were flown at 5000 feet with a wind component using manual and autopilot flight control. The results were virtually identical. Average miss distance for ten trials was 34.7 feet when flying manually, and 33.2 feet when flying on autopilot.

19

The more difficult conditions were also reflected in the precentages of undetected lights -- 42.9 percent when flying manually, and 30.5 percent when operating on autopilot.

The limited number of trials preclude any major conclusions. However, it appears that the more complex operating conditions will exert a definite impact on both weapon delivery performance and workload. Further refinement of the current control techniques and more extensive evaluation will be required to fully assess the extent of the impact of multiple variables.

Dive

The dive series was initiated at 5000 feet. A 10-degree dive was entered following target acquisition and maintained to the weapon release point. Steering was performed manually. Weapon release accuracy and external target detection performance was comparable to that achieved in level weapon delivery runs. As shown in Table 10, average miss distance for the dive trials was 10.65 feet which was slightly better than the 14.63 feet achieved in level runs. The undetected external target percentage of 34.8 percent for the dive trials is approximately twice that of the 19.3 percent experienced when flying level.

It therefore appears that the steering provided by the data management features will readily accommodate dive profiles with virtually no penalty in terms of weapon delivery performance. However, manual flight control during a dive maneuver will impose greater workloads throughout the run.

Maneuvering

The feasibility of preprogrammed autopilot maneuvering after lockon to the weapon release point was evaluated in a final series of trials. A preprogrammed series of maneuvers, consisting of a series of sinusoids of a 3.2-second period and maximum lateral displacement of approximately 100 feet on either side of the nonmaneuvering path, were introduced into the autopilot steering following lockon. The turns continued through the approach period until approximately 5 seconds from weapon release. At this point, the aircraft leveled out and remained level until release. The results are summarized in Table 11. The average miss distance of 5.45 feet was a slight improvement of the nonmaneuvering value of 8.55 feet. Therefore, it appears that automatic maneuvering can be considered as a viable concept which may be developed more fully as a feature of future tactical data management system configurations.

The average percentage of undetected external targets is also comparable -- 23.5 percent compared to 18.9 percent for nonmaneuvering trials. There appears to be no problem in terms of workload.

Figure 1 plots each pilot's percentage of lights missed (a measure of pilot workload) against his aircraft steering performance. All the data were taken during a CAL weapon delivery mode. The cross track error, as a result of mechanization, was removed to show just the pilot's contribution to cross track miss. The data shows that whatever the external condition, each pilot divided his attention between the lights and the weapon delivery

20

TABLE 10. LEVEL VERSUS DIVE PROFILE PERFORMANCE

Profile	Level		Dive	
Result / Subject	Cross track miss distance	Missed Lights	Cross track miss distance	Missed Lights
1	13.4	10.8	6.4	20.8
2	12.4	12.8	7.4	26.2
3	16.8	29.6	10.8	37.6
4	16.2	24.2	18.0	56.2
Average	14.6	19.3	10.6	34.8

TABLE 11. MANEUVERING TRIALS

Result / Subject	Cross track miss distance (feet)	Missed lights (percent)
1	5.6	22
2	7.4	9
3	4.6	37
4	4.2	24
Average	5.45	24

task differently. It is apparent that pilot 4 worked considerably harder or was considerably more capable than pilot 1.

A more universally useful data set could be obtained if the pilot subjects were instructed to vary their attention to the lights and weapon delivery task, but to keep their total effort constant and to be fully occupied.

It is expected that a larger number of data points (more runs) would reveal a more well-defined relationship between workload and steering performance. This presentation of the data points out the desirability of extending the experiments to achieve a better workload/performance relationship. It is only through high confidence relationships, such as these, can human factors studies have a real impact on hardware design decisions.

SECTION IV

SIMULATION SYSTEM TEST INSTALLATION

The implementation of the simulation in support of this program represented an interesting technical challenge. The scope of the simulation was increased over prior programs in this area in three ways: 1) a head-down, electro-optical sensor simulation was added to the simulation, 2) A-7 aircraft aerodynamics and flight controls were mechanized, and 3) tactical weapon delivery software was mechanized in detail and integrated with a modified autopilot to permit realistic simulation of the mission scenario over an increased flight regime and with realistic noise inputs. The challenge was not in the implementation of any one of the above-named augmentations to the previous simulation. The challenge, rather, was in the integration of a simulation that approached a hot bench facility in its level of detail and fidelity. For example, three computers (a Xerox 9300, Xerox Sigma 5, and an Applied Dynamics AD-4) were required for the complete mechanization. Problems which arose and were solved during integration were related to information transfer (accuracy, granularity, and timing) among the three computers just as they might occur in the integration of an air data computer and a tactical computer in a hot bench or an aircraft.

This section contains descriptions of the physical components of the simulation, the software, and the integration task.

4.1 MECHANIZATION

The simulation configuration for the Tactical Data System consists of several functional entities: A-7 aircraft aerodynamics and kinematics, switching and mode logic for all phases of the air-to-ground weapon delivery mission, weapon delivery computations, and the physical cockpit/experimental area. Figure 2 illustrates the relationship of these entities. The following paragraphs describe the simulation software models and the physical mechanization.

Software Models

Aerodynamics

The aerodynamic and control system simulation models represent A-7 aircraft aerodynamic and control system characteristics. The simulation consists of a linearized six-degree-of-freedom model in which the aerodynamic coefficients are assumed constant over the relatively limited flight regime required for the studies. Pitch and roll commands are derived from the flight stick. Since the simulator rudder pedals are not active, yaw control is programmed to provide coordinated turns. Figure 3 shows the lateral aerodynamics and control system mechanization. Figure 4 shows the longitudinal aerodynamics and control system mechanization. Figure 5 contains definitions of the terms used in Figures 3 and 4.

23
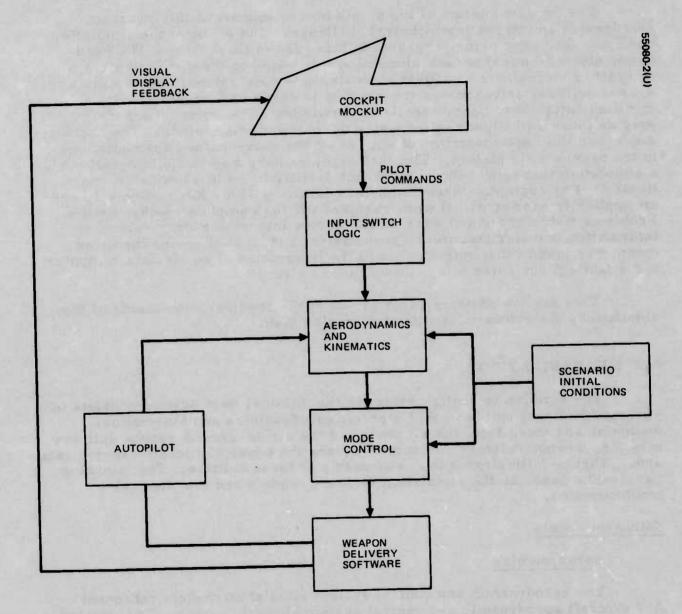
Figure 2. Functional Block Diagram

24

55080-3(U)

ROLL CONTROL

STICK FORCE

$\frac{1}{0.1S + 1}$

K_P

δ_a

p

YAW CONTROL

LATERAL ACCELERATION

$a_y = U_o \dot{\beta} - g\phi + U_o r$

$\frac{1}{0.5S + 1}$

K_r

K/S

δ_r

$\dot{\beta}$

pa

K_r

$\frac{S + 1}{(0.03S + 1)(S + 0.33)}$

Y_w β
Y_{δ_r} δ_r
Y_{δ_o} δ_a
g/U_o ϕ

$1/S$ $\dot{\beta}$ U_o v

L_β β
L_p p
L_r r
I_{xz}/I_x $\dot{r}$
L_{δ_r} δ_r
L_{δ_o} δ_a

$1/S$ $\dot{p}$ $p = \dot{\phi}$ $1/S$ ϕ

N_β β
N_p p
N_r r
I_{xz}/I_z $\dot{p}$
N_{δ_r} δ_r
N_{δ_o} δ_a

$1/S$ $\dot{r}$ $r = \dot{\psi}$ $1/S$ ψ
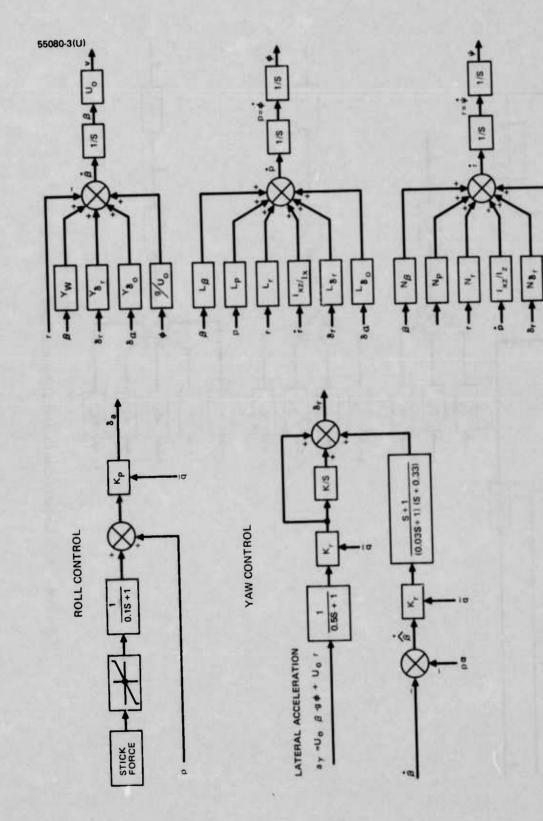
Figure 3. A-7 Lateral Control System and Aerodynamics

25

55080-4(U)
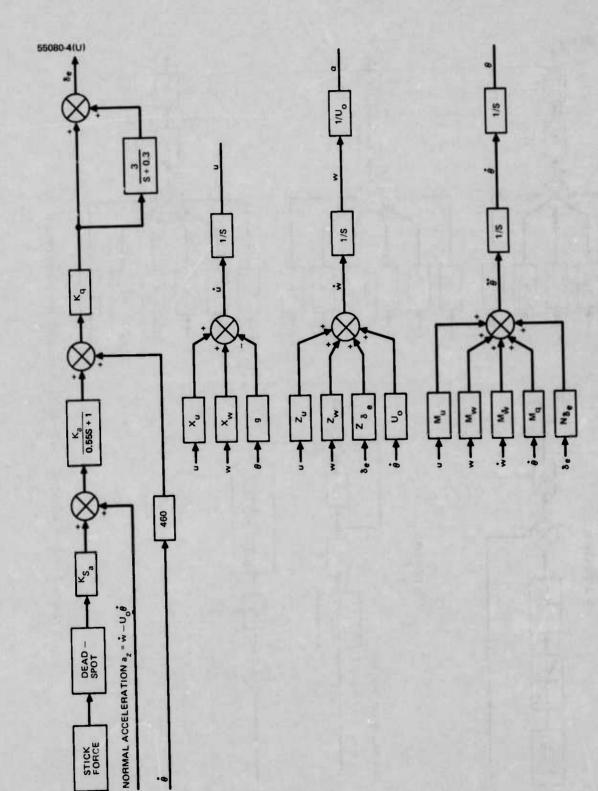
Figure 4. A-7 Longitudinal Control System and Aerodynamics

26

$\overline{V}$ = AIRCRAFT VELOCITY VECTOR

$\overline{\omega}$ = AIRCRAFT ANGULAR VELOCITY VECTOR OF THE BODY—FIXED x, y, z COORDINATE SYSTEM

$u = V_x$ = COMPONENT OF $\overline{V}$ ALONG x AXIS

$v = V_y$ = COMPONENT OF $\overline{V}$ ALONG y AXIS

$w = V_z$ = COMPONENT OF $\overline{V}$ ALONG z AXIS

$p = \omega_x$ = COMPONENT OF $\overline{\omega}$ ALONG x AXIS (ANGULAR RATE ABOUT x AXIS)

$q = \omega_y$ = COMPONENT OF $\overline{\omega}$ ALONG y AXIS (ANGULAR RATE ABOUT y AXIS)

$r = \omega_z$ = COMPONENT OF $\overline{\omega}$ ALONG z AXIS (ANGULAR RATE ABOUT z AXIS)

α = ANGLE OF ATTACK

β = ANGLE OF SIDESLIP

δ_a = AILERON DEFLECTION ANGLE

δ_r = RUDDER DEFLECTION ANGLE

δ_e = ELEVATOR DEFLECTION ANGLE

$\overline{q}$ = DYNAMIC PRESSURE $(1/2\, \rho\, V^2)$

ψ = YAW EULER ANGLE

θ = PITCH EULER ANGLE

ϕ = ROLL EULER ANGLE

x AXIS

y AXIS

z AXIS

Figure 5. A-7 Symbol Definition

27

Kinematics

Aircraft position rates in inertial coordinates are integrated to derive aircraft position and target position relative to the aircraft as a function of time. Rectangular integration with a 50 ms step size is used. Target range, range rate, azimuth and elevation angles, and angle rates are used by the weapon delivery equations and by the displays program to position and orient the target on the HUD. This information is also used to drive the television sensor simulation.

Using the definitions given in Figure 5, angular rates ($\dot{\Phi}$, $\dot{\theta}$, $\dot{\Psi}$) and translational rates ($\dot{x}$, $\dot{y}$, $\dot{z}$) were computed as shown in the following matrix equations:

$$
\begin{bmatrix} \dot{\Phi} \\ \dot{\theta} \\ \dot{\Psi} \end{bmatrix} = \begin{bmatrix} 1 & \sin\Phi\tan\theta & \cos\Phi\tan\theta \\ 0 & \cos\Phi & -\sin\Phi \\ 0 & \dfrac{\sin\Phi}{\cos\theta} & \dfrac{\cos\Phi}{\cos\theta} \end{bmatrix} \begin{bmatrix} p \\ q \\ r \end{bmatrix}
\tag{1}
$$

$$
\begin{bmatrix} \dot{x} \\ \dot{y} \\ \dot{z} \end{bmatrix} = \begin{bmatrix} \cos\Psi\cos\theta & \cos\Psi\sin\theta\sin\Phi - \sin\Psi\cos\Phi & \sin\Psi\sin\Phi + \cos\Psi\sin\theta\cos\Phi \\ \sin\Psi\cos\theta & \cos\Psi\cos\Phi + \sin\Psi\sin\theta\sin\Phi & \sin\Psi\sin\theta\cos\Phi - \cos\Psi\sin\Phi \\ -\sin\theta & \sin\Phi\cos\theta & \cos\theta\cos\Phi \end{bmatrix} \begin{bmatrix} u \\ v \\ w \end{bmatrix}
\tag{2}
$$

Switching and Mode Logic

Mode control was provided to permit selection of a number of different operating modes of the simulation:

1) Head-up display or sensor display

2) Autopilot or manual steering

3) Wind or no wind

4) High altitude or low altitude

5) Sensor track or manual pointing

6) Target acquisition command

7) Run/freeze/restart

28

Although most of the above mode control is accomplished directly from hardware switches, in some instances special logic was inserted to augment the hardwired logic. For example, even when the autopilot mode of the simulation is selected, the autopilot is not engaged until target track is achieved. This ensures that the steering signal to the autopilot is valid at the time it is engaged.

Additional logic was generated to control the lights which are a part of the visual side task. Individual lights are turned on at random intervals which belong to a uniform distribution. The lights are extinguished either by depression of the trigger on the flight stick or after a period of time which is random and independent of the "off" interval. Elapsed time between onset and extinguishing of the light is measured and recorded for each event.

The timing of the lights was modified for the present studies in an attempt to make the visual side task a better measure of pilot workload. In previous studies, the "on" time of the lights was a random variable uniformly distributed between 3 and 5 seconds. This was changed to a fixed interval of 1 second. Correspondingly, "off" times were changed from an interval of 2 to 4 seconds to one of 1 to 5 seconds. Thus, the average period of an "on-off" cycle was decreased from 7 to 4 seconds with the "on" time much shorter than before. The success of this change is demonstrated in the experimental data. The visual side task now represents a much more sensitive measure of pilot workload.

Sensor Simulation

The simulated sensor image is derived from a television scanner that is focused on a rear-illuminated transparency. Range-to-target data are used to drive a zoom lens on the optical axis of the scanner to simulate the effects of range closure. Sensor pointing angles are used to position the transparency platform in x and y, permitting slewing of the space-stabilized sensor to acquire and track the target. Acquisition is accomplished by slewing the sensor to the target using the throttle-mounted force controller and depressing the acquisition switch. If the target is within the acquisition gate, track is enabled. The location of the target on the transparency is input to the computer by selecting the "calibrate" mode and designating the target as in acquisition. Sensor (transparency platform) coordinates are thus stored for use in acquisition and track modes during simulation operation.

To provide an accurate, integral simulation, care was taken to ensure consistency of target/sensor positioning through HUD/VSD and VSD/HUD transitions as well as in the HUD and VSD modes. The coordinate transformations from earth to body coordinates and their inverse are given below:

Assume Φ and θ as defined in Figure 5 and the following definitions:

$\eta_G \epsilon_G$ - azimuth, elevation of sensor line of sight in body coordinates

α, ϵ - azimuth, elevation of sensor line of sight in earth coordinates (heading stabilized)

29

x, y, z - body axes

X, Y, Z - earth axes

Thus, in matrix notation,

$$\begin{bmatrix} u_x \\ u_y \\ u_z \end{bmatrix} = \begin{bmatrix} \cos\theta & 0 & -\sin\theta \\ \sin\theta\sin\Phi & \cos\Phi & \sin\Phi\cos\theta \\ \sin\theta\cos\Phi & -\sin\Phi & \cos\Phi\cos\theta \end{bmatrix} \begin{bmatrix} 1 \\ \tan\alpha \\ \tan\epsilon \end{bmatrix} \tag{3}$$

$$\eta_G = \tan^{-1}\frac{u_y}{u_x}$$

$$\epsilon_G = \tan^{-1}\frac{u_z}{u_x}$$

for the transformation from earth to body coordinates, and

$$\begin{bmatrix} u_x \\ u_y \\ u_z \end{bmatrix} = \begin{bmatrix} \cos\theta & \sin\theta\sin\Phi & \sin\theta\cos\Phi \\ 0 & \cos\Phi & -\sin\Phi \\ -\sin\theta & \sin\Phi\cos\theta & \cos\Phi\cos\theta \end{bmatrix} \begin{bmatrix} 1 \\ \tan\eta_G \\ \tan\epsilon_G \end{bmatrix} \tag{4}$$

$$\alpha = \tan^{-1}\frac{u_y}{u_x}$$

$$\epsilon \simeq \tan^{-1}\frac{u_z}{u_x}$$

for the transformation from body to earth coordinates.

Weapon Delivery

The weapon delivery model is predicated on the delivery of free-fall weapons against tactical targets on the ground. The components of the simulated weapon delivery system include a television sensor mounted on a stabilized platform, an air data computer (ADC), an aircraft attitude reference set (ARS), a head-up display (HUD), a sensor display, a set of weapon delivery controls, standard flight controls and instruments, and a central computer processor. In the program, sensor measurement noise

30

is simulated. The weapon delivery software includes a complete measurement data filter (Kalman Filter) to combine noisy sensor measurements and predict unknown velocities and wind speeds. The function of the weapon delivery system consists of aiding in acquiring and tracking the target in an autotrack mode. The ultimate objective is to direct the aircraft (through an autopilot) or aid a pilot in steering the aircraft to a weapon release point and trigger or enable weapon release.

The functions of the weapon delivery equations are shown in Figure 6 within the dotted lines. It can be seen that simulated noisy aircraft and sensor inputs are filtered and then processed by the angle rate bombing equations. These equations compute the bomb release time as well as an azimuth steering signal. Steering can be either automatic or manual. The optimal steering computation is used in the automatic steering mode and is discussed and derived in Appendix IV.

The changes that were made for the present simulation were in three areas: sensor error generation, Kalman filtering, and ballistics.
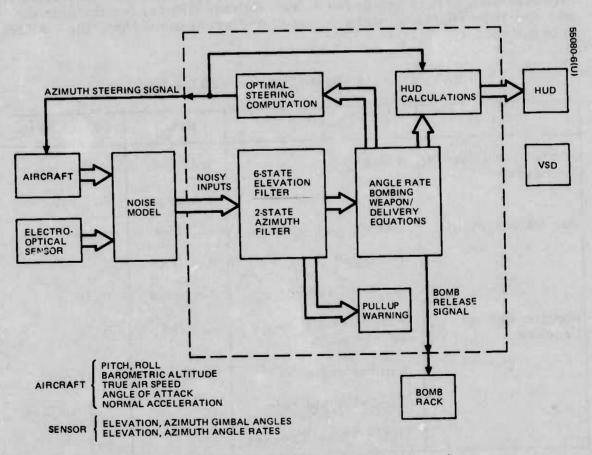

Figure 6. Diagram of Weapon Delivery Functions

31

Sensor Error Generation. Each simulated sensor measurement was assumed to have some random measurement error associated with it. For this study, all of the sensor errors were assumed to be either a bias or a wide bandwidth "white" noise. The various sensor measurements and their associated 1σ error values are shown in Table 12.

In the weapon delivery subroutine, NARBS, the bias and noise error values for each sensor measurement are generated by drawing samples from a gaussian random number generator and scaling these samples by the 1σ values listed in Table 12. The bias error values are computed only once at the beginning of a weapon delivery run and held constant for the duration of the run. The noise error values are computed once per computation cycle (50 ms) that is, every time a new measurement is made. Both error values are added to the "true" values of the measurements to produce "noisy" measurements to be processed further by the weapon delivery equations.

Kalman Filtering. In order to accurately deliver bombs in the presence of noisy sensor measurements, some sort of filtering is necessary. In the previous study, (Reference 1) filtering was omitted and "true" noise-free sensor measurements were used to compute the quantities required for an angle-rate bombing solution. In the present study, since simulated measurement errors are present, two Kalman filters, for the azimuth and elevation channels, were designed and programmed into the NARBS subroutine.

TABLE 12. ESTIMATED 1σ ERROR VALUES

Sensor	Quantity	Bias	White Noise
Altitude and Heading Reference	Pitch	1 degree	0.7 mr
	Roll	1 degree	0.7 mr
Air Data System	Barometric altitude	167 feet	8 feet
	Airspeed	8.4 fps	--
	Angle of attack	1 degree	0.7 mr
Electro-optical Tracker	Aircraft normal acceleration	0.3 fps^2	--
	Gimbal angle	1 mr	0.47 mr
	Gimbal angle rate	--	1.5 mr/sec
	Gated Video Tracker	--	0.3 mr

32

The elevation filter is a six-state extended Kalman filter. It computes four filter measurements from the available noisy sensor inputs, processes them in predictor-corrector fashion, and outputs optimal estimates of the six states. The azimuth filter is of the same form, but has only two states and two measurements. The form of the filters is shown in Appendix I.

The states used by both filters are listed in Table 13, and are defined in Figures 7 and 8.

Ballistics. In the simulation of Reference 1 vacuum bomb range and trail, (the distance that the bomb is retarded because of drag), was found by fitting a polynomial function of airspeed, altitude, and dive angle to the ballistic tables for seven representative cases. The present study used a new method requiring the storage of only two constants. The crux of this method is the use of small perturbations from vacuum ballistics. It will work for low-drag bombs at any attitude (dive, level, or climb) and with varying accuracy at any altitude and speed. While its accuracy might not be adequate for dropping actual bombs, it is quite adequate for a realistic simulation of weapon delivery. The method is discussed in Appendix II.

TABLE 13. NARBS FILTER STATES

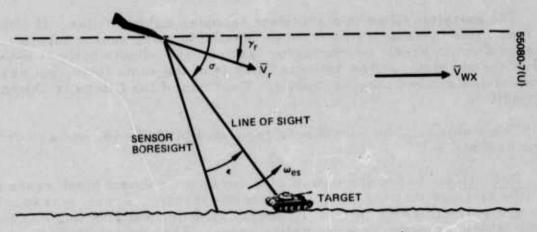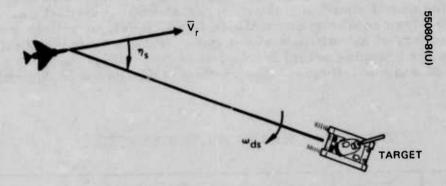| Channel	State	Description
Elevation	ω_{es}	Stabilized line of sight elevation angular rate
	σ	Angle from horizontal to line of sight
	V_r	Magnitude of aircraft velocity vector relative to target
	V_{WX}	Horizontal in plane wind/target velocity
	γ_r	Angle from horizontal to V_r
	ϵ	Elevation angle from sensor boresight to line of sight
Azimuth	η_s	Stabilized azimuth angle to line of sight
	ω_{ds}	Stabilized line of sight azimuth angular rate

33

Figure 7. Elevation Plane Geometry

Figure 8. Azimuth Plane Geometry

Autopilot

The aerodynamic simulation described earlier in this section represents a conventional airframe (the A-7) with both short period and phugoid representations. Thus, although the autopilot is ultimately used to control the flight path of the aircraft, an inner loop is required to dampen the short period mode of the aerodynamics.

The autopilot is functionally divided into longitudinal control and lateral-directional control. The altitude hold channel shown in Figure 9 was used to maintain aircraft altitude using the pitch attitude inner control loop. The altitude error is used to derive a pitch angle command. The inner loop generates elevator deflection commands as a function of the difference between commanded pitch angle and the present pitch attitude. The major difference between this model and the one used in the previous study is that the reference altitude is now defined as that existing when the autopilot is engaged. Previously, the reference value was a predefined initial condition.

The lateral channel (see Figure 10) operates on the same basic principle although several important refinements should be noted: In contrast with the autopilot used in the last study, which steered out line-of-sight errors to the target, the present autopilot operates on a steering signal generated by the weapon delivery function. Thus, the effects of wind can be included in the simulation and successful weapon deliveries can be achieved
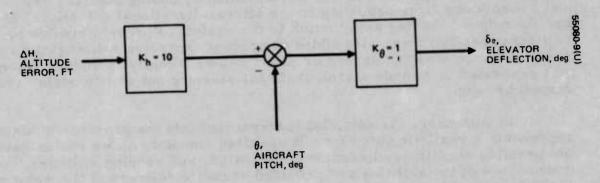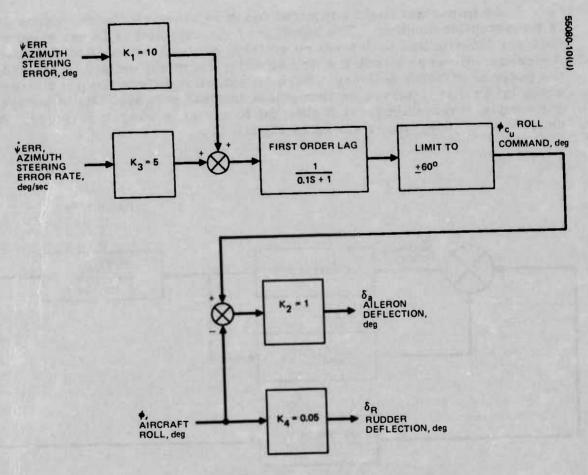
34

Figure 9. Altitude Hold Geometry

Figure 10. Lateral Directional Autopilot

35

with wind included in the simulation. Autopilot gains were increased to improve system response to steering signal inputs. To compensate for oscillations of the airframe that were introduced as a result of the increased gains, lead-lag equalization was implemented by adding steering error rate and a smoothing first-order lag in the lateral-directional autopilot. This had the effect of adding anticipation to the system to prevent overshoots. A roll command limit was also added to prevent excessive roll angles as a result of large steering errors or error rates. Finally, a rudder command was generated to provide a crab angle for steering out steady-state errors caused by wind.

In summary, the autopilot incorporated into the present simulation represents a realistic autopilot. It operated smoothly under a wide variety of operating conditions, including noise, wind, and varying altitudes. It proved free of instabilities and provided accurate delivery of the weapons to the targets. It was, therefore, consistent with one of the initial objectives of the program: to evaluate tactical data system concepts within a simulation representative of the tactical environment.

An important flight command function associated with weapon delivery is the autopilot function. The function of the autopilot is to use weapon delivery information to determine suitable aircraft orientation commands. A weapon delivery objective which an autopilot might satisfy is steering for the purpose of bomb delivery. Such an autopilot differs from a conventional autopilot in that it serves an immediate tactical purpose. Its objective is not simply to maintain level flight, but to assist in weapon delivery. A generic block diagram is shown in Figure 11.
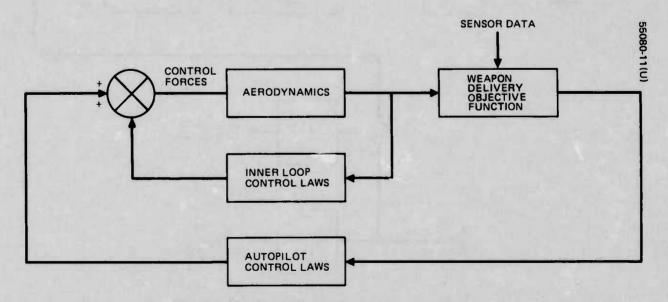

Figure 11. Tactical Autopilot Control System Block Diagram

One task of this study has been to develop an optimal autopilot control law to assist in bombing delivery. The developments are discussed in Appendix IV. Major steps included:

1) Definition of aerodynamic differential equations

2) Definition of inner loop control laws and states

3) Determination of the bombing delivery objective function

4) Synthesis

5) Discretization procedure

6) Definition of the optimal control problem

7) Solution of the matrix Riccati equation

8) Recommended control law

Equation (35) in Appendix IV is the fundamental state equation, where the aerodynamic terms are given in Appendix V.

A digital computer program is developed (Appendix IV) to discretize Equation 35 and to compute the control gains. Aileron and elevator deflection control commands are computed in terms of these gains and the 13 states. The recommended autopilot control law is contained in Equations 45 through 49.

System Executive

The use of two medium- to large-scale digital computers in the simulation dictated careful design of an executive program structure. The executive functions included master timing, analog computer mode control (for initial conditions, run, and hold), and execution of different functional software blocks in proper sequence. Figure 12 illustrates the general structure.

The Xerox 9300 computer was made the master computer and, as such, it controlled all timing and data transfers. All digital processes were interrupt scheduled. Three primary interrupts were used: two in the 9300, and one in the Sigma 5. All processes for one iteration of the simulation are initiated by the 20 Hz (50 ms) clock interrupt to the 9300. On receipt of that interrupt, the 9300 begins processing by reading the status of all external (to the computer) switches and signals and by transmitting all data required for the weapon delivery computations to the Sigma 5. Processing in the 9300 then continues by performing any switching and logic control functions, updating the geometry and dynamics, and then entering a "wait" state until data from the weapon delivery computations are ready.

When transmission of some 50 data words to the Sigma 5 has been completed (this process takes approximately 250 to 300 μs), an interrupt is generated by the data channel to the Sigma 5 processor. The data received from the 9300 includes aircraft attitude and rates. These data are used in
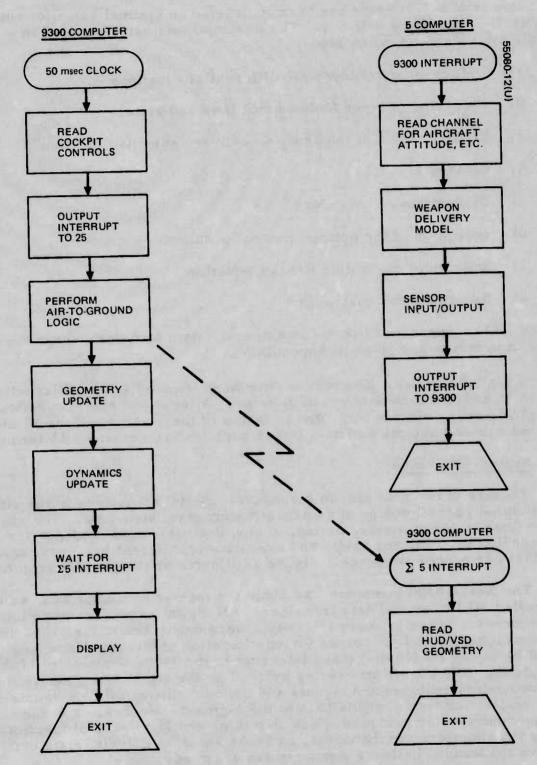
Figure 12. Executive Control of Digital Computer

38

the computation of basic weapon delivery parameters such as time-to-go and steering error. These data are transmitted back to the 9300 and the Sigma 5 returns to its "wait" state to await the next interrupt from the 9300.

On receipt of the data from the Sigma 5, the 9300 resumes processing and completes its processing for the time interval by generating and outputting a new display list to the symbol generator.

4.2 PHYSICAL DESCRIPTION

The simulation was mechanized physically using the hardware components shown in Figure 13. These physical components consist of the digital and analog computers, the cockpit mockup, the electro-optical sensor simulator, and stroke and in-raster symbol generators.

Figure 13. Hardware Configuration

39

Cockpit Mockup

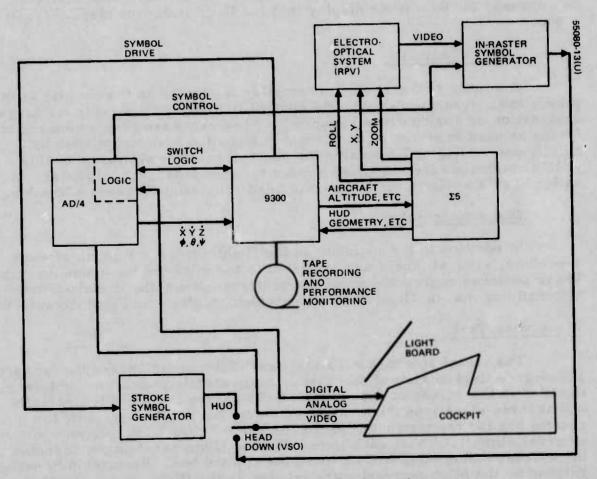The cockpit mockup used in the performance of the simulation studies is configured to represent a modern lightweight tactical fighter and is shown in Figures 14 and 15. Controls available to the pilot include a flight stick, a force controller for target designation, display mode switch, target acquisition command switch, visual side task switch, and mode control switches. All of the information required by the pilot is presented on a head-up display (HUD) or a head-down sensor display. This includes flight attitude, heading, atltitude, and weapon delivery cues.

Flight Stick

The flight stick is a spring-loaded, viscous damped, two-axis controller. It is used to control the pitch and roll attitude of the aircraft. These represent total control of the aircraft, since the rudder pedals in this simulation are inactive.

Several discrete switches are located on the flight stick. Two used in these studies are the display mode switch and the trigger. The trigger is used in performing the visual side task. The display mode switch is used to command the dual mode display into the HUD or sensor display (VSD) mode.

Force Controller

A small, two-axis force controller is located on the throttle at the pilot's left. It functions as a rate control in slewing the sensor for target designation or during manual tracking. Slew rates are proportional to the forces applied in either axis. Target designation is accomplished by axially depressing and releasing the controller. The activation of this switch commands the simulated sensor to attempt target acquisition. Activation of this switch after lockon has been achieved will cause a breaklock.

Discrete Switches

In addition to the switches on the flight stick and throttle already described, several others are available to the pilot and the experimenter. These switches control the mode of operation (automatic or manual track, automatic or manual flight control), problem restart, and altitude selection.

Visual Side Task

The visual side task uses a screen which encompasses the forward 180-degree field of view of the pilot. Independently selectable lights are mounted in the screen at approximately 30-degree intervals horizontally and at three elevations (high, middle, low). Each light is repeated in a control box for the instructor so that he can monitor pilot response to the external stimuli. Thus, each time a light is illuminated on the screen, the corresponding lamp will be lit on the control box. Each lamp is extinguished by the pilot depressing the trigger on the flight stick or by the computer after a period of time has elapsed.

Displays

Two display modes are provided in the simulation: HUD, and sensor display (VSD). These displays comprise a unique combined head-up/head-down display concept intended primarily to conserve weight, space, and power in lightweight fighter aircraft. When operating in a head-down mode, the pilot views the image on the display face directly. A shutter is closed to prevent high ambient light from entering the display from the HUD and washing it out. When switched to the HUD mode, the shutter is opened, permitting symbology generated on the cathode-ray tube (CRT) to be collimated and projected on to the HUD combining glass.

In the HUD mode, calligraphic symbology is drawn on the face of the CRT for collimation and projection onto the HUD combining glass. Calligraphic symbol generation is used to provide symbology of sufficient brightness to be easily viewed in high ambient light. In-raster symbology is mixed with the sensor imagery generated by the television sensor simulator and displayed on the VSD.

Sensor Simulation

Simulated sensor video is provided with a television scanner (TVS) which scans rear-illuminated photographic film imagery (Figure 16). Imagery used during this program simulated video from an electro-optical (TV) sensor. With suitable sensor film imagery, other sensors such as IR can also be simulated.

Closure on the target is provided with a computer-controlled, servo driven 20:1 zoom lens on the TVS. The film imagery which is scanned by the TVS is mounted in a servo-driven platform with three degrees of freedom: Y- and X- translation, and roll. The simulated sensor is space-stabilized and its boresight angle is controlled by the force controller in search mode and by the tracking system in track mode. Thus, the sensor imagery moves to reflect sensor pointing and spatial motion. The location of a target within the sensor image is correlated with its apparent position in the HUD, and vice-versa.

Symbology

Although the symbology presented in the simulation will be generated by two different means, symbology on the HUD and the sensor display is as nearly identical as possible. The following symbols are used:

1) Tracking Reticle (HUD Only) — The tracking reticle indicates the sensor line of sight on the HUD. This corresponds to the center of the sensor display presentation.

2) Reference Symbol (Sensor Display Only) — This symbol marks the center of the sensor display and provides a reference for the artificial horizon.
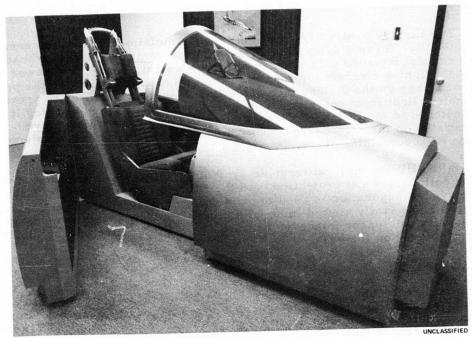
Photo 4R29880

Figure 14. Cockpit Mockup
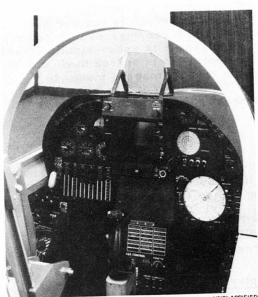
Photo 4R28995

Figure 15. Cockpit Controls
and Displays
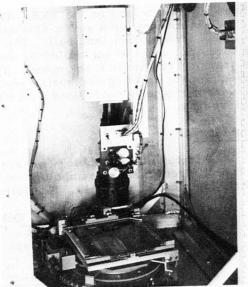
Photo 4R31374

Figure 16. Television Scanner

3) <u>Flight Path Marker (HUD Only)</u> — The flight path marker represents the direction of the velocity vector of the aircraft.

4) <u>Artificial Horizon</u> — This symbol provides an attitude reference for the pilot.

5) <u>Steering Reticle</u> — This symbol provides a steering signal to the pilot to weapon release. In one weapon delivery mode (CCIP) this symbol represents the predicted impact point of the weapon if it were released at the present instant. In the CAL mode, the steering reticle indicates the magnitude and direction of the azimuth steering error.

6) <u>Time-to-Go Symbol</u> — The length of the vertical bar of this symbol is an analog indication of the time remaining before weapon release.

7) <u>Visual Target Symbol (HUD Only)</u> — This symbol represents the spatial position of real target within the HUD field of view.

Figures 17 and 18 show typical HUD and sensor display symbology formats.

Figure 17. HUD Symbology

Figure 18. Sensor Display Symbology

43

4.3 INTEGRATION

Final integration of the simulation consisted of three separate, but not always obviously distinct, tasks: checkout of individual components of the simulation, making these components run together in real time, and verification of the accuracy of the simulation.

Initially, the programming effort was separated into two major tasks: weapon delivery computation development, and aircraft/displays/sen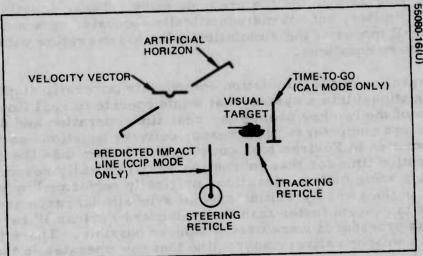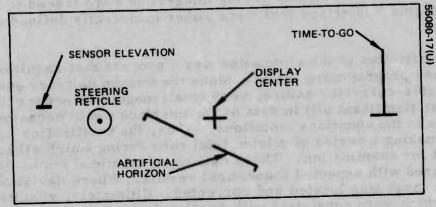sor simulation development. The weapon delivery software was developed as a subroutine which accepted aircraft data as inputs and generated weapon delivery data as outputs. Required input and output parameters were identified for transmission from/to the 9300 and scaling was defined. For early checkout, a data tape was generated by the 9300. This tape contained a time sequence of data required by the weapon delivery computations exactly as they would be received over the 9300/Sigma 5 high-speed interface. Through the use of this tape, the weapon delivery computations could be checked out in a batch mode of operation almost as if the system was on line and operating in real time. Thus, preliminary checkout was accomplished with a minimum expenditure of time and money. Preliminary checkout of the new modes of the real-time simulation (A-7 aerodynamics and electro-optical sensor) was done using the weapon delivery equations which were programmed for the previous study. These equations provided functionally similar, but not mathematically accurate, data which were used to exercise all modes of the simulation prior to integration with the complete weapon delivery equations.

Integration of the simulation components (aircraft, displays, weapon delivery equations) into a system that would operate in real time required the solution of the two key problems: real-time operation and data transfer between the two computers. The weapon delivery equations as they were originally written in Fortran took considerably longer than the 20 ms available. Execution time for that subroutine was drastically reduced by explicitly programming some matrix operations originally performed by generalized matrix subroutines and by writing special symbolic language and Fortran subroutines to execute faster than their standard Fortran library counterparts. Table lookup procedures were used whenever possible. These techniques resulted in a weapon delivery subroutine that now operates in the real-time environment.

A few minor problems during integration were traced to variables in the 9300/Sigma 5 interface that were either incorrectly defined or improperly scaled.

Verification of the simulation was a process that required mathematical analysis and programming talent. Since the weapon delivery equations were of a predictor-corrector nature, very small magnitude errors (in some cases, in the least significant bit) in data at the interface would occasionally cause divergence in the equations' solutions. Thus, the verification process consisted of making a series of piloted trial runs during which all critical data was output for examination. These data were examined frame-by-frame and compared with expected theoretical results. Where deviations were noted, the cause was located and corrected. Ultimately, results were obtained which were consistent with predicted results.

44

SECTION V

SIMULATION FACILITY RECOMMENDATIONS

The recommendations for this study are concentrated in the area of implementation — that is recommendations on procedures for system integration and checkout. They are general in nature, and if adhered to, can shorten integration time significantly. The facility recommendations from the previous study (Reference 1) are still applicable for the present expanded simulation.

The experience gained in the development and integration of the current simulation reinforces recommendations made in the previous final report. The heavy use of structured programming techniques is strongly suggested. Specifically,

1) Maintain the top-down program structure by defining, implementing, and checking out the skeleton executive first;

2) Predefine subprogram modules and arguments by function and then implement each module separately; and

3) Force early definintion (by meaning, scale, and granularity) of all global variables.

Observance of these guidelines will greatly facilitate the steps of checkout and integration.

Each subprogram module should be statically and, if possible, dynamically checked out prior to integration into the real-time simulation. This can be accomplished through the use of realistic models to generate inputs to each module. As an alternative, a tape with a time history of all pertinent data can be used for input to the module under checkout. The tape can be generated, for example, by other simulation programs in which confidence is already high. This process has the advantage of repeatability and facilitates the isolation of variables during the checkout process. It also tends to be less expensive in terms of computer resources than early checkout of subprogram modules in the real-time environment.

When integration is attempted, modules should be integrated singly. This facilitates isolation of problem areas as each new module is added. It does require that the executive skeleton execute properly alone with dummy subprogram modules. This approach takes full advantage of the top-down software structure. In many cases, it will be advantageous to return to the early checkout procedures described above to remedy problems detected and identified during integration.

SECTION VI
REFERENCES

1. Eto, D. K., Streeter, E., Weber, J. W., <u>Tactical Data Management Systems Design Concepts Evaluation</u>, Technical Report AFFDL-TR-74-53, May 1974.

2. Eto, D. K., Gunvordahl, J. W., Newman, J. B., Weihrauch, M., <u>Design Criteria for Integrated Flight Data Management Systems</u>, Technical Report AFFDL-TR-73-37, Volume II, May 1973. (C)

3. D. McRuer, I. Ashkenas, D. Graham, <u>Aircraft Dynamics and Automatic Control</u>, Systems Technology, Inc. Technical Report No. 129-1, Contract No. NOw 62-0781-c, AD859330, August 1968.

4. Meditch, J. S., <u>Stochastic Optimal Linear Estimation and Control</u>, McGraw-Hill, 1969.

5. M. Athans and P. L. Falb, <u>Optimal Control</u>, McGraw-Hill, 1966.

6. P. Dorato and A. H. Levis, "Optimal Linear Regulator: The Discrete-Time Case," <u>IEEE Trans. Automatic Control</u>, Vol. AC-16, pp. 613-620, December 1971.

7. B. D. O. Anderson and J. B. Moore, "Extensions of Quadratic Minimization Theory, II. Infinite Time Results," <u>Int. J. Contr.</u>, Vol. 7, pp. 473-480, May 1968.

APPENDIX I
AZIMUTH FILTER DERIVATION

STRUCTURE OF FILTER

The azimuth angle - angle rate filter is a discrete two state, two measurement extended Kalman filter. The flow diagram for such a filter is shown in Figure 19. The filter states are stabilized azimuth gimbal angle, η_s, and angle rate, ω_{ds}. The discrete one step predictor equations are written as:

$$\hat{\eta}_s(k+1|k) = \hat{\eta}_s(k|k) + \hat{\omega}_{ds}(k|k)\, T \tag{5}$$

$$\hat{\omega}_{ds}(k+1|k) = \hat{\omega}_{ds}(k|k) + \dot{\omega}_{ds}(k|k)\, T \tag{6}$$

where

ω_{es} = elevation angle rate
σ = elevation angle
γ_r = dive angle relative to target coordinate system
T = sample interval.
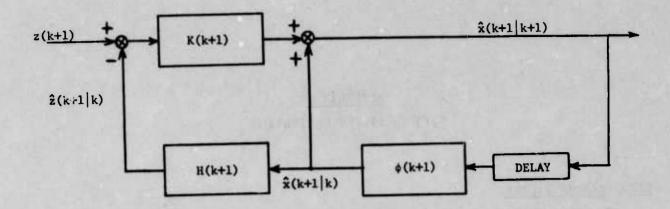
The computation of predicted measurements is simply

$$\hat{\eta}_{sm}(k+1|k) = \hat{\eta}_s(k+1|k) \tag{7}$$

$$\hat{\omega}_{dsm}(k+1|k) = \hat{\omega}_{dsm}(k+1|k) \tag{8}$$

49

z = measurement
ẑ = predicted measurement
x̂ = state estimate
K = filter gain matrix
φ = transition matrix
H = measurement matrix
k = iteration index

FIGURE 19. Kalman Filter Block Diagram

Filter Gains

The computation of filter gains for this extended Kalman filter follows the form given in the reference. The recursive equations which compute both the gain matrix K and the state covariance matrix P are:

$$P(k+1|k) = \phi(k+1|k) \, P(k|k) \, \phi^T(k+1|k) \qquad (9)$$

50

$$K(k+1) = P(k+1|k) \, H^T(k+1) \, [H(k+1) \, P(k+1|k) \, H^T(k+1) + R(k+1)]^{-1} \quad (10)$$

$$P(k+1)|k+1) = [I - K(k+1) \, H(k+1)] \, P(k+1|k) \quad\quad (11)$$

where

        P = state covariance matrix

        ϕ = state transition matrix

        K = filter gain matrix

        H = measurement matrix

        R = measurement covariance matrix.

In order to use these three equations, expressions for $\phi(k+1|k)$, $H(k+1)$, $R(k+1)$ and initial values of $P(k|k)$ are required. The linearized state transition matrix is found from equations 5 and 6 by taking partial derivatives:

$$\phi(k+1|k) = \begin{bmatrix} \dfrac{\partial \, \hat{\eta}_s(k+1|k)}{\partial \, \hat{\eta}_s(k|k)} & \dfrac{\partial \, \hat{\eta}_s(k+1|k)}{\partial \, \hat{\omega}_{ds}(k|k)} \\[4mm] \dfrac{\partial \, \hat{\omega}_{ds}(k+1|k)}{\partial \, \hat{\eta}_s(k|k)} & \dfrac{\partial \, \hat{\omega}_{ds}(k+1|k)}{\partial \, \hat{\omega}_{d_r}(k|k)} \end{bmatrix}$$

Thus

$$\phi_{11} = 1 \quad\quad\quad\quad \phi_{12} = T$$

$$\phi_{21} = 0 \quad\quad\quad\quad \phi_{22} = 1 + \frac{2\hat{\omega}_{es}(k|k)}{\tan[\hat{\sigma}(k|k) - \hat{\gamma}_r(k|k)]}$$

The measurement matrix $H(k+1)$ is simply the two dimensional identity matrix since each state is also a measurement. Thus

$$H_{11} = 1 \qquad H_{12} = 0$$

$$H_{21} = 0 \qquad H_{22} = 1$$

The measurement covariance matrix is given values corresponding to the variances of the two measurements

$$R(k+1) = \begin{bmatrix} \sigma_{\eta_s}^2 & 0 \\ 0 & \sigma_{\omega_{ds}}^2 \end{bmatrix} = \begin{bmatrix} R_{11} & 0 \\ 0 & R_{12} \end{bmatrix}$$

Similarly the state covariance matrix is initialized as

$$P(0|0) = \begin{bmatrix} P_{11} & 0 \\ 0 & P_{22} \end{bmatrix}$$

Substituting the above quantities into equations 9, 10, and 11 yields the filter gain equations:

$$P_{11}(k+1|k) = P_{11}(k|k) + 2TP_{12}(k|k) + T^2 P_{22}(k|k)$$

$$P_{12}(k+1|k) = P_{21}(k+1|k) = \phi_{22}[P_{12}(k|k) + T P_{22}(k|k)]$$

$$P_{22}(k+1|k) = \phi_{22}^2 P_{22}(k|k)$$

$$\Delta = [P_{11}(k+1|k) + R_{11}] * [P_{22}(k+1|k) + R_{22}] - P_{12}^2(k+1|k)$$

$$K_{11}(k+1) = \{P_{11}(k+1|k) \ [P_{22}(k+1|k) + R_{22}] - P_{12}^{2}(k+1|k)\}/\Delta$$

$$K_{12}(k+1) = P_{12}(k+1|k) \ R_{11}/\Delta$$

$$K_{21}(k+1) = P_{12}(k+1|k) \ R_{22}/\Delta$$

$$K_{22}(k+1) = \{- P_{12}^{2}(k+1|k) + P_{22}(k+1|k) \ [P_{11}(k+1|k) + R_{11}]\}/\Delta$$

$$P_{11}(k+1|k+1) = P_{11}(k+1|k) \ [1 - K_{11}(k+1)] - P_{12}(k+1|k) \ K_{12}(k+1)$$

$$P_{12}(k+1|k+1) = P_{21}(k+1|k+1) = P_{12}(k+1|k) \ [1 - K_{11}(k+1)] - P_{22}(k+1|k) \ K_{12}(k+1)$$

$$P_{22}(k+1|k+1) = P_{22}(k+1|k) \ [1 - K_{22}(k+1)] - P_{12}(k+1|k) \ K_{21}(k+1)$$

APPENDIX II

NEW BALLISTICS COMPUTATIONS

An excellent representation of low drag bomb ballistics can be obtained with the storage of just two constants. This algorithm actually represents a simplification of the previous ballistic computations. While its accuracy might not be adequate for dropping actual bombs, it is quite adequate for simulation purposes. It works at any attitude (dive, level, or climb) and with varying accuracy at any altitude and speed.

The crux of this method is the use of small perturbations from vacuum ballistics. In a typical dive vacuum geometry (Figure 20), the no-wind range (X_{Bo}) and time of fall (T) can easily be found from:

$$H = V_{Az} T + D$$

$$D = \frac{1}{2} g T^2$$

$$\frac{1}{2} g T^2 - V_{Az} T - H = 0$$

$$T = \frac{-V_{Az} - \sqrt{V_{Az}^2 - 2gH}}{g}$$

and

$$X_{Bo} = V_{Ax} T$$

55
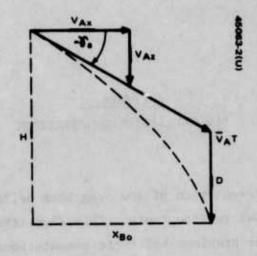
FIGURE 20. Vacuum Ballistic Geometry

It has now been found that excellent representation of the ground range of a low drag bomb can be obtained over a surprisingly wide range of operating conditions simply by multiplying gravity by a constant, K_g, slightly larger than 1. Then

$$D = \frac{1}{2} K_g g T^2$$

$$T = \frac{-V_{Az} + \sqrt{V_{Az}^2 + 2 K_g g H}}{K_g g}$$

and again

$$X_{Bo} = V_{Ax} T$$

For example, an M-117 bomb has been fit from 360 to 560 knots, 0 to 60 degrees dive and altitudes of 1,000 to 7,000 feet. K_g was found to be 1.10 to minimize the error in elevation angular rate, whose rms value worked out to be 0.34 mr/sec.

The value of T obtained in this approximation is always somewhat lower than true T_F (time of fall). While this in itself might not be important, the use of $T_F = T$ would cause the computed trail, L, to be zero. This in turn would cause cross-trail to be zero, so that when cross-winds are entered into the system, the steering would be unrealistic. The pilot would always be commanded to point his ground track at the target rather than slightly upwind of it. Therefore, a realistic T_F is required to give pilots a realistic feel of the steering problem.

This is quite easily accomplished by the use of a second constant, again slightly greater than unity:

$$T_F = K_T T$$

While the proper value of K_T might vary from 1.02 to 1.10 over the region of interest for an M-117, the use of some median value will always insure a trail in the proper direction.
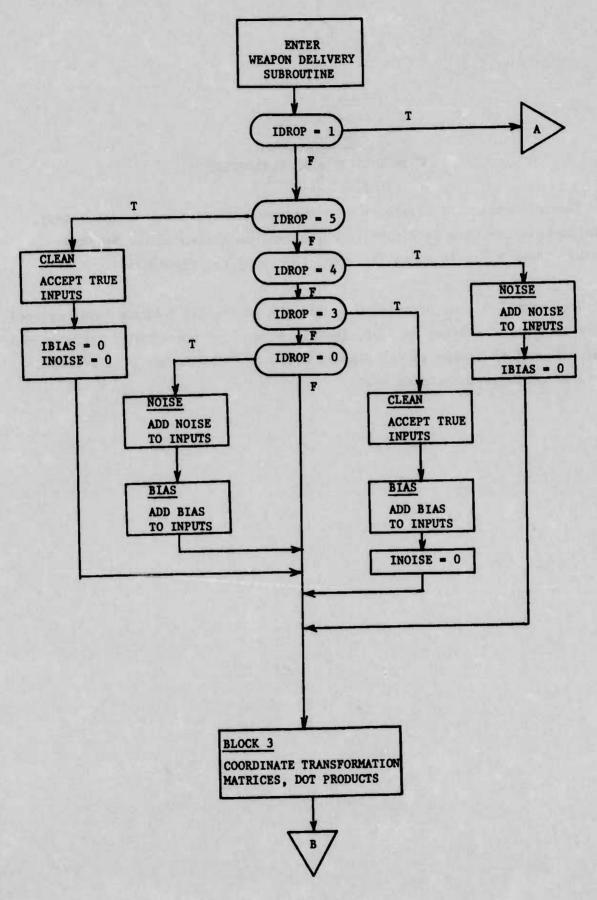
Thus, extension of the operating conditions and the avoidance of setting in nominal values for altitude and time of fall can readily be accomplished for low drag bombs. If and when high drag bombs are required, this solution will no longer be adequate. A choice will have to be made between polynomial fits (which are available for a large number of bombs at Hughes), or real-time integration. An excellent algorithm is available for the latter, but it would add considerably to the computer memory and execution time requirements.

57
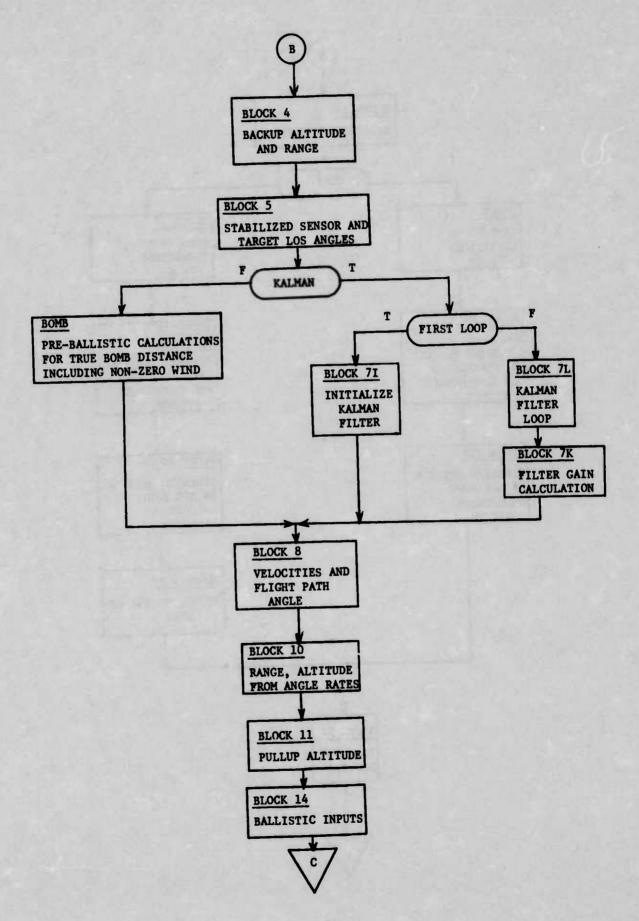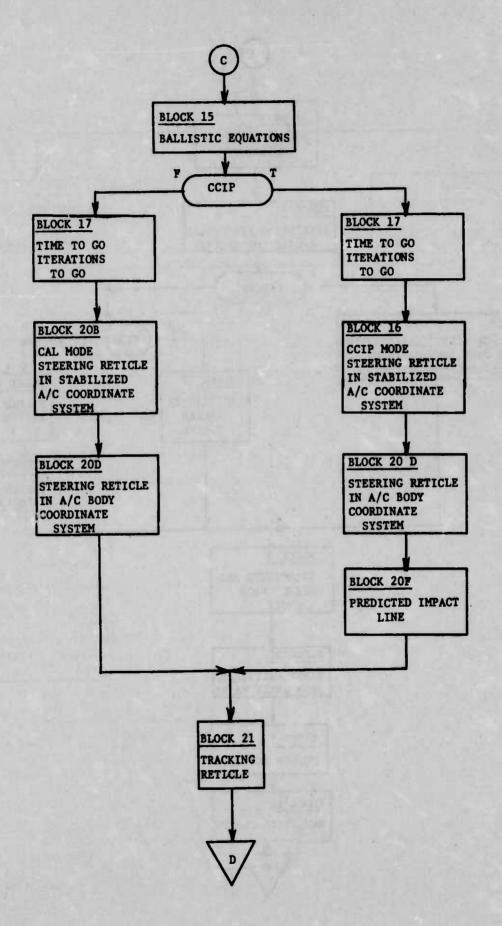
APPENDIX III
FLOWCHART OF ARBS SUBROUTINE
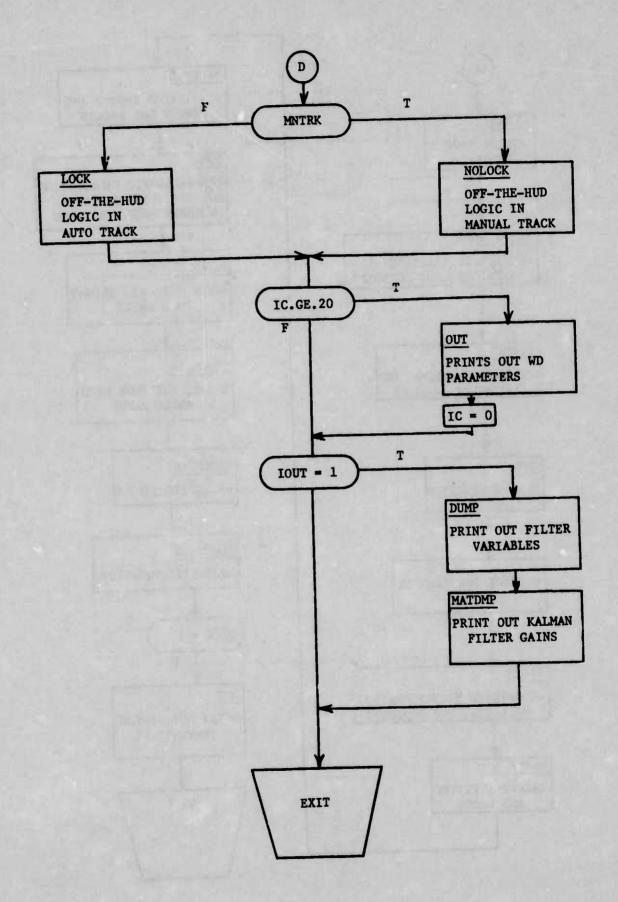
The following is a flowchart of the weapon delivery subroutine (ARBS). Each block in the flow is titled to correspond to titles in the FORTRAN listing. Each block is shown in detail following the flowchart.
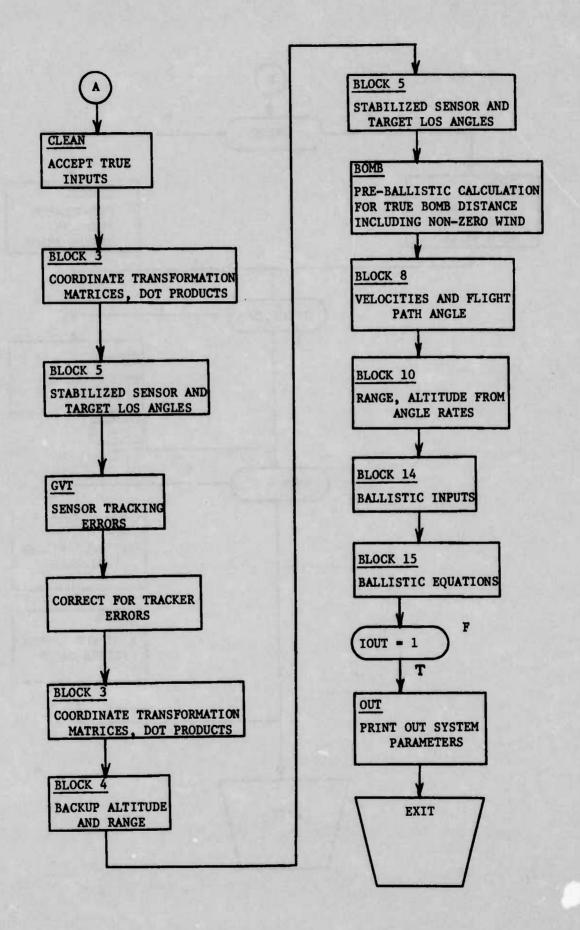
The execution time of this subroutine including all computations required by the two Kalman filters is approximately 40 msec on the Sigma-5 computer and about one half that time on the Sigma-8 computer. The former time is within the 45 msec simulation timing goal.

ENTER
WEAPON DELIVERY
SUBROUTINE

IDROP = 1 — T → A

F

T → IDROP = 5

F

CLEAN
ACCEPT TRUE
INPUTS

IDROP = 4 — T → NOISE
ADD NOISE
TO INPUTS

F

IBIAS = 0
INOISE = 0

IDROP = 3 — T

F

IBIAS = 0

T → IDROP = 0

F

NOISE
ADD NOISE
TO INPUTS

CLEAN
ACCEPT TRUE
INPUTS

BIAS
ADD BIAS
TO INPUTS

BIAS
ADD BIAS
TO INPUTS

INOISE = 0

BLOCK 3
COORDINATE TRANSFORMATION
MATRICES, DOT PRODUCTS

B

60

61

63

GVT

Computes sensor's target tracking error

$$\epsilon_{ms} = \epsilon_{true} - \epsilon_s$$

$$\eta_{ms} = \eta_{true} - \eta_s$$

$$\epsilon_m = \epsilon_{ms} \cos \rho + \eta_{ms} \sin \rho$$

$$\eta_m = - \epsilon_{ms} \sin \rho + \eta_{ms} \cos \rho$$

CLEAN

Sets the noisy measurements (denoted with an X as the first letter) equal to the true or "clean" values of the measurements, i.e.,

$$XTHETA = THETA$$
$$XPHI = PHI$$
$$\cdot$$
$$\cdot$$
$$\cdot$$
$$\cdot$$
$$\cdot$$
$$etc.$$

NOISE

Adds gaussian random noise to the clean measurements. The zero mean unity variance random numbers are stored in an array RANDOM.

$$XTHETA = THETA + SIG1 * RANDOM \ (IRAND + 1)$$
$$\vdots$$
$$XOMGDM = OMGDM + SIG13 * RANDOM \ (IRAND + 13)$$
$$IRAND = IRAND + 13$$

BIAS

Add a bias to each measurement which remains constant during the course of one entire run.

BLOCK 3

Computes the following coordinate transformation matrices: [Platform/Body], [Body/LOS], [Platform/LOS] denoted by M1, M2, and M3 respectively. These matrices are defined by the following equations:

$$
\begin{bmatrix} \bar{i} \\ \bar{l} \\ \bar{k} \end{bmatrix} =
\begin{bmatrix} C\theta & 0 & -S\theta \\ S\theta S\phi & C\phi & C\theta S\phi \\ S\theta C\phi & -S\phi & C\theta C\phi \end{bmatrix}
\begin{bmatrix} \bar{X} \\ \bar{Y} \\ \bar{Z} \end{bmatrix} = M1 \begin{bmatrix} \bar{X} \\ \bar{Y} \\ \bar{Z} \end{bmatrix}
$$

$$
\begin{bmatrix} \bar{i}_R \\ \bar{i}_E \\ \bar{i}_D \end{bmatrix} =
\begin{bmatrix} C\eta_g C\epsilon_g & S\eta_g C\epsilon_g & -S\epsilon_g \\ -S\eta_g & C\eta_g & 0 \\ C\eta_g S\epsilon_g & S\eta_g S\epsilon_g & C\epsilon_g \end{bmatrix}
\begin{bmatrix} \bar{i} \\ \bar{j} \\ \bar{k} \end{bmatrix} = M2 \begin{bmatrix} \bar{i} \\ \bar{j} \\ \bar{k} \end{bmatrix}
$$

$$
\begin{bmatrix} \bar{i}_R \\ \bar{i}_E \\ \bar{i}_D \end{bmatrix} =
\begin{bmatrix} C\eta_g C\epsilon_g & S\eta_g C\epsilon_g & -S\epsilon_g \\ -S\eta_g & C\eta_g & 0 \\ C\eta_g S\epsilon_g & S\eta_g S\epsilon_g & C\epsilon_g \end{bmatrix}
\begin{bmatrix} C\theta & 0 & -S\theta \\ S\theta S\phi & C\phi & C\theta S\phi \\ S\theta C\phi & -S\phi & C\theta C\phi \end{bmatrix}
\begin{bmatrix} \bar{X} \\ \bar{Y} \\ \bar{Z} \end{bmatrix} = M3 \begin{bmatrix} \bar{X} \\ \bar{Y} \\ \bar{Z} \end{bmatrix}
$$

BLOCK 4

Computes backup altitude above target and backup range.

$$H_b = H_p - H_T$$

$$R_b = H_b/M3(1,3) = H_b/(\bar{I}_R \cdot \bar{Z})$$

BLOCK 5

Computes stabilized line of sight angles in elevation and azimuth as well as the display rotation angle, ρ.

$$\sin \epsilon_s = - M3(1,3) = - (\bar{I}_R \cdot \bar{Z})$$

$$\cos \epsilon_s = (1 - \sin^2 \epsilon)^{1/2}$$

$$\epsilon_s = \tan^{-1}[\frac{\sin \epsilon_s}{\cos \epsilon_s}]$$

$$\sin \eta_s = M3(1,2)/\cos \epsilon_s = (\bar{I}_R \cdot \bar{Y})/\cos \epsilon_s$$

$$\cos \eta_s = M3(1,1)/\cos \epsilon_s = (\bar{I}_R \cdot \bar{X})/\cos \epsilon_s$$

$$\eta_s = \tan^{-1}[\frac{\sin \eta_s}{\cos \eta_s}]$$

$$\sin \rho = M3(3,1) \sin \eta_s - M3(3,2) \cos \eta_s$$

$$= (\bar{I}_D \cdot \bar{X}) \sin \eta_s - (\bar{I}_D \cdot \bar{Y}) \cos \eta_s$$

$$\cos \rho = M3(2,2) \cos \eta_s - M3(2,1) \sin \eta_s$$

$$= (\bar{I}_E \cdot \bar{Y}) \cos \eta_s - (\bar{I}_E \cdot \bar{X}) \sin \eta_s$$

BLOCK 7I

Initializes the elevation and azimuth Kalman filters during the first iteration of the NARBS subroutine.

Initial Predicted Values of States

$$\hat{\omega}_e(k+1|k) = \frac{V_a[\cos(\eta_g + \eta_m)\sin(\varepsilon_g + \varepsilon_m) + \alpha\cos(\varepsilon_g + \varepsilon_m)]}{R_b}$$

$$\hat{\omega}_d(k+1|k) = \frac{V_a \sin(\eta_g + \eta_m)}{R_b}$$

$$\hat{\omega}_{es}(k+1|k) = \hat{\omega}_e(k+1|k)\cos\rho - \hat{\omega}_d(k+1|k)\sin\rho$$

$$\hat{\omega}_{ds}(k+1|k) = \hat{\omega}_e(k+1|k)\sin\rho + \hat{\omega}_d(k+1|k)\cos\rho$$

$$\hat{\sigma}(k+1|k) = \varepsilon_s$$

$$\hat{\eta}_s(k+1|k) = \eta_s$$

$$\hat{V}_r(k+1|k) = V_a$$

$$\hat{V}_{wx}(k+1|k) = 0.$$

$$\hat{\gamma}_r(k+1|k) = \theta - \alpha\cos\phi$$

$$\hat{\varepsilon}(k+1|k) = \varepsilon_m$$

Initial Predicted Measurements (not already initialized as states)

$$\hat{\sigma}_m(k+1|k) = \varepsilon_s$$

$$\hat{V}_a(k+1|k) = V_a$$

68

$$\hat{\gamma}_a(k+1|k) = \hat{\gamma}_r(k+1|k)$$

Initialize ϕ – State Transition Matrix

$$\phi_{21} = \phi_{61} = T$$

$$\phi_{22} = \phi_{33} = \phi_{44} = \phi_{55} = \phi_{66} = 1$$

Initialize H – Measurement Matrix

$$H_{12} = 1$$

$$H_{16} = -1$$

Initialize Q – Disturbance Covariance Matrix

$$QMAT = 0.25 \times 10^{-6}$$

Initialize P(k|k) – State Covariance Matrix

$$P_{11}(0|0) = 5 \times 10^{-6}$$

$$P_{22}(0|0) = 0.72 \times 10^{-6}$$

$$P_{33}(0|0) = 401$$

$$P_{44}(0|0) = 400$$

69

$$P_{55}(0|0) = 1 \times 10^{-6}$$

$$P_{66}(0|0) = 0.09 \times 10^{-6}$$

Initialize R – Measurement Covariance Matrix

$$R_{11} = 0.72 \times 10^{-6}$$

$$R_{22} = 1$$

$$R_{33} = 1 \times 10^{-6}$$

$$R_{44} = 0.09 \times 10^{-6}$$

Initialize Azimuth Filter

$$PA_{11}(0|0) = 0.22 \times 10^{-6}$$

$$PA_{22}(0|0) = 25 \times 10^{-6}$$

$$RA_{11} = 0.22 \times 10^{-6}$$

$$RA_{22} = 2.25 \times 10^{-6}$$

BLOCK 7L

Carries out the elevation and azimuth Kalman filter computations.

Measurements Formed From Inputs

$$\sigma_m = \epsilon_s$$

$$\sin \gamma_{am} = \sin \theta - \alpha_m \cos \theta \cos \phi$$

$$\cos \gamma_{am} = \cos \theta - \alpha_m \sin \theta \cos \phi$$

$$\gamma_{am} = \tan^{-1}[\frac{\sin \gamma_{am}}{\cos \gamma_{am}}]$$

Process New Gyro Measurements

$$\dot{\hat{\epsilon}} = \frac{[\hat{\omega}_e(k+1|k) + \hat{\omega}_e(k|k)]}{2} - \omega_{em}$$

$$\hat{\epsilon}(k+1|k) = \hat{\epsilon}(k|k) + T \dot{\hat{\epsilon}}$$

$$\hat{\sigma}_m(k+1|k) = \hat{\sigma}(k+1|k) - \hat{\epsilon}(k+1|k) \cos \rho$$

Estimated Values of States at Start of Cycle

$$\Delta_1 = \sigma_m - \hat{\sigma}_m(k|k-1)$$

$$\Delta_2 = V_a - \hat{V}_a(k|k-1)$$

$$\Delta_3 = \gamma_{am} - \hat{\gamma}_a(k|k-1)$$

$$\Delta_4 = \epsilon_m - \hat{\epsilon}(k|k-1)$$

$$\overline{RESID} = \overline{K} \cdot \overline{\Delta}$$

71

$$\hat{\omega}_{es}(k|k) = \hat{\omega}_{es}(k|k-1) + \text{RESID}_1$$

$$\hat{\sigma}(k|k) = \hat{\sigma}(k|k-1) + \text{RESID}_2$$

$$\hat{V}_r(k|k) = \hat{V}_r(k|k-1) + \text{RESID}_3$$

$$\hat{V}_{wx}(k|k) = \hat{V}_{wx}(k|k-1) + \text{RESID}_4$$

$$\hat{\gamma}_r(k|k) = \hat{\gamma}_r(k|k-1) + \text{RESID}_5$$

$$\hat{\varepsilon}(k|k) = \varepsilon(k|k-1) + \text{RESID}_6$$

$$\Delta\eta = \eta_s - \hat{\eta}_s(k|k-1)$$

$$\Delta\omega = \omega_{dm} - \hat{\omega}_{ds}(k|k-1)$$

$$\hat{\eta}_s(k|k) = \hat{\eta}_s(k|k-1) + V_{11}\,\Delta\eta + V_{12}\,\Delta\omega$$

$$\hat{\omega}_{ds}(k|k) = \hat{\omega}_{ds}(k|k-1) + V_{21}\,\Delta\eta + V_{22}\,\Delta\omega$$
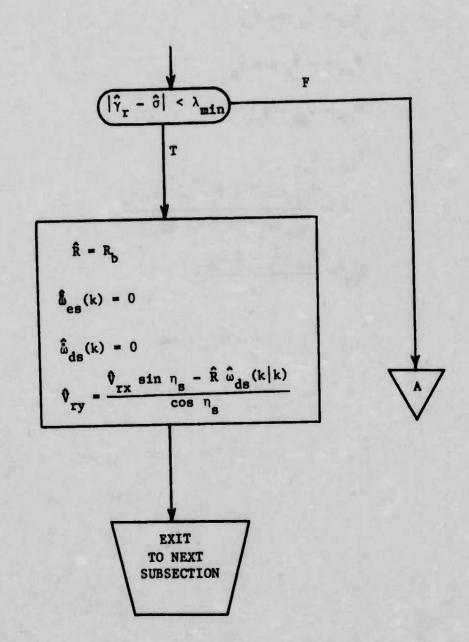
Estimated Values of Calculated Variables

$$\dot{\hat{\theta}} = \frac{(a_n\,\cos\phi - g\,\cos\theta)}{\hat{V}_a(k|k-1)}$$

a_n = normal accelerometer measurement

72

$$\dot{\psi} = \frac{a_n \sin \phi}{\hat{V}_a(k|k-1) \cos [\gamma_a(k|k-1)]}$$

$$\dot{\gamma}_r = \frac{(a_n \cos \phi - g \cos \theta)}{\hat{V}_r(k\ k)}$$

```
                    │
                    ▼
        ╭───────────────────────╮           F
        │ |\hat{\dot{\gamma}}_r - \hat{\sigma}| < \lambda_{min} │──────────────┐
        ╰───────────────────────╯                             │
                    │ T                                        │
                    ▼                                          │
        ┌───────────────────────────────┐                     │
        │                               │                     │
        │   \hat{R} = R_b               │                     │
        │                               │                     │
        │   \hat{\dot{\omega}}_{es}(k) = 0              │                     │
        │                               │                     ▼
        │   \hat{\dot{\omega}}_{ds}(k) = 0              │                  ╲   A   ╱
        │                               │                   ╲     ╱
        │   \hat{V}_{ry} = \frac{\hat{V}_{rx} \sin \eta_s - \hat{R} \hat{\omega}_{ds}(k|k)}{\cos \eta_s} │       ╲ ╱
        │                               │
        └───────────────────────────────┘
                    │
                    ▼
            ╱─────────────────╲
           │      EXIT         │
           │    TO NEXT        │
           │   SUBSECTION      │
            ╲─────────────────╱
```

$$\hat{\gamma}_a = \hat{\gamma}(k|k) + \tan^{-1} \left[\frac{\hat{V}_{wx}(k|k) \sin \hat{\gamma}_r(k|k)}{\hat{V}_r(k|k) - \hat{V}_{wx}(k|k) \cos \hat{\gamma}_r(k|k)} \right]$$

$$\hat{V}_a = (\hat{V}_{wx}^2(k|k) + \hat{V}_r^2(k|k) - 2\hat{V}_{wx}(k|k) \, \hat{V}_r(k|k) \, c\hat{\gamma}_r(k|k))^{1/2}$$

$$\hat{V}_{ax} = \hat{V}_a \cos \hat{\gamma}_a$$

$$\hat{V}_{az} = - \hat{V}_a \sin \hat{\gamma}_a$$

$$\hat{V}_{rx} = \hat{V}_{ax} + \hat{V}_{wx}$$

$$\hat{V}_{rz} = \hat{V}_{az}$$

$$\hat{R} = \frac{\hat{V}_{rx} \sin \hat{\sigma} + \hat{V}_{rz} \cos \hat{\sigma} \, c\eta_s}{\hat{\omega}_{es} \, c\eta_s + \hat{\omega}_{ds} \, s\hat{\sigma} \, s\eta_s}$$
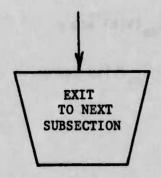
$$\hat{V}_{ry} = \frac{\hat{V}_{rx} \, s\hat{\eta}_s - \hat{R} \, \hat{\omega}_{ds}}{c\eta_s}$$

$$\hat{V}_{rN} = \hat{V}_{rx} \cos \psi - \hat{V}_{ry} \sin \psi$$

$$\hat{V}_{rE} = \hat{V}_{rx} \sin \psi + \hat{V}_{ry} \cos \psi$$

$$\hat{V}_{rR} = (\hat{V} \quad c\eta_s + \hat{V} \, s\eta_s \,) \, c\sigma - V_{rz} \, s\sigma$$

74

$$\dot{V}_{rN} = \hat{\dot{V}}_a(-\sin\theta\,\cos\psi + \alpha_p\,\cos\phi\,\cos\epsilon\,\cos\psi)\,\dot{\theta}$$

$$+ \hat{\dot{V}}_a\left[-\cos\theta\,\sin\psi + \alpha_p(-\cos\phi\,\sin\theta\,\sin\psi + \sin\phi\,\cos\psi)\right]\psi'$$

$$+ \hat{\dot{V}}_a(-\alpha_p\,\sin\phi\,\sin\theta\,\cos\psi + \cos\phi\,\sin\psi)\,\phi'$$

$$\dot{V}_{rE} = \hat{\dot{V}}_a(-\sin\theta\,\sin\psi + \alpha_p\,\cos\phi\,\cos\theta\,\sin\psi)\,\dot{\theta}$$

$$+ \hat{\dot{V}}_a\,\cos\theta\,\cos\psi + \alpha_p(\cos\phi\,\sin\theta\,\cos\psi + \sin\phi\,\sin\psi)\ \psi'$$

$$+ \hat{\dot{V}}_a(-\alpha_p\,\sin\phi\,\sin\theta\,\sin\psi - \cos\phi\,\cos\psi)\,\phi'$$

$$\dot{V}_{rz} = \hat{\dot{V}}_a(-\cos\theta - \alpha_p\,\cos\phi\,\sin\theta)\,\theta + \hat{\dot{V}}_a(-\alpha_p\,\sin\phi\,\cos\theta)\,\phi'$$

$$\hat{\dot{\omega}}_{es} = \frac{\left[(\dot{V}_{rN}\cos(\psi+\eta_s) + \dot{V}_{rE}\sin(\psi+\eta_s))\sin\hat{\sigma} + \dot{V}_{rz}\cos\hat{\sigma} + 2\hat{\dot{V}}_{rR}\hat{\omega}_{es}\right]}{\hat{R}} - \hat{\omega}_{ds}^2\,\tan\hat{\sigma}$$

$$\hat{\dot{\omega}}_{ds} = \frac{\dot{V}_{rN}\sin(\psi+\eta_s) - \dot{V}_{rE}\cos(\psi+\eta_s) + \left[\dot{V}_{rN}\cos(\psi+\eta_s) + \dot{V}_{rE}\sin(\psi+\eta_s)\right]\dfrac{\hat{\omega}_{ds}}{\cos\hat{\sigma}}}{\hat{R}}$$

```
 EXIT
TO NEXT
SUBSECTION
```

75

Predicted Values of States at Start of Next Cycle

$$\hat{\omega}_{es}(k+1|k) = \hat{\omega}_{es}(k|k) + \hat{\dot{\omega}}_{es} \, T$$

(Limit $\hat{\omega}_{es}(k+1|k)$ to be ≤ 0)

$$\hat{\omega}_{ds}(k+1|k) = \hat{\omega}_{ds}(k|k) + \hat{\dot{\omega}}_{ds} \, T$$

$$\hat{\dot{\eta}}_s = \frac{\hat{\omega}_{ds}}{\cos \hat{\sigma}} - \dot{\psi}$$

$$\hat{\eta}_s(k+1|k) = \hat{\eta}_s(k|k) + \dot{\eta}_s(k|k) \, T$$

$$\hat{\sigma}(k+1|k) = \hat{\sigma}(k|k) + \hat{\omega}_{es}(k|k) \, T$$

$$\hat{V}_r(k+1|k) = \hat{V}_r(k|k)$$

$$\hat{V}_{wx}(k+1|k) = \hat{V}_{wx}(k|k)$$

$$\hat{\gamma}_r(k+1|k) = \hat{\gamma}_r(k|k) + \dot{\gamma}_r \, T$$

$$\hat{\omega}_e(k+1|k) = \hat{\omega}_{es}(k+1|k) \cos \rho + \hat{\omega}_{ds}(k+1|k) \sin \rho$$

$$\hat{\omega}_d(k+1|k) = - \hat{\omega}_{es}(k+1|k) \sin \rho + \hat{\omega}_{ds}(k+1|k) \cos \rho$$

$$\hat{\omega}_e(k|k) = \hat{\omega}_{es}(k|k) \cos \rho + \hat{\omega}_{ds}(k|k) \sin \rho$$

$$\hat{\omega}_d(k|k) = - \hat{\omega}_{es}(k|k) \sin \rho + \hat{\omega}_{ds}(k|k) \cos \rho$$

Predicted Values of Measurements

$$\hat{V}_a(k+1|k) = [\hat{V}_{wx}^2(k+1|k) + \hat{V}_r^{\,2}(k+1|k)$$

$$- 2\hat{V}_{wx}(k+1|k) \, \hat{V}_r(k+1|k) \cos \hat{\gamma}_r(k+1|k)]^{1/2}$$

76

$$\hat{\gamma}_a(k+1|k) = \hat{\gamma}_r(k+1|k) + \tan^{-1}\left[\frac{\hat{V}_{wx}(k+1|k)\ \sin\gamma_r(k+1|k)}{\hat{V}_r(k+1|k) - \hat{V}_{wx}(k+1|k)\ \cos\gamma_r(k+1|k)}\right]$$

BLOCK 7K

Computes the Kalman Filter Gain Matrix for both azimuth and elevation channels.

Compute ϕ Matrix – Elevation Channel

$$\phi_{11} = 1 + T\ \frac{\psi\ \hat{\omega}_{es}(k+1|k) - \hat{\dot{\theta}}}{\tan\ [\hat{\sigma}(k|k) - \hat{\gamma}_r(k|k)]}$$

$$\phi_{12} = \frac{-T\ \hat{\omega}_{es}(k|k)\ [2\hat{\omega}_{es}(k|k) - \hat{\dot{\theta}}]}{\sin^2\ [\hat{\sigma}(k|k) - \hat{\gamma}_r(k|k)]}$$

$$\phi_{13} = \frac{T\ \hat{\omega}_{es}(k|k)\ \hat{\dot{\theta}}}{\hat{V}_r(k|k)\ \tan\ [\hat{\sigma}(k|k) - \hat{\gamma}_r(k|k)]}$$

$$\left\{\begin{array}{l} \text{If}\quad |\hat{\sigma}(k|k) - \hat{\gamma}_r(k|k)|\quad \text{is near zero, then} \\[2ex] \text{Set}\qquad \phi_{11} = 1 \qquad\text{and}\qquad \phi_{12} = \phi_{13} = 0 \end{array}\right\}$$

$$\phi_{14} = -\ \phi_{12}$$

$$\phi_{53} = -\ \frac{T\ \hat{\dot{\theta}}}{\hat{V}_r(k|k)}$$

Compute H Matrix - Elevation Channel

$$V_{an\ell} = [\hat{V}_r^{\;2}(k+1|k) + \hat{V}_{wx}^2(k+1|k)$$

$$- 2\hat{V}_r(k+1|k) \; \hat{V}_{wx}(k+1|k) \; \cos \hat{\gamma}_r(k+1|k)]^{1/2}$$

$$H_{23} = \frac{\hat{V}_r(k+1|k) - \hat{V}_{wx}(k+1|k) \; \cos \hat{\gamma}_r(k+1|k)}{V_{an\ell}}$$

$$H_{24} = \frac{\hat{V}_{wx}(k+1|k) - \hat{V}_r(k+1|k) \; \cos \hat{\gamma}_r(k+1|k)}{V_{an\ell}}$$

$$H_{25} = \frac{\hat{V}_r(k+1|k) \; \hat{V}_{wx}(k+1|k) \; \sin \hat{\gamma}_r(k+1|k)}{V_{an\ell}}$$

$$H_{33} = \frac{-\hat{V}_{wx}(k+1|k) \; \sin \hat{\gamma}_r(k+1|k)}{V_{an\ell}^2}$$

$$H_{34} = \frac{\hat{V}_r(k+1|k) \; \sin \hat{\gamma}_r(k+1|k)}{V_{an\ell}^2}$$

$$H_{35} = 1 + \frac{\hat{V}_r(k+1|k) \; \hat{V}_{wx}(k+1|k) \; \cos \hat{\gamma}_r(k+1|k) - V_{wx}^2(k+1|k)}{V_{an\ell}^2}$$

78

Compute Kalman Gain Matrix - Elevation Channel

$$P(k+1|k) = \phi \; P(k|k) \; \phi^T + \Gamma Q \Gamma^T$$

$$K(k+1) = P(k+1|k) \; H^T \; [H \; P(k+1|k) \; H^T + R]^{-1}$$

$$P(k+1|k+1) = [I - K(k+1) \; H] \; P(k+1|k)$$

If $\hat{\gamma}_r(k+1|k) < 15°$ then zero out horizontal wind channel gains.

Azimuth Filter Gains

(Same form as above)

BOMB

Computes true inputs required for computation of bomb's horizontal range at release, and also for other WD computations when the filter is by-passed.

$$\sin \gamma_{ap} = \sin \theta - \alpha_m \cos \theta \cos \phi$$

$$\cos \gamma_{ap} = \cos \theta - \alpha_m \sin \theta \cos \phi$$

$$\gamma_{ap} = \tan^{-1} \left[\frac{\sin \gamma_{ap}}{\cos \gamma_{ap}} \right]$$

$$V_r = [V_{am}^2 + V_{wx}^2 + 2V_{am} \; V_{wx} \cos \gamma_{ap}]^{1/2}$$

$$\Delta\gamma = \cos^{-1} \left[\frac{V_r^2 + V_{am}^2 - V_{wx}^2}{2 \; V_{am} \; V_r} \right]$$

If V_{wx} is close to zero, set $\Delta\gamma = 0$ otherwise,

79

$$\Delta \gamma = \tan^{-1} \Delta \gamma \frac{V_{xw}}{|V_{xw}|}$$

$$\hat{\gamma}_r(k+1|k) = \gamma_{ap} + \Delta \gamma$$

$$\hat{\sigma}(k+1|k) = \epsilon_s + \Delta \gamma$$

$$\eta = \eta_g + \eta_m$$

$$\eta_s(k+1|k) = \eta_s$$

$$\epsilon = \epsilon_g + \epsilon_m + \Delta \gamma$$

$$\hat{V}_a(k+1|k) = V_{am}$$

$$\hat{V}_{wx}(k+1|k) = V_{xw}$$

$$R_{TGT} = \frac{H_p - H_T}{M3(1,3)}$$

$$\hat{\omega}_e(k+1|k) = \frac{V_r[\cos \eta \sin \epsilon + \alpha \cos \epsilon]}{R_b}$$

$$\hat{\omega}_d(k+1|k) = \frac{V_r \sin \eta}{R_b}$$

$$\dot{\omega}_{es}(k+1|k) = \hat{\omega}_e(k+1|k) \cos \rho - \hat{\omega}_d(k+1|k) \sin \rho$$

$$\hat{\omega}_{ds}(k+1|k) = \hat{\omega}_e(k+1|k) \sin \rho + \hat{\omega}_d(k+1|k) \cos \rho$$

BLOCK 8

Computes velocities and flight path angle relative to air speed vector.

$$\gamma_a = \gamma_a(k+1|k)$$

$$\alpha_p = \frac{\sin \theta - \sin \gamma_a}{\cos \phi \cos \theta}$$

$$V_A = \hat{V}_a(k+1|k)$$

$$V_{AX} = V_A \cos \gamma_a$$

$$V_{AY} = - V_A \alpha_p \sin \phi$$

$$V_X = V_{AX} + \hat{V}_{wx}(k+1|k)$$

$$V_Z = - V_A \sin \gamma_a$$

BLOCK 10

Computes range and altitude from angle rates.

$$R = \frac{V_x \sin \hat{\sigma}(k+1|k) + V_Z \cos \hat{\sigma}(k+1|k) \cos \hat{\eta}_s(k+1|k)}{\hat{\omega}_{es}(k+1|k) \cos \hat{\eta}_s(k+1|k) + \hat{\omega}_{ds}(k+1|k) \sin \hat{\sigma}(k+1|k) \sin \eta_s(k+1|k)}$$

Denominator of R is checked against zero. If so, R is set to R_b before the division is made.

$$R_x = R \cos \hat{\sigma}(k+1|k) \cos \hat{\eta}_s(k+1|k)$$

$$H = - R \sin \hat{\sigma}(k+1|k)$$

$$V_Y = \frac{V_X \sin \hat{\eta}_s(k+1|k) - R \hat{\omega}_{ds}(k+1|k)}{\cos \hat{\eta}_s(k+1|k)}$$

$$V_{WY} = V_Y - V_{AY}$$

BLOCK 11

A pullup warning is issued (JPULLUP = 1) if the aircraft is in danger of either hitting the ground or getting caught in the bomb blast. A 4-g pullup capability is assumed for the aircraft and the M117 low drag bomb is assumed for the blast clearance.

$$H_{WG} = GW_1 + GW_2(1 - \cos \gamma_a) V_a^2/96.6 + GW_3 V_Z$$

$$H_{WB} = BW_1 - BW_2 \sin \gamma_a + BW_3 V_Z$$

$$H_W = \max (H_{WG}, H_{WB})$$

If $H_p \leq H_W$ then set JPULLUP = 1.

BLOCK 14

Computes stabilized aircraft referenced initial bomb velocities including ejection velocities for use in ballistic equations

$$V_{XB} = V_{AX} + V_{EJ} \cdot M1(3,1)$$

$$V_{YB} = V_{AY} + V_{EJ} \cdot M1(3,2)$$

$$V_{ZB} = V_{AZ} + V_{EJ} \cdot M1(3,3)$$

$$H_{BB} = H$$

BLOCK 15

Computes bomb's time of fall and horizontal range assuming a low drag bomb

$$g_1 = K_g g$$

$$t_o = \frac{(V_{ZB}^2 + 2g_1 H_{BB})^{1/2} - V_{ZB}}{g_1}$$

$$X_{Bo} = V_{XB} t_o$$

$$t_f = K_T t_o$$

$$X_B = X_{Bo} + \hat{V}_{wx}(k+1|k) \cdot t_f$$

$$L = V_{XB} t_f - X_{Bo}$$

$$Y_B = V_{YB} \cdot t_o + V_{WY} \cdot t_f$$

BLOCK 17

Computes time to go and number of iterations to go until release.

$$t_{go} = \frac{R_x - X_B}{V_X}$$

$$i_{t_{go}} = 20 \cdot t_{go}$$

83

BLOCK 16

Computes CCIP mode steering reticle in stabilized aircraft coordinate system.

$$P_X = X_B/R_B$$

$$P_Y = Y_B/R_B$$

$$P_Z = (H_B + V_Z T)/R_B$$

BLOCK 20B

Computes CAL mode steering reticle pointing vector in stabilized aircraft coordinate system.

$$\omega_{DSC} = \frac{L \cdot V_X \cdot \sin \hat{n}_s(k+1|k)}{R(R_X + L)}$$

$$P_X = M3(1,1) = \bar{I}_R \cdot \bar{X}$$

$$P_Y = M3(1,2) + t_f[\omega_{DSC} - \hat{\omega}_{ds}(k+1|k)] \cdot K_{steer}$$

$$\text{where } M3(1,2) = \bar{I}_R \cdot \bar{Y}$$

$$P_Z = M3(1,3) = \bar{I}_R \cdot \bar{Z}$$

84

BLOCK 20D

Computes aircraft body referenced steering reticle pointing vector.

$$P_I = P_X \cos \theta - P_Z \sin \theta$$

$$P_J = P_X \sin \theta \sin \phi + P_Y \cos \theta + P_Z \cos \theta \sin \phi$$

$$P_K = P_X \sin \theta \cos \phi - P_Y \sin \phi + P_Z \cos \theta \cos \phi$$

$$\eta_R = \tan^{-1} (P_J/P_I)$$

$$\epsilon_R = \tan^{-1} (P_K/P_I)$$

BLOCK 20F

Computes CCIP mode predicted impact line.

$$V_{PI} = V_X \cos \theta - V_Z \sin \theta$$

$$V_{PJ} = V_X \sin \theta \sin \phi + V_{YB} \cos \theta + V_Z \cos \theta \sin \phi$$

$$V_{PK} = V_X \sin \theta \cos \phi - V_{YB} \sin \phi + V_Z \cos \theta \cos \phi$$

$$\tau_{BETA} = [-\frac{1 + \epsilon_R^2}{1 + \eta_R^2}] \; [\frac{P_I V_{PJ} - P_J V_{PI}}{P_K V_{PI} - P_I V_{PK}}]$$

BLOCK 21

Computes the pointing vector for the tracking reticle.

$$T_i = \bar{I}_R \cdot \bar{i} = M2(1,1)$$

$$T_j = \bar{I}_R \cdot \bar{j} = M2(1,2)$$

$$T_k = \bar{I}_R \cdot k = M2(1,3)$$
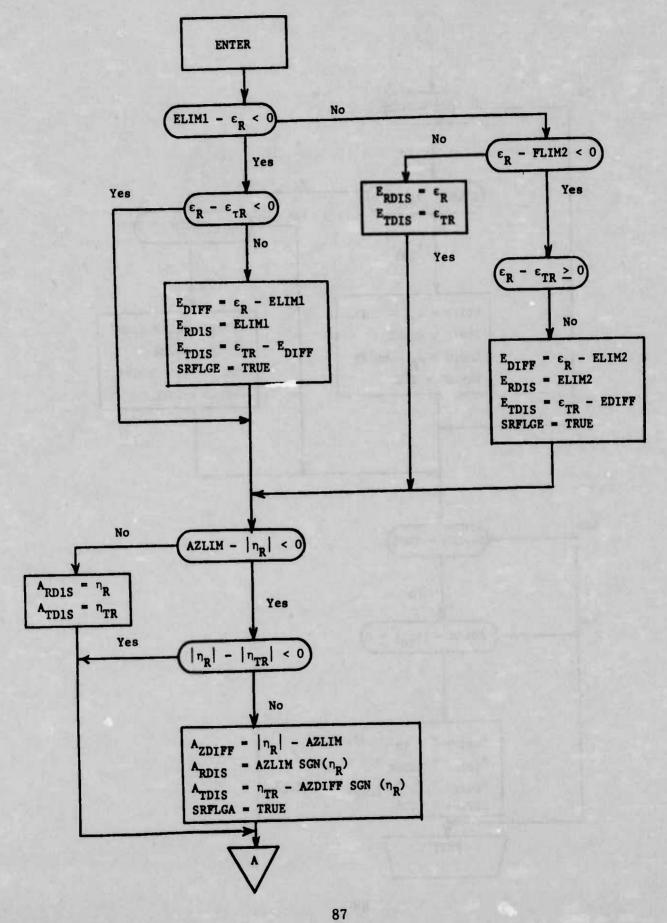
$$n_{TR} = \tan^{-1}(T_j/T_i)$$
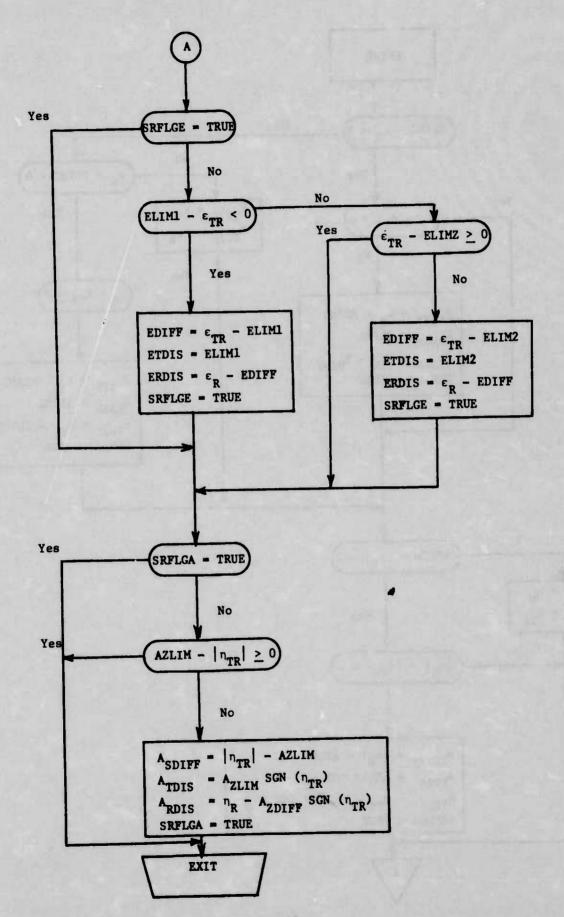
$$\varepsilon_{TR} = -\tan^{-1}(T_k/T_i)$$

LOCK

When locked onto a target, senses if either reticle goes off the HUD and keeps it on the HUD.

ENTER

ELIM1 − ϵ_R < 0 —— No

Yes

$\epsilon_R - \epsilon_{\tau R}$ < 0

Yes

No

$E_{DIFF} = \epsilon_R - ELIM1$
$E_{RD1S} = ELIM1$
$E_{TDIS} = \epsilon_{TR} - E_{DIFF}$
SRFLGE = TRUE

$E_{RDIS} = \epsilon_R$
$E_{TDIS} = \epsilon_{TR}$

No

$\epsilon_R - FLIM2$ < 0

Yes

Yes

$\epsilon_R - \epsilon_{TR} \geq 0$

No

$E_{DIFF} = \epsilon_R - ELIM2$
$E_{RDIS} = ELIM2$
$E_{TDIS} = \epsilon_{TR} - EDIFF$
SRFLGE = TRUE

No

AZLIM − $|n_R|$ < 0

$A_{RD1S} = n_R$
$A_{TD1S} = n_{TR}$

Yes

Yes

$|n_R| - |n_{TR}|$ < 0

No

$A_{ZDIFF} = |n_R| - AZLIM$
$A_{RDIS} = AZLIM\ SGN(n_R)$
$A_{TDIS} = n_{TR} - AZDIFF\ SGN\ (n_R)$
SRFLGA = TRUE

A

87

A

SRFLGE = TRUE

Yes

No

$ELIM1 - \epsilon_{TR} < 0$

No

Yes

$\dot{\epsilon}_{TR} - ELIMZ \geq 0$

Yes

No

$EDIFF = \epsilon_{TR} - ELIM1$
$ETDIS = ELIM1$
$ERDIS = \epsilon_R - EDIFF$
$SRFLGE = TRUE$

$EDIFF = \epsilon_{TR} - ELIM2$
$ETDIS = ELIM2$
$ERDIS = \epsilon_R - EDIFF$
$SRFLGE = TRUE$

SRFLGA = TRUE

Yes

No

Yes

$AZLIM - |n_{TR}| \geq 0$

No

$A_{SDIFF} = |n_{TR}| - AZLIM$
$A_{TDIS} = A_{ZLIM} \, SGN \, (n_{TR})$
$A_{RDIS} = n_R - A_{ZDIFF} \, SGN \, (n_{TR})$
$SRFLGA = TRUE$

EXIT

88

NOLOCK

If not locked on to target, senses when either reticle goes off the HUD and keeps it on the HUD.

```
                              ┌─────────────┐
                              │    ENTER    │
                              └─────────────┘
                                     │
        Yes    ╭──────────────────────────────────╮
        ┌──────│       ELIM1 - εR < 0             │
        │      ╰──────────────────────────────────╯
        │                    │ No
        │                    ▼                              Yes
        │      ╭──────────────────────────────────╮────────────┐
        │      │       εR - ELIM2 ≥ 0             │            │
        │      ╰──────────────────────────────────╯            │
        │                    │ No                              │
        │                    ▼                                 │
        │            ┌──────────────────┐                      │
        └───────────▶│ SRFLGM = .TRUE.  │                      │
                     └──────────────────┘                      │
                              │◀──────────────────────────────┘
                              ▼
        No     ╭──────────────────────────────────╮
        ┌──────│      AZLIM - |ηR| < 0           │
        │      ╰──────────────────────────────────╯
        │                    │ Yes
        │                    ▼
        │            ┌──────────────────┐
        │            │ SRFLGM = .TRUE.  │
        │            └──────────────────┘
        │                    │
        │                    ▼
        Yes    ╭──────────────────────────────────╮
        ┌──────│      ELIM1 - εTR < 0            │
        │      ╰──────────────────────────────────╯
        │                    │ No
        │                    ▼                              Yes
        │      ╭──────────────────────────────────╮────────────┐
        │      │      εTR - ELIM2 ≥ 0           │            │
        │      ╰──────────────────────────────────╯            │
        │                    │ No                              │
        │                    ▼                                 │
        │            ┌──────────────────┐                      │
        └───────────▶│ TRFLGM = .TRUE.  │                      │
                     └──────────────────┘                      │
                              │◀──────────────────────────────┘
                              ▼
        No     ╭──────────────────────────────────╮
        ┌──────│     AZLIM - |ηTR| < 0          │
        │      ╰──────────────────────────────────╯
        │                    │ Yes
        │                    ▼
        │            ┌──────────────────┐
        │            │ TRFLGM = .TRUE.  │
        │            └──────────────────┘
        │                    │
        └────────────────────▼
                     ╱──────────────╲
                    │      EXIT      │
                     ╲──────────────╱
```
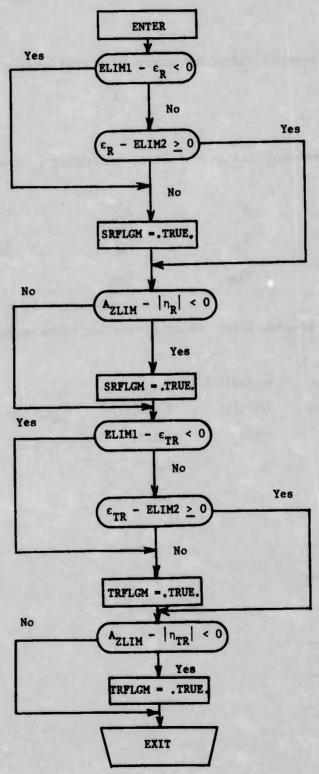
Decision and process blocks (top to bottom):

- $\text{ELIM1} - \epsilon_R < 0$ — Yes branch bypasses; No continues
- $\epsilon_R - \text{ELIM2} \geq 0$ — Yes branch bypasses; No continues
- SRFLGM = .TRUE.
- $A_{ZLIM} - |\eta_R| < 0$ — No branch bypasses; Yes continues
- SRFLGM = .TRUE.
- $\text{ELIM1} - \epsilon_{TR} < 0$ — Yes branch bypasses; No continues
- $\epsilon_{TR} - \text{ELIM2} \geq 0$ — Yes branch bypasses; No continues
- TRFLGM = .TRUE.
- $A_{ZLIM} - |\eta_{TR}| < 0$ — No branch bypasses; Yes continues
- TRFLGM = .TRUE.
- EXIT

89

<u>OUT</u>

Prints out several variables every 20 iterations. The counter is IC.

<u>DUMP</u>

Prints out several filter variables according to the following format:

θ	ϕ	η_g	ϵ_g	H_p
H_T	V_a	α_m	η_m	ϵ_m
a_k	ω_{EM}	ω_{DM}		

(repeat above quantities with noise added if IDROP $\neq$ 5)

$\hat{\eta}_s(k+1\vert k)$	$\hat{\omega}_{ds}(k+1\vert k)$	V_{11}	V_{12}	V_{21}	V_{22}
$\hat{\omega}_{es}(k+1\vert k)$	$\hat{\sigma}(k+1\vert k)$	$\hat{V}_r(k+1\vert k)$	$\hat{V}_{wx}(k+1\vert k)$	$\hat{\gamma}_r(k+1\vert k)$	$\hat{\epsilon}(k+1\vert k)$
$RESID_1$	$RESID_2$	$RESID_3$	$RESID_4$	$RESID_5$	$RESID_6$
Δ_1	Δ_2	Δ_3	Δ_4		

$$\dot{\hat{\omega}}_{es} = \text{---}$$
$$\hat{\dot{\omega}}_{ds} = \text{---}$$
$$t_f = \text{---}$$
$$X_B = \text{---}$$
$$R_X = \text{---}$$
$$t_{go} = \text{---}$$

90

MATDMP

Prints out Kalman gain matrix as computed in BLOCK 7K.

$$
\begin{matrix}
K_{11} & K_{12} & K_{13} & K_{14} \\
K_{21} & K_{22} & K_{23} & K_{24} \\
K_{31} & K_{32} & K_{33} & K_{34} \\
K_{41} & K_{42} & K_{43} & K_{44} \\
K_{51} & K_{52} & K_{53} & K_{54} \\
K_{61} & K_{62} & K_{63} & K_{64}
\end{matrix}
$$

DEVELOPMENT OF AUTOPILOT CONTROL LAW

1. Definition of Aerodynamic Differential Equations

The aircraft coordinate system must be defined first. The unit vectors are as follows: $\vec{1}_x = \vec{i}$ is along the fuselage reference line, $\vec{1}_y = \vec{j}$ is along the right wing, and $\vec{1}_z = \vec{k} = \vec{i} \times \vec{j}$ is down. Coordinate systems are discussed in depth in References 1 and 9.

Complete aerodynamic differential equations are developed in Reference 3. By linearizing the equations and making reasonable assumptions, the equations may be simplified and written in uncoupled form. The <u>longitudinal equations of motion</u> are the following:

$$\dot{u} = X_u u + X_w w \tag{12}$$

$$\dot{w} = Z_u u + Z_w w + U_o q + Z_{\delta_e} \delta_e \tag{13}$$

$$\dot{q} = M_u u + M_w w + M_q q + M_{\delta_e} \delta_e \tag{14}$$

where

    u = component of velocity perturbation along the $\vec{1}_x$ axis

    U_o = trim (horizontal) air speed

    w = component of velocity perturbation along the $\vec{1}_z$ axis

    q = angular rate about the $\vec{1}_y$ axis

    δ_e = elevator deflection angle

and the dimensional stability derivatives X_u, X_w, Z_u, Z_w, Z_{δ_e}, M_u, M_w, M_q, and M_{δ_e} are given in Appendix I as functions of atmospheric density, wing characteristics, etc.

The <u>lateral equations of motion</u> are the following:

$$\dot{\beta} = Y_v \beta - r + Y_{\delta_a} \delta_a + Y_{\delta_r} \delta_r \tag{15}$$

$$\dot{p} = L_\beta \beta + L_p p + L_r r + L_{\delta_a} \delta_a + L_{\delta_r} \delta_r \tag{16}$$

$$\dot{r} = N_\beta \beta + N_p p + N_r r + N_{\delta_a} \delta_a + N_{\delta_r} \delta_r \tag{17}$$

where

$$\beta = \frac{v}{U_o}$$

v = component of velocity perturbation along the $\vec{1}_y$ axis

p = angular rate about the $\vec{1}_x$ axis

r = angular rate about the $\vec{1}_z$ axis

δ_a = aileron deflection angle

δ_r = rudder deflection angle

and the dimensional stability derivatives Y_v, Y_{δ_a}, Y_{δ_r}, L_β, L_p, L_r, L_{δ_a}, L_{δ_r}, N_β, N_p, N_r, N_{δ_a}, and N_{δ_r} are given in Appendix I. It is also implicitly assumed that

$$p = \dot{\phi} - \dot{\psi} \sin \theta \approx \dot{\phi} \tag{18}$$

$$q = \dot{\theta} \cos \phi + \dot{\psi} \cos \theta \sin \phi \approx \dot{\theta} \tag{19}$$

$$r = -\dot{\theta} \sin \phi + \dot{\psi} \cos \theta \cos \phi \approx \dot{\psi} \tag{20}$$

Equations (12)-(17) can be combined in matrix, or state, notation in the following manner:

94

$$
\begin{bmatrix} \dot{u} \\ \dot{w} \\ \dot{q} \\ \dot{\beta} \\ \dot{p} \\ \dot{r} \end{bmatrix}
=
\begin{bmatrix}
X_u & X_w & 0 & 0 & 0 & 0 \\
Z_u & Z_w & U_o & 0 & 0 & 0 \\
M_u & M_w & M_q & 0 & 0 & 0 \\
0 & 0 & 0 & Y_v & 0 & -1 \\
0 & 0 & 0 & L_\beta & L_p & L_r \\
0 & 0 & 0 & N_\beta & N_p & N_r
\end{bmatrix}
\begin{bmatrix} u \\ w \\ q \\ \beta \\ p \\ r \end{bmatrix}
$$

$$
+
\begin{bmatrix}
0 & 0 & 0 \\
Z_{\delta_e} & 0 & 0 \\
M_{\delta_e} & 0 & 0 \\
0 & Y_{\delta_a} & Y_{\delta_r} \\
0 & L_{\delta_a} & L_{\delta_r} \\
0 & N_{\delta_a} & N_{\delta_r}
\end{bmatrix}
\begin{bmatrix} \delta_e \\ \delta_a \\ \delta_r \end{bmatrix}
\tag{21}
$$

The vector of deflection angles represents the system input vector.

2. Definition of Inner Loop Control Laws and States

The three deflection angles δ_e, δ_a, and δ_r are themselves functions of the aerodynamic quantities of equations (12)-(17). These relationships are referred to as inner loop control laws.

Figure 21 shows the pitch, or elevator, control law assumed. The block diagram can be reduced to the form shown in Figure 22, wherein the states x_1 and x_2 are defined. From Figure 22, an expression for δ_e in terms of the states x_1 and x_2 can be written:
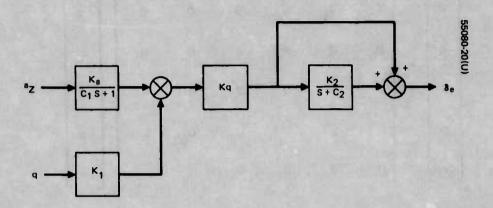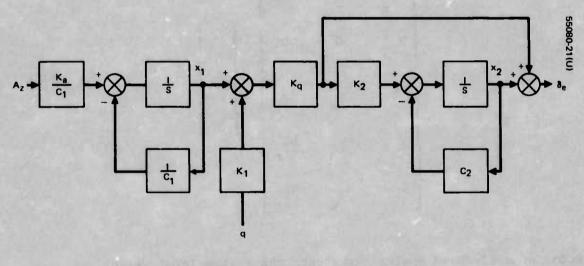
Figure 21. Block Diagram of Pitch Control Law (Inner Loop)

a_z	=	NORMAL ACCELERATION
K_1	=	460
K_2	=	3
C_1	=	0.55
C_2	=	0.3
K_a	=	2
K_q	=	5.4×10^{-4}

Figure 22. Reduced Block Diagram of Pitch Control Law
(Inner Loop) with Two States Specified

96

$$\delta_e = K_1 \, K_q \, q + K_q \, x_1 + x_2$$

$$= K_1 \, K_q \, q + \begin{bmatrix} K_q & 1 \end{bmatrix} \begin{bmatrix} x_1 \\ x_2 \end{bmatrix} \qquad (22)$$

From Figure 22, the state equation for x_1 and x_2 can also be determined:

$$\begin{bmatrix} \dot{x}_1 \\ \dot{x}_2 \end{bmatrix} = \begin{bmatrix} -\dfrac{1}{C_1} & 0 \\ K_2 \, K_q & -C_2 \end{bmatrix} \begin{bmatrix} x_1 \\ x_2 \end{bmatrix} + \begin{bmatrix} \dfrac{K_a}{C_1} & 0 \\ 0 & K_1 \, K_2 \, K_q \end{bmatrix} \begin{bmatrix} a_z \\ q \end{bmatrix} \qquad (23)$$

But the normal acceleration a_z is given by

$$a_z = \dot{w} - U_o \, q$$

$$= Z_u \, u + Z_w \, w + Z_{\delta_e} \, \delta_e \qquad (24)$$

(using equation (13)). Finally, equations (22) and (24) can be substituted into equation (23) to yield

$$\begin{bmatrix} \dot{x}_1 \\ \dot{x}_2 \end{bmatrix} = \begin{bmatrix} \left(\dfrac{K_a \, K_q \, Z_{\delta_e} - 1}{C_1} \right) & \left(\dfrac{K_a \, Z_{\delta_e}}{C_1} \right) \\ K_2 \, K_q & -C_2 \end{bmatrix} \begin{bmatrix} x_1 \\ x_2 \end{bmatrix}$$

$$+ \begin{bmatrix} \left(\dfrac{K_a \, Z_u}{C_1} \right) & \left(\dfrac{K_a \, Z_w}{C_1} \right) & \left(\dfrac{K_1 \, K_a \, K_q \, Z_{\delta_e}}{C_1} \right) \\ 0 & 0 & K_1 \, K_2 \, K_q \end{bmatrix} \begin{bmatrix} u \\ w \\ q \end{bmatrix} \qquad (25)$$

97

Equations (11) and (14) contain the required state representation for x_1 and x_2.

The assumed roll, or aileron, inner loop control law is simply the following equation:

$$\delta_a = K_p\, p \tag{26}$$

where

$$K_p = \begin{cases} 0.1, & \bar{q} \geq 1000 \\ 0.4 - \bar{q}/3000, & 100 \leq \bar{q} < 1000 \\ 0.4, & \bar{q} < 100 \end{cases}$$
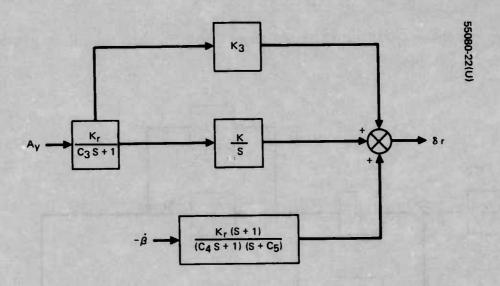
$\bar{q}$ = dynamic pressure (see Appendix A), slugs/(feet $\cdot$ sec^2)

Figure 23 shows the yaw, or rudder, inner loop control law assumed. The block diagram can be reduced to the form shown in Figure 24, wherein the states x_3, x_4, x_5, and x_6 are defined. From Figure 24, an expression for δ_r in terms of the four states can be written:

$$\delta_r = K_3\, x_3 + x_4 + x_5 + x_6 \tag{27}$$

The state equation for the four states can also be determined from Figure 5:

$$\begin{bmatrix} \dot{x}_3 \\ \dot{x}_4 \\ \dot{x}_5 \\ \dot{x}_6 \end{bmatrix} = \begin{bmatrix} -\dfrac{1}{C_3} & 0 & 0 & 0 \\ K & 0 & 0 & 0 \\ 0 & 0 & -C_5 & 0 \\ 0 & 0 & (1 - \dfrac{1}{C_4}) & -\dfrac{1}{C_4} \end{bmatrix} \begin{bmatrix} x_3 \\ x_4 \\ x_5 \\ x_6 \end{bmatrix} + \begin{bmatrix} \dfrac{K_r}{C_3} & 0 \\ 0 & 0 \\ 0 & -\dfrac{K_r}{C_4} \\ 0 & 0 \end{bmatrix} \begin{bmatrix} a_y \\ \dot{\beta} \end{bmatrix} \tag{28}$$

98

a_Y = LATERAL ACCELERATION

$C_3 = 0.5$

$C_4 = 0.03$

$C_5 = 0.33$

$K = 0.0036$

$K_3 = 0.012$

$$K_r = \begin{cases} 0.25, & \bar{q} \geq 1000 \\ 1.1 - \dfrac{\bar{q}}{1200}, & 100 \leq \bar{q} < 1000 \\ 1.0, & \bar{q} < 100 \end{cases}$$

($\bar{q}$ in $\dfrac{slugs}{ft \cdot sec^2}$)

Figure 23. Block Diagram of Yaw Control Law (Inner Loop)
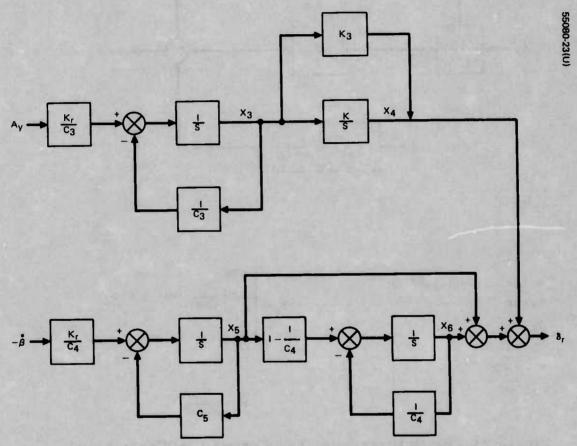
99

Figure 24. Reduced Block Diagram of Yaw Control Law
(Inner Loop) with Four States Specified

100

But the lateral acceleration a_y is given by

$$a_y = U_o \dot{\beta} + U_o r$$

$$= U_o Y_v \beta + U_o Y_{\delta_a} \delta_a + U_o Y_{\delta_r} \delta_r \qquad (29)$$

(using equation (15)). Substitution of equations (29), (15), and (27) into equation (28) eventually yields

$$
\begin{bmatrix} \dot{x}_3 \\ \dot{x}_4 \\ \dot{x}_5 \\ \dot{x}_6 \end{bmatrix}
=
\begin{bmatrix}
(F_1 K_3 - \frac{1}{C_3}) & F_1 & F_1 & F_1 \\
K & 0 & 0 & 0 \\
F_2 K_3 & F_2 & (F_2 - C_5) & F_2 \\
0 & 0 & (1 - \frac{1}{C_4}) & -\frac{1}{C_4}
\end{bmatrix}
\begin{bmatrix} x_3 \\ x_4 \\ x_5 \\ x_6 \end{bmatrix}
$$

$$
+
\begin{bmatrix}
\left(\dfrac{U_o Y_v K_r}{C_3}\right) & \left(\dfrac{K_r U_o Y_{\delta_a} K_p}{C_3}\right) & 0 \\
0 & 0 & 0 \\
\left(-\dfrac{K_r Y_v}{C_4}\right) & \left(-\dfrac{K_r Y_{\delta_a} K_p}{C_4}\right) & \dfrac{K_r}{C_4} \\
0 & 0 & 0
\end{bmatrix}
\begin{bmatrix} \beta \\ p \\ r \end{bmatrix}
\qquad (30)
$$

where

$$F_1 = \frac{K_r U_o Y_{\delta_r}}{C_3}$$

$$F_2 = -\frac{K_r Y_{\delta_r}}{C_4}$$

101

Equations (27) and (30) contain the required state representation for x_3, x_4, x_5, and x_6.

3. Determination of the Bombing Delivery Objective Function

The coordinate system used for bombing delivery calculations is the stabilized line-of-sight (LOS) system. The unit vectors are the following: $\vec{1}_R$ is along the LOS to the target, $\vec{1}_{e_s}$ is normal to $\vec{1}_R$ and in the horizontal plane, and $\vec{1}_{d_s} = \vec{1}_R \times \vec{1}_{e_s}$ is down. It is also necessary to define the space-stabilized aircraft coordinate system. The unit vectors are the following: $\vec{1}_s$ is along the aircraft heading in the horizontal plane, $\vec{j}_s$ is normal to $\vec{1}_s$ in the horizontal plane, and $\vec{k}_s = \vec{1}_s \times \vec{j}_s$ is down.

The target LOS rate about the $\vec{1}_{d_s}$ axis is denoted by ω_{d_s}. The bombing computations generate a commanded value for ω_{d_s}, given by

$$\omega_{d_{s_c}} = \left(\frac{L}{R_x + L}\right) \left(\frac{V_x \sin \eta_s}{R}\right) \tag{31}$$

The symbols and geometry are indicated in Figure 25. It can be shown that

$$\frac{V_x \sin \eta_s}{R} = \omega_{d_s} - \frac{V_y \cos \eta_s}{R} \tag{32}$$

where
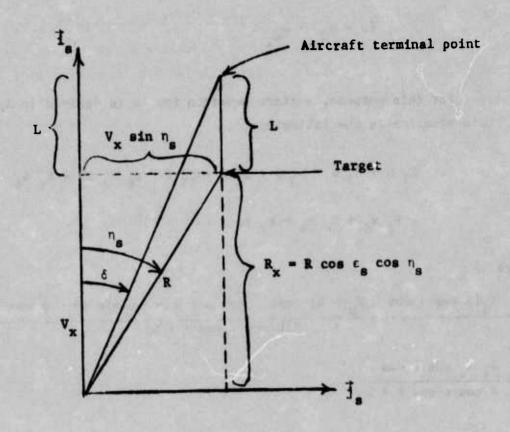
$$V_y = -w \sin \phi + W_y \approx W_y$$

$$W_y = \text{wind velocity}$$

Equation (20) can thus be written as

$$\omega_{d_{s_c}} = \left(\frac{L}{R_x + L}\right) \left[\omega_{d_s} - \frac{W_y \cos \eta_s}{R}\right] \tag{33}*$$

---

*Note that if there were no wind, the bombing command would be to diminish ω_{d_s}, eventually driving it to zero.

ϵ_s = space-stabilized elevation angle to target

η_s = space-stabilized azimuth angle to target

R = range to target

V_x = component of aircraft velocity in the $\vec{i}_s$ direction

L = horizontal trail of bomb

FIGURE 25. GEOMETRY FOR ANGLE RATE BOMBING
CROSS-PLANE SOLUTION

The objective of the autopilot control is to drive ω_{d_s} to $\omega_{d_{s_c}}$ using aileron and elevator commands. This is accomplished by driving the state

$$\delta\omega = \omega_{d_s} - \omega_{d_{s_c}} \qquad (23)\ (34)$$

to zero. For this purpose, a state equation for $\delta\omega$ is derived in Appendix VI. The state equation is the following:

$$\dot{\delta\omega} = E_1\, u + E_2\, w + E_3\, \beta + E_4\, p + E_5\, r + E_6\, K_3\, x_3 + E_6\, x_4$$

$$+ E_6\, x_5 + E_6\, x_6 + E_7\, \delta\omega \qquad (35)$$

where

$$E_1 = \frac{\lambda_1 [R \cos \epsilon \cos \eta\, X_u - R(\dot{\epsilon} \sin \epsilon \cos \eta + \dot{\eta} \cos \epsilon \sin \eta) - \dot{R} \cos \epsilon \cos \eta]}{R(R \cos \epsilon \cos \eta + L)}$$

$$E_2 = \frac{\lambda_1 X_w \cos \epsilon \cos \eta}{R \cos \epsilon \cos \eta + L}$$

$$E_3 = \frac{\lambda_1 U_o [R \cos \epsilon \cos \eta\, Y_v - R(\dot{\epsilon} \sin \epsilon \cos \eta + \dot{\eta} \cos \epsilon \sin \eta) - \dot{R} \cos \epsilon \cos \eta]}{R(R \cos \epsilon \cos \eta + L)}$$

$$E_4 = \frac{\lambda_j U_o Y_{\delta_a} K_p \cos \epsilon \cos \eta}{R \cos \epsilon \cos \eta + L}$$

$$E_5 = -\frac{\lambda_1 U_o \cos \epsilon \cos \eta}{R \cos \epsilon \cos \eta + L}$$

$$E_6 = \frac{\lambda_j U_o Y_{\delta_r} \cos \epsilon \cos \eta}{R \cos \epsilon \cos \eta + L}$$

$$E_7 = \frac{R(\dot{\epsilon} \sin \epsilon \cos \eta + \dot{\eta} \cos \epsilon \sin \eta) - \dot{R} \cos \epsilon \cos \eta}{R \cos \epsilon \cos \eta + L}$$

$$\lambda_i = \frac{-\sin \eta}{\sqrt{1 - \sin^2 \epsilon \cos^2 \eta}}$$

$$\lambda_j = \frac{\cos \epsilon \cos \eta}{\sqrt{1 - \sin^2 \epsilon \cos^2 \eta}}$$

and ϵ and η are the sensor elevation and azimuth gimbal angles, respectively.

4. Synthesis

In the previous three sections, state equations have been developed for six aerodynamic state variables (equation (21)), six inner loop control states (equations (23) and (28)), and one bombing delivery state (equation (35)). It is now necessary to synthesize the three state equations into one, taking advantage of equations (26) and (27). The resulting state equation is shown on the following page. It should be noted that equations (21), (23), and (28), equation (63) of Appendix VI are used to determine how the additive controls $\Delta \delta_e$ and $\Delta \delta_a$ affect the thirteen states.

5 Discretization Procedure

Equation (25) represents a state equation of the standard form

$$\dot{\vec{x}} = A \vec{x} + B \vec{u}$$

where

$\vec{x}$ is the 13 x 1 state vector

A is 13 x 13

B is 13 x 2

$\vec{u}$ is the 2 x 1 control vector.

The autopilot controls are to be implemented digitally every T seconds. It is therefore necessary to discretize equation (36). The state transition

105

$$
\begin{bmatrix} \dot{u} \\ \dot{w} \\ \dot{q} \\ \dot{x}_1 \\ \dot{x}_2 \\ \dot{\beta} \\ \dot{p} \\ \dot{r} \\ \dot{x}_3 \\ \dot{x}_4 \\ \dot{x}_5 \\ \dot{x}_6 \\ \dot{\delta\omega} \end{bmatrix}
=
\underbrace{\begin{bmatrix}
X_u & X_w & 0 & 0 & 0 & & & & & & & & 0 \\
Z_u & Z_w & (U_o+Z_{\delta_e}K_1K_q) & (Z_{\delta_e}K_q) & Z_{\delta_e} & & & & & & & & 0 \\
M_u & M_w & (M_q+M_{\delta_e}K_1K_q) & (M_qK_q) & M_{\delta_e} & & & & & & & & 0 \\
\left(\dfrac{K_aZ_u}{C_1}\right) & \left(\dfrac{K_aZ_w}{C_1}\right) & F_3 & F_4 & \left(\dfrac{K_aZ_{\delta_e}}{C_1}\right) & & & & & & & & 0 \\
0 & 0 & K_1K_2K_q & K_2K_q & -C_2 & & & & & & & & 0 \\
 & & & & & Y_v & Y_{\delta_a}K_p & -1 & Y_{\delta_r}K_3 & Y_{\delta_r} & Y_{\delta_r} & Y_{\delta_r} & 0 \\
 & & & & & L & (L_p+L_{\delta_a}K_p) & L_r & L_{\delta_r}K_3 & L_{\delta_r} & L_{\delta_r} & L_{\delta_r} & 0 \\
 & & & & & N & (N_p+N_{\delta_a}K_2) & N_r & N_{\delta_r}K_3 & N_{\delta_r} & N_{\delta_r} & N_{\delta_r} & 0 \\
 & & & & & \left(\dfrac{U_oK_rY_v}{C_3}\right) & \left(\dfrac{U_oK_rY_{\delta_a}K_p}{C_3}\right) & 0 & \left(F_1K_3-\dfrac{1}{C_3}\right) & F_1 & F_1 & F_1 & 0 \\
 & & & & & 0 & 0 & 0 & K & 0 & 0 & 0 & 0 \\
 & & & & & -\dfrac{K_rY_v}{C_4} & -\dfrac{K_rY_{\delta_a}K_p}{C_4} & \dfrac{K_r}{C_4} & F_2K_3 & F_2 & (F_2-C_5) & F_2 & 0 \\
 & & & & & 0 & 0 & 0 & 0 & 0 & \left(1-\dfrac{1}{C_4}\right) & \left(-\dfrac{1}{C_4}\right) & 0 \\
E_1 & E_2 & 0 & 0 & 0 & E_3 & E_4 & E_5 & K_3E_6 & E_6 & E_6 & E_6 & E_7
\end{bmatrix}}_{A}
\begin{bmatrix} u \\ w \\ q \\ x_1 \\ x_2 \\ \beta \\ p \\ r \\ x_3 \\ x_4 \\ x_5 \\ x_6 \\ \delta\omega \end{bmatrix}
$$

$$
+\underbrace{\begin{bmatrix}
0 & 0 \\
Z_{\delta_e} & 0 \\
M_{\delta_e} & 0 \\
\left(\dfrac{K_aZ_{\delta_e}}{C_1}\right) & 0 \\
0 & 0 \\
0 & Y_{\delta_a} \\
0 & L_{\delta_a} \\
0 & N_{\delta_a} \\
0 & \left(\dfrac{K_rU_oY_{\delta_a}}{C_3}\right) \\
0 & 0 \\
0 & \left(-\dfrac{K_rY_{\delta_a}}{C_4}\right) \\
0 & 0 \\
0 & E_4
\end{bmatrix}}_{B}
\underbrace{\begin{bmatrix} \Delta\delta_e \\ \Delta\delta_a \end{bmatrix}}_{\vec{u}}
\qquad (36)
$$

$$F_1 = \frac{K_rU_oY_{\delta_r}}{C_3}$$

$$F_2 = -\frac{K_rY_{\delta_r}}{C_4}$$

$$F_3 = \frac{Z_{\delta_e}K_1K_aK_2}{C_1}$$

$$F_4 = \frac{K_aZ_{\delta_e}K_q-1}{C_1}$$

matrix is given by

$$\Phi \overset{\Delta}{=} \Phi(0, T) = e^{AT} \tag{37}$$

(see, for example, Reference 4). Equation (37) must be evaluated numerically, using the series expansion for the exponential. The <u>discretized</u> <u>state</u> <u>equation</u> then becomes

$$\vec{x}(n+1) = \Phi \, \vec{x}(n) + \Psi \, \vec{u}(n) \tag{27} \ \ (38)$$

where

$$\Psi = \int_{0}^{T} \Phi \, B \, d\tau = \Phi \, B \, T \tag{39}$$

It should be noted that Φ is assumed to be time-invariant. While this is not strictly true because Φ is a function of external target data $(R, \epsilon, \eta, \dot{\epsilon}, \dot{\eta})$, no other information about Φ in the future is available; solution of the discrete time optimal control problem requires future knowledge of Φ (as is seen in the next section). Moreover, it is not likely that Φ will actually vary much over the duration of the autopilot-controlled flight.

6. <u>Definition of the Optimal Control Problem</u>

The system (Φ, ψ) illustrated in Figure 26 is <u>controllable</u> since the matrix

$$[\Psi \mid \Phi\Psi \mid \Phi^2\Psi \mid - - - \mid \Phi^{12}\Psi]$$

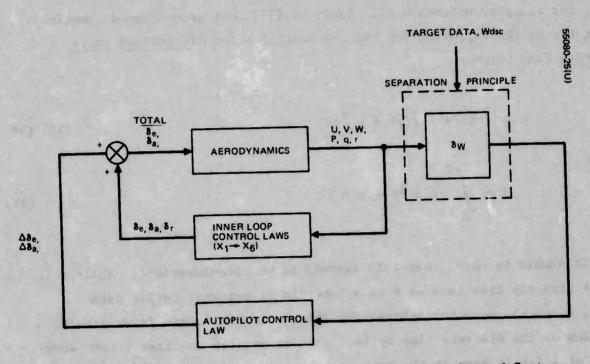has rank 13. This statement would not be true if only one deflection angle were used as a control.

107

Figure 26. Detailed Block Diagram of Tactical Autopilot Control System

Define

$$J_N = \sum_{i=1}^{N} \vec{x}^T(i)\ Q(i)\ \vec{x}(i) + \vec{u}^T(i-1)\ \bar{R}(i-1)\ \vec{u}(i-1) \qquad (40)$$

where

$$Q = \begin{bmatrix} 0 & & & & & & & & & & & & \\ & 0 & & & & & & & & & & & \\ & & q_3 & & & & & & & & & & \\ & & & 0 & & & & & & & & & \\ & & & & 0 & & & & & & & & \\ & & & & & 0 & & & & & & & \\ & & & & & & q_7 & & & & & & \\ & & & & & & & q_8 & & & & & \\ & & & & & & & & 0 & & & & \\ & & & & & & & & & 0 & & & \\ & & & & & & & & & & 0 & & \\ & & & & & & & & & & & 0 & \\ & & & & & & & & & & & & q_{13} \end{bmatrix}$$

and

$$\bar{R} = \begin{bmatrix} R_1 & 0 \\ 0 & R_2 \end{bmatrix}$$

(Both Q and R must be positive semidefinite matrices.) The optimal control
problem for the tactical autopilot is to determine a control law for
equation (38) (and Figure 7) which minimizes J_N (for some arbitrarily large N).

109

The values q_3, q_7, q_8, q_{13} and R_1, R_2 are "levers," costs associated with undesirable values of states and with control effort, respectively. The values assumed are the following:

$$q_3 = q_7 = q_8 = 1$$

$$q_{13} = 50$$

$$R_1 = 100$$

$$R_2 = 1$$

The terms q_3, q_7, and q_8 are non-zero because a secondary objective is to achieve zero Euler angle rates. The term R_1 is so large because $\Delta\delta_a$ is the preferred control; therefore, control via $\Delta\delta_e$ must be made relatively costly.

The value of N is chosen to be arbitrarily large. This is done to force the controller to achieve its objective (primarily to drive $\delta\omega$ to zero) as quickly as possible <u>and</u> <u>to</u> <u>maintain</u> it. If N were finite, it could not be guaranteed that the cost function J_n would not be excessive for $n \gg N$. (Such considerations are discussed in Reference 5, among other places.)

If it were only desired to drive $\delta\omega$ to zero, the control problem could be treated as an output regulator problem. That is, the state vector could be formed with the first 12 elements, and the output would be equation (24). This approach is equivalent to that formulated here if $q_3 = q_7 = q_8 = 0$.

7. Solution of the Matrix Riccati Equation

The optimal control law for the linear regulator problem formulated in the previous section is the linear feedback control law

$$\vec{u}(n) = S(n) \, \vec{x}(n) \tag{41}$$

where the 2 x 13 feedback control matrix $S(n)$ is determined recursively from

the following equations:*

$$S(n) = - [\psi^T \, K(n+1) \, \psi + \overline{R}]^{-1} \, \psi^T \, K(n+1) \, \phi \tag{42}$$

$$K(n) = \phi^T \, K(n+1) \, \phi + \phi^T \, K(n+1) \, \psi \, S(n) + Q \tag{43}$$

solved backward in time. Since the terminal time N is arbitrarily large, the terminal condition for recursive solution of equations (42) and (43) is

$$K(N) = 0 \tag{44}$$

and only the steady-state solution for S is required. That is, steady-state solution of equations (42)-(44) yields a constant gain matrix S^*. The autopilot control law is then

$$\vec{u}(n) = S^* \, \vec{x}(n) \tag{45}$$

8. Recommended Control Law

Equations (42)-(44) are solved by means of a digital computer program. In this program, the discretization process of equations (37) and (39) is first performed (numerically). Then the gain matrix S^* is computed, given the costs assumed earlier. This computer program is described and listed in Appendix C.

The matrices ϕ and ψ involved in equations (42) and (43) depend on target data (because of the bombing delivery state $\delta\omega$). This target data is the following:

$$R, \; \epsilon, \; \eta, \; \dot{\epsilon}, \; \dot{\eta} \; .$$

(Of course, the matrices also depend on aerodynamic quantities, for which values have been assumed in Appendix I.) Using the simulation, S^* has been

*See, for example, References 4 and 6. These equations together comprise the matrix Riccati difference equation.

111

computed for various values of the five quantities.[*] The following conclusions have been reached:

(1) the small values of η, $\dot{\epsilon}$, and $\dot{\eta}$ which would be expected in the bombing delivery situation have no appreciable effect on S^*

(2) as long as ϵ is not over approximately 30°, S^* will not vary

(3) two elements of S^* depend on range

The constant values of S^* are listed below (to 3 significant figures):

$$S^*(1, 1) = -9.70 \times 10^{-3}$$

$$S^*(1, 2) = -2.86 \times 10^{-2}$$

$$S^*(1, 3) = 0.213$$

$$S^*(1, 4) = 2.69 \times 10^{-2}$$

$$S^*(1, 5) = 50.7$$

$$S^*(2, 6) = -50.9$$

$$S^*(2, 7) = 7.03 \times 10^{-2}$$

$$S^*(2, 8) = 0.659$$

$$S^*(2, 9) = -3.48 \times 10^{-3}$$

$$S^*(2, 10) = 3.22$$

$$S^*(2, 11) = -0.142$$

$$S^*(2, 12) = -0.154$$

(46)

Values of the two range-dependent terms are given in Table 14. All other elements of the gain matrix S^* are zero. The values of S^* in Table 14

[*]It is assumed that $T = 0.050$ sec and $L = 2000$ ft.

TABLE 14. RANGE-DEPENDENT GAIN TERMS

Range, n. miles	$s^*(2, 1)$	$s^*(2, 13)$
0.5	3.76×10^{-2}	1.59×10^2
1.0	7.54×10^{-3}	88.7
1.5	6.24×10^{-3}	1.56×10^2
2.0	9.62×10^{-3}	4.90×10^2
2.5	-7.52×10^{-2}	-8.64×10^3
3.0	6.57×10^{-3}	2.75×10^3
3.5	-4.15×10^{-4}	2.92×10^2
4.0	-4.29×10^{-4}	1.13×10^2

are curve-fit for ease of mechanization. The resulting expressions are:

$$s^*(2, 1) \approx (-4.59 \times 10^{-3}) + \frac{(1.96 \times 10^{-2})}{R} \qquad (47)$$

$$s^*(2, 13) \approx (1.07 \times 10^4) - (4.95 \times 10^4)\, R + (8.61 \times 10^4)\, R^2$$

$$- (7.23 \times 10^4)\, R^3 + (3.12 \times 10^4)\, R^4$$

$$- (6.60 \times 10^3)\, R^5 + 535\, R^6 \qquad (48)$$

where R is expressed in n. miles.

The quantity ω_{d_s} is in fact a noisy quantity. It is smoothed with a Kalman Filter.   The well known Separation Principle (Reference 4) states that the optimal stochiastic control system consists of

the optimal filter in cascade with the deterministic optimal controller.
Therefore, the estimate of $\delta\omega$ should be used. The <u>recommended</u> <u>control</u> <u>law</u>
is the following:

$$\Delta\delta_e = S^*(1,\,1)\,u + S^*(1,\,2)\,w + S^*(1,\,3)\,q + S^*(1,\,4)\,x_1$$

$$+ S^*(1,\,5)\,x_2 \tag{49}$$

$$\Delta\delta_a = S^*(2,\,1)\,u + S^*(2,\,6)\,\beta + S^*(2,\,7)\,p + S^*(2,\,8)\,r + S^*(2,\,9)\,x_3$$

$$+ S^*(2,\,10)\,x_4 + S^*(2,\,11)\,x_5 + S^*(2,\,12)\,x_6$$

$$+ S^*(2,\,13)\,[\hat{\omega}_{d_s} - \omega_{d_{s_c}}] \tag{50}$$

where the elements of S^* are given by equations (46)-(48),

$\hat{\omega}_{d_s}$ is the smoothed estimate of ω_{d_s} from the Kalman Filter

$\omega_{d_{s_c}}$ is the command from the bombing delivery calculations

and $\Delta\delta_e$ and $\Delta\delta_a$ are in radians.

The quantities $\Delta\delta_e$ and $\Delta\delta_a$ must be applied over tne entire period (of
duration T seconds).

APPENDIX V

STABILITY DERIVATIVES

The following values are assumed for the longitudinal and lateral aerodynamic terms:

$$X_u = - \frac{\rho \, s \, U_o (C_D + C_{Du})}{m}$$

$$X_w = \frac{\rho \, s \, U_o (C_L - C_{D_\alpha})}{2m}$$

$$Z_u = - \frac{\rho \, s \, U_o (C_L + C_{Lu})}{m}$$

$$Z_w = - \frac{\rho \, s \, U_o (C_{L_\alpha} + C_D)}{m}$$

$$Z_{\delta_e} = - \frac{\rho \, s \, U_o^2 \, C_{L_{\delta_e}}}{2m}$$

$$M_u = \frac{\rho \, s \, U_o \, c \, C_{m_u}}{I_y}$$

$$M_w = \frac{\rho \, s \, U_o \, c \, C_{m_\alpha}}{2I_y}$$

$$M_q = \frac{\rho \, s \, U_o \, c^2 \, C_{m_q}}{4I_y}$$

$$M_{\delta_e} = \frac{\rho s U_o^2 c C_{m_{\delta_e}}}{2I_y}$$

$$Y_v = \frac{\rho s U_o C_{y_\beta}}{2m}$$

$$Y_{\sigma_a} = \frac{\rho s U_o C_{y_{\delta_a}}}{2m}$$

$$Y_{\delta_r} = \frac{\rho s U_o C_{y_{\delta_r}}}{2m}$$

$$L_\beta = \frac{\rho s U_o b^2 C_{L_\beta}}{2I_x}$$

$$L_p = \frac{\rho s U_o b^2 C_{L_p}}{4I_x}$$

$$L_r = \frac{\rho s U_o b^2 C_{L_r}}{4I_x}$$

$$L_{\delta_a} = \frac{\rho s U_o^2 b C_{L_{\delta_a}}}{2I_x}$$

$$L_{\delta_r} = \frac{\rho s U_o^2 b C_{L_{\delta_r}}}{2I_x}$$

116

$$N_\beta = \frac{\rho \, s \, U_o^2 \, b \, C_{N_\beta}}{2 I_z}$$

$$N_p = \frac{\rho \, s \, U_o \, b^2 \, C_{N_p}}{4 I_z}$$

$$N_r = \frac{\rho \, s \, U_o \, b^2 \, C_{N_r}}{4 I_z}$$

$$N_{\delta_a} = \frac{\rho \, s \, U_o^2 \, b \, C_{N_{\delta_a}}}{2 I_z}$$

$$N_{\delta_r} = \frac{\rho \, s \, U_o^2 \, b \, C_{N_{\delta_r}}}{2 I_z}$$

where

ρ = atmospheric density = 0.00238 slugs/ft^3

s = wing area = 375 ft^2

b = wing span = 38.73 ft

c = mean aerodynamic chord = 10.84 ft

U_o = trim air speed = 1000 ft^2

m = aircraft mass = 940 slugs

I_x = 24,899 slugs ft^2

I_y = 70,497 slugs ft^2

I_z = 89,050 slugs ft^2

117

and

$$C_D = 0.0276$$

$$C_L = 0.0665$$

$$C_{D_u} = 0.022$$

$$C_{L_u} = 0.022$$

$$C_{D_\alpha} = 0.0665$$

$$C_{L_\alpha} = 4.8$$

$$C_{L_{\delta_e}} = 0.378$$

$$C_{m_u} = 0.0329$$

$$C_{m_\alpha} = -0.478$$

$$C_{m_{\delta_e}} = -0.6$$

$$C_{m_q} = -3.54$$

$$C_{y_\beta} = 0.773$$

$$C_{y_{\delta_r}} = 0.0917$$

$$C_{y_{\delta_a}} = 0.0257$$

$$C_{L_r} = 0.0862$$

$$C_{L_p} = -0.385$$

$$C_{L_\beta} = 0.0831$$

$$C_{L_{\delta_r}} = 0.00985$$

$$C_{L_{\delta_a}} = -0.0549$$

118
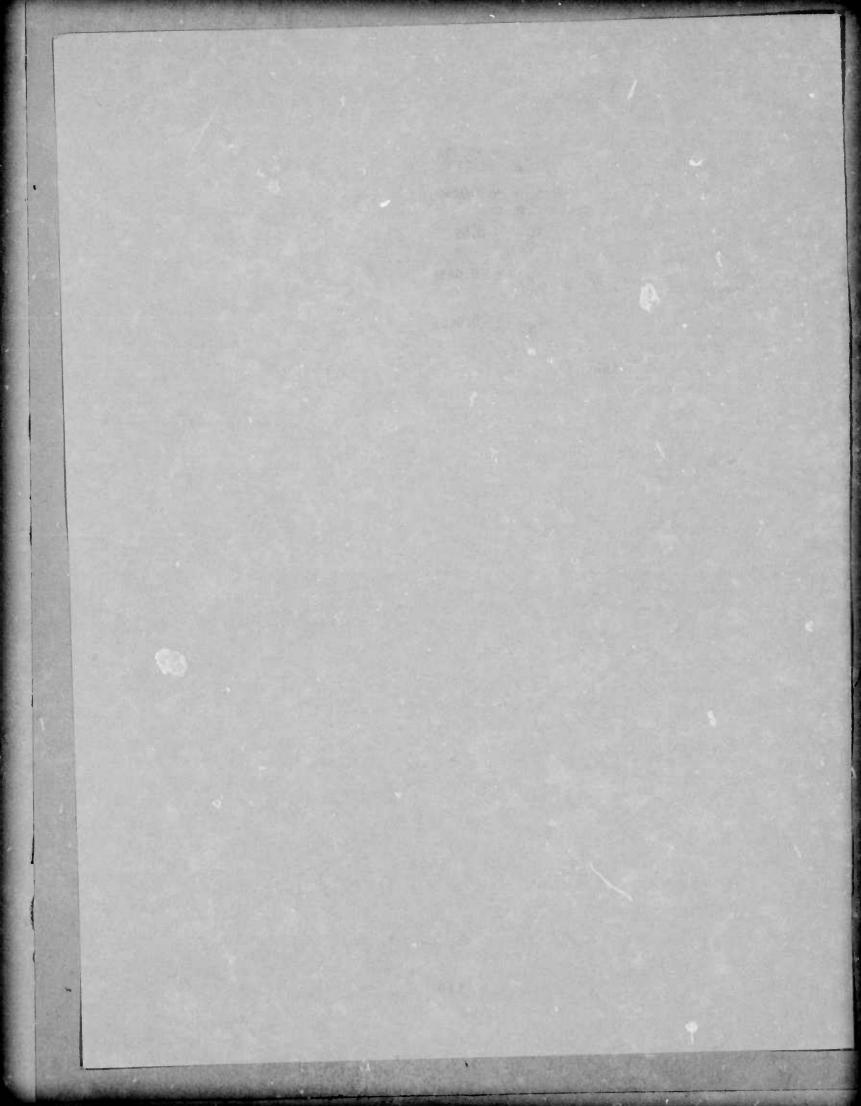
$$C_{N_r} = -0.324$$

$$C_{N_p} = 0.0244$$

$$C_{N_\beta} = 0.09$$

$$C_{N_{\delta_r}} = -0.0458$$

$$C_{N_{\delta_a}} = -0.0905$$

DERIVATION OF STATE EQUATION FOR $\delta\omega$

Equation (23) of the text may be written as

$$\delta\omega = (\frac{R_x}{R_x + L})\ \omega_{d_s} - (\frac{L}{R_x + L})\ (\frac{W_y\ \cos\ \eta_s}{R}) \tag{51}$$

A state equation for $\delta\omega$ is obtained by differentiating equation (B-1):

$$\dot{\delta\omega} = \frac{d(\delta\omega)}{dt} = -\frac{\dot{R}_x}{(R_x + L)^2}\left[R_x\ \omega_{d_s} - \frac{L\ W_y\ \cos\ \eta_s}{R}\right]$$

$$+ \frac{1}{(R_x + L)}\left[\dot{R}_x\ \omega_{d_s} + R_x\ \dot{\omega}_{d_s} + \frac{L\ W_y\ \cos\ \eta_s\ \dot{R}}{R^2} + \frac{L\ W_y\ \dot{\eta}_s\ \sin\ \eta_s}{R}\right]$$

$$= \left[\frac{\dot{R}_x}{R_x + L} - \frac{\dot{R}_x\ R_x}{(R_x + L)^2}\right]\ \omega_{d_s} - \left[-\frac{\dot{R}}{R} - \frac{\dot{R}_x}{(R_x + L)}\right]\left[\frac{L\ W_y\ \cos\ \eta_s}{R(R_x + L)}\right]$$

$$+ \frac{1}{(R_x + L)}\left[R_x\ \dot{\omega}_{d_s} + \frac{L\ W_y\ \dot{\eta}_s\ \sin\ \eta_s}{R}\right] \tag{52}$$

where it is assumed that

$$\dot{W}_y = \dot{L} \approx 0\ .$$

A state equation should be a linear function of $\delta\omega$, so terms must be rearranged:

121

$$\dot{\delta\omega} = - \left(\frac{\dot{R}_x}{R_x + L}\right) \left[\frac{R_x}{R_x + L} \omega_{d_s} - \left(\frac{L}{R_x + L}\right) \frac{W_y \cos \eta_s}{R}\right]$$

$$+ \frac{1}{(R_x + L)} \left[\dot{R}_x \omega_{d_s} + \frac{\dot{R} L W_y \cos \eta_s}{R^2} + R_x \dot{\omega}_{d_s} + \frac{L W_y \dot{\eta}_s \sin \eta_s}{R}\right] \qquad (53)$$

Now, using the fact that

$$\omega_{d_s} \overset{\Delta}{=} \frac{V_{e_s}}{R} \qquad (54)$$

and using equation (50), equation (52) becomes

$$\dot{\delta\omega} = - \frac{\dot{R}_x}{(R_x + L)} \ \delta\omega + \left(\frac{1}{R_x + L}\right) \left(\frac{R \dot{R}_x - 2R_x \dot{R}}{R^2}\right) V_{e_s} + \left[\frac{R_x}{R(R_x + L)}\right] a_{e_s}$$

$$+ \left(\frac{1}{R_x + L}\right) \left[\frac{L \dot{R} W_y \cos \eta_s}{R^2} + \frac{L W_y \dot{\eta}_s \sin \eta_s}{R}\right] \qquad (55)$$

For small Euler angles,

$$V_{e_s} \approx u(\vec{i} \cdot \vec{i}_{e_s}) + v(\vec{j} \cdot \vec{i}_{e_s}) + w(\vec{k} \cdot \vec{i}_{e_s})$$

$$\approx \lambda_i u + \lambda_j v \qquad (56)$$

where

$$\lambda_i = \frac{-\sin \eta}{\sqrt{1 - \sin^2 \iota \cos^2 \eta}} \qquad (57)$$

$$\lambda_j = \frac{\cos \iota \cos \eta}{\sqrt{1 - \sin^2 \iota \cos^2 \eta}} \qquad (58)$$

122

and ϵ and η are the elevation and azimuth gimbal angles, respectively. Similarly,

$$a_{e_s} = \lambda_1 \dot{u} + \lambda_j \dot{v} \tag{59}$$

Also, it can be shown that

$$R_x = R \cos \epsilon \cos \eta \tag{60}$$

and

$$\dot{R}_x = \dot{R} \cos \epsilon \cos \eta + R \, [\dot{\theta} \sin \epsilon \cos \eta - \dot{\epsilon} \sin \epsilon \cos \eta$$

$$- \dot{\eta} \cos \epsilon \sin \eta]$$

$$\approx \dot{R} \cos \epsilon \cos \eta - R \, [\dot{\epsilon} \sin \epsilon \cos \eta - \dot{\eta} \cos \epsilon \sin \eta] \tag{61}$$

The terms in brackets in equation (55) are judged to be relatively small. Thus, substitution of equations (56) and (59) into equation (55) yields

$$\dot{\delta\omega} = - \frac{\dot{R}_x}{R_x + L} \, \delta\omega + \left(\frac{R \, \dot{R}_x - 2R_x \, \dot{R}}{R^2} \right) \left(\frac{\lambda_1}{R_x + L} \right) u + \left(\frac{R \, \dot{R}_x - 2R_x \, \dot{R}}{R^2} \right) \left(\frac{\lambda_1}{R_x + L} \right) v$$

$$+ \left[\frac{R_x \, \lambda_1}{R(R_x + L)} \right] \dot{u} + \left[\frac{R_x \, \lambda_1}{R(R_x + L)} \right] \dot{v} \tag{62}$$

with the associated equations (57), (58), (60), and (61). But the accelerations $\dot{u}$ and $\dot{v}$ are given by equations (12) and (14) of the text, respectively, so

123

$$\dot{\delta\omega} = \left(-\frac{\dot{R}_x}{R_x + L}\right)\delta\omega + \frac{\lambda_1}{R(R_x + L)}\left[\frac{R\dot{R}_x - 2R_x\dot{R}}{R} + R_x X_u\right]u + \left[\frac{R_x \lambda_1 X_w}{R(R_x + L)}\right]w$$

$$+ \left[\frac{\lambda_1 U_o}{R(R_x + L)}\right]\left[\frac{R\dot{R}_x - 2R_x\dot{R}}{R} + R_x Y_v\right]\beta - \left[\frac{R_x \lambda_1 U_o}{R(R_x + L)}\right]r$$

$$+ \left[\frac{R_x \lambda_j U_o Y_{\delta_a}}{R(R_x + L)}\right]\delta_a + \left[\frac{R_x \lambda_j U_o Y_{\delta_r}}{R(R_x + L)}\right]\delta_r \tag{63}$$

Substitution of equations (26) and (27) for δ_a and δ_r, respectively, into equation (B-13) results in the final equation:

$$\dot{\delta\omega} = \left[\frac{\lambda_1}{R(R_x + L)}\left(\frac{R\dot{R}_x - 2R_x\dot{R}}{R} + R_x X_u\right)\right]u + \left[\frac{R_x \lambda_1 X_w}{R(R_x + L)}\right]w$$

$$+ \left[\frac{\lambda_1 U_o}{R(R_x + L)}\left(\frac{R\dot{R}_x - 2R_x\dot{R}}{R} + R_x Y_v\right)\right]\beta + \left[\frac{R_x \lambda_j U_o Y_{\delta_a} K_p}{R(R_x + L)}\right]p$$

$$- \left[\frac{R_x \lambda_1 U_o}{R(R_x + L)}\right]r + \left[\frac{R_x \lambda_j U_o Y_{\delta_r} K_3}{R(R_x + L)}\right]x_3 + \left[\frac{R_x \lambda_j U_o Y_{\delta_r}}{R(R_x + L)}\right]x_4$$

$$+ \left[\frac{R_x \lambda_j U_o Y_{\delta_r}}{R(R_x + L)}\right]x_5 + \left[\frac{R_x \lambda_j U_o Y_{\delta_r}}{R(R_x + L)}\right]x_6 - \left(\frac{\dot{R}_x}{R_x + L}\right)\delta\omega \tag{64}$$

Equation (64) is accompanied by equations (57), (58), (60), and (61).

APPENDIX VII

SUPPLEMENTAL TRIAL SERIES

INTRODUCTION AND SUMMARY

A supplemental trial series was performed during the period of May through August 1975 to explore in greater depth the impact of wind, altitude, and task priorities on pilot performance. A total of 200 weapon delivery task trials were conducted. These trials provided weapon delivery and pilot workload data which may be used to further substantiate the conclusions of the trial series.

The test conditions of the initial series were retained for the supplemental trials. These conditions are identified below and are described in detail in the main body of the report as referenced.

- TDS/Simulation System - The major simulation system features --- computed azimuth lead (CAL) steering, manual and autopilot flight control, automatic weapon release, and the head-up display (HUD) --- were retained for this series.

- Terminal Attack Tasks - The weapon delivery tasks --- target sighting, target acquisition, target tracking, aircraft steering, weapon release, and external target detection --- were identical for the supplemental series.

- Subjects and Training - The four pilots who have participated in the two previous studies again served as the subjects for this series. Familiarization with the 6000 foot altitude and random wind conditions was provided prior to initiating the trials.

- Recorded Data - Cross-track miss distance and external light detections were the primary data items which were recorded and analyzed.

Three major factors were varied. The no-wind and single-crosswind conditions were broadened to provide a random-wind situation. The altitude ceiling was raised to 6000 feet. Finally, the operating priority under which the individual trial was performed was varied between the primary weapon delivery task and the detection of the light targets external to the cockpit.

The data provided by the 200 supplemental trials are presented in detail in Tables 15 through 20 and Figures 27 through 30. These data support the following major conclusions:

- The presence of a random-wind factor does not significantly affect manual weapon delivery performance. The use of auto-pilot reduced cross-track miss distances 47 percent (16.4 to 8.7 feet) in the random-wind situation. In this series, the autopilot performance was equal to earlier no-wind trials.

- When operating in a minimum time attack situation (such as that imposed by a 6000 foot operating altitude), the autopilot function serves to significantly improve weapon delivery performance over manually controlled flight.

- A predetermined task priority (weapon delivery or external target detection) has no discernible impact on pilot performance of either the weapon delivery task or external light detection. It would appear that the requirements of the tactical situation will be dominant in establishing task priorities during the weapon delivery process.

WIND

The initial trial series included a set of 40 trials in which a wind factor was added to the trial conditions. The value which was used was 270 degrees at 40 knots -- a left crosswind component. The wind factor was the same for all 20 trials. Weapon delivery accuracies were virtually identical for the wind factor series when compared to no-wind trials when flying manually. Workloads did, however, show a significant increase when the wind factor was present.

In further analysis of these data, the impact of training was considered. Did the pilots perform well in the wind situation because they had learned the correct action for the given wind condition? This query prompted the expansion of the single-wind condition to a somewhat random set of five wind conditions. Crosswinds of 270 degrees/40 knots, 315 degrees/20 knots, 45 degrees/20 knots, and 90 degrees/40 knots plus a no-wind condition were presented to the pilot in random order through his set of 20 trials (ten manual, ten autopilot). This approach forced the pilot to react to the steering commands on the HUD rather than being able to anticipate the required corrections.

The results of the random-wind trials were again virtually identical to the no-wind and fixed-wind conditions when flying manually. However, when using the autopilot in the random-wind condition, the cross track miss distances were comparable (8.7 to 8.5 feet) to the results achieved in the no-wind condition (Table 1). This would indicate that the autopilot control technique used in the simulation system is capable of completely neutralizing

TABLE 15. CROSS-TRACK MISS DISTANCE VERSUS WIND FACTORS

Subject	Average Miss Distance, feet					
	No wind		Fixed wind		Random wind	
	Manual Flight Control	Autopilot	Manual Flight Control	Autopilot	Manual Flight Control	Autopilot
1	13.4	8.8	21.6	14.6	17.3	7.0
2	12.4	10.0	12.0	17.4	13.6	7.4
3	16.8	7.6	7.6	18.0	15.5	8.1
4	16.2	7.8	18.2	13.2	19.2	12.3
Average	14.6	8.5	14.8	15.8	16.4	8.7

127

TABLE 16. MISSED LIGHTS VERSUS WIND FACTORS

Missed Lights, percent

Subject	No wind		Fixed wind		Random wind	
	Manual Flight Control	Autopilot	Manual Flight Control	Autopilot	Manual Flight Control	Autopilot
1	10.8	13.4	28.2	18.4	17.6	13.9
2	12.8	14.6	13.0	12.6	18.0	17.1
3	29.6	24.4	37.6	32.2	48.5	27.0
4	24.2	23.4	55.0	35.2	42.9	13.9
Average	19.3	18.9	32.8	24.7	31.8	18.0

128

TABLE 17. CROSS-TRACK MISS DISTANCE VERSUS ALTITUDE

| Subject | Altitude, feet | | | | | |
| | 1000 | | 5000 | | 6000 | |
	Manual Flight Control	Autopilot	Manual Flight Control	Autopilot	Manual Flight Control	Autopilot
1	13.4	8.8	20.6	8.0	16.4	13.3
2	12.4	10.0	18.2	12.0	48.2	10.7
3	16.8	7.6	32.6	10.0	20.3	11.6
4	16.2	7.8	41.6	13.2	38.6	8.9
Average	14.6	8.5	28.2	10.3	30.9	11.1

TABLE 18. MISSED LIGHTS VERSUS ALTITUDE

Altitude, feet

Subject	1000		5000		6000	
	Manual Flight Control	Autopilot	Manual Flight Control	Autopilot	Manual Flight Control	Autopilot
1	10.8	13.4	16.0	20.4	22.1	23.6
2	12.8	14.6	43.4	25.4	25.8	15.5
3	29.6	24.4	36.0	33.6	53.2	32.1
4	24.2	23.4	58.2	33.2	43.1	15.5
Average	19.3	18.9	37.3	27.7	36.1	21.7

TABLE 19. 6000 FOOT, RANDOM WIND CROSS-TRACK
MISS DISTANCES

Subject	Manual Flight Control	Autopilot
1	36.9	23.2
2	50.4	22.4
Average	43.7	22.8

TABLE 20. 6000 FOOT/RANDOM WIND MISSED LIGHTS,
percent

Subject	Manual Flight Control	Autopilot
1	34.5	13.2
2	48.9	39.3
Average	41.7	26.3

the impact of wind conditions. In so doing, a significant (47 percent) improvement in weapon delivery accuracy may be realized through use of autopilot control.

External target detection performance (Table 16) remained relatively constant for all trials where wind was a factor. As indicated in the initial trial series, there is a significant increase in workload in terms of the percentage of missed lights (no wind-19.3 percent, fixed wind-32.8 percent, random wind-31.8 percent) when a wind factor is present.

ALTITUDE

The increase of altitude from 1000 to 5000 feet and the resulting decrease in the time available for target designation and steering corrections to the weapon release point had a twofold impact on pilot performance. Weapon delivery accuracies decreased, and pilot workloads increased. The impact was most significant when the pilot was flying manually.

A supplemental trial series of 80 trials was directed to an examination of pilot performance at a maximum detection altitude. Using a 5 miles simulated detection range and an 11 degree down HUD field of view, the maximum detection altitude is approximately 6000 feet. At this altitude, the pilot has an interval of from 3 to 5 seconds to acquire the target following its
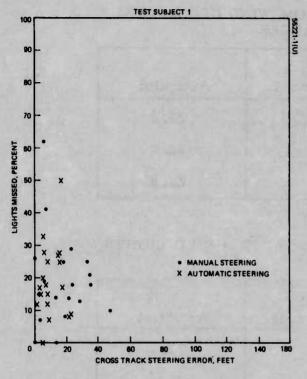
131

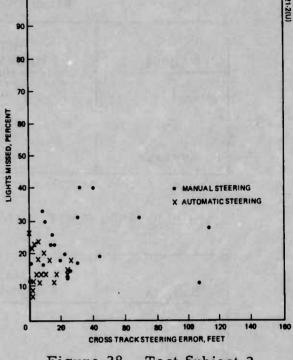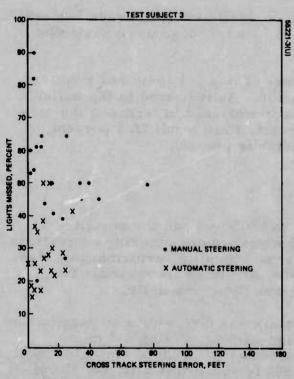Figure 27. Test Subject 1

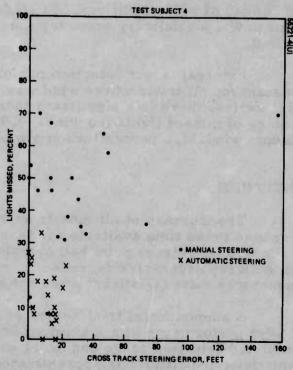Figure 28. Test Subject 2

Figure 29. Test Subject 3

Figure 30. Test Subject 4

132

initial appearance, and approximately 10 seconds to make any required steering corrections to the weapon release point. It is only because of the provision for the off-HUD symbology that the attack can be made at these geometries.

Overall performance at 6000 feet (Table 17) was virtually identical to that which was recorded for the 5000-foot series. Cross-track miss distance when flying manually at 6000 feet averaged 30.9 feet as compared to 28.2 feet for the 5000-foot trials. These data confirm the previous conclusion that reduced operating time imposed by increased operating altitude adversely affects weapon delivery performance.

When operating on autopilot, the 11.1 foot average cross-track miss distance again confirmed the capabilities of automatic flight control in significantly improving weapon delivery performance over that achieved when flying manually.

Pilot workloads in terms of external target detection were significantly influenced when flying manually at 6000 feet (Table 18). At this altitude 36.1 percent of the lights were missed (37.3 percent at 3000 feet), reflecting a major increase over the 19.3 percent missed when operating at 1000 feet.

In summary, the reduced operating times imposed by higher flight altitudes reduce weapon delivery accuracies and increase workloads when flying manually. When autopilot flight controls features are available, comparable performance levels may be maintained through the available operating altitudes.

WIND/ALTITUDE

A final series of 40 trials which combined the 6000 foot and random wind conditions were performed by two of the four pilot subjects. It was anticipated that the severe demands imposed by this combination of conditions would significantly influence both weapon delivery accuracies and pilot workload.

The limited data reflected in Table 19 indicates that the combination of a random wind and a maximum operating altitude has virtually an additive impact on weapon delivery performance. Average cross-track miss distance when flying manually was 16.4 feet in a random-wind condition, and 30.9 feet when operating at 6000 feet. When the factors were combined, an average cross-track miss distance of 43.7 feet was recorded. Similarly an average of 8.7 feet (wind) and 11.1 feet (6000 feet) may be compared to an average of 22.8 feet when operating on autopilot under the combined wind/altitude conditions.

Workloads in terms of missed lights were comparable to those recorded for combination trials of the initial series. The 41.7 percent (manual flight control) and 26.3 percent (autopilot) (Table 20) accurately reflect the increased demand placed on the pilot in the more severe operating environment.

133

TASK PRIORITIES

The priority which the pilot assigns to the various tasks resident in the weapon delivery trial was an additional variable that was considered in the supplemental trial series. During the wind and altitude trials, the pilot was asked to vary his task priorities through each set (for a total of four sets) of 10 trials as follows:

Number of Trials	Primary	Secondary
4	Weapon Delivery	Light Detection
4	Light Detection	Weapon Delivery
2	Both	Both

Figures 27 through 30 are plots of 40 runs (some data points represent two runs) each for the four pilot subjects. Each set of 40 includes 20 runs in which the altitude was fixed at 1000 feet and random wind was applied, and 20 runs in which the altitude was raised to 6000 feet. In addition, for 16 runs the pilot was instructed to concentrate primarily on weapon delivery and secondarily on his side task. For another 16 runs the order was reversed; the pilot was instructed to concentrate primarily on the side task and secondarily to weapon delivery. In the remaining eight runs, the pilot subjects were instructed to divide their attention equally between the two tasks. In all cases the pilots were instructed to try to maintain a constant total effort. It was intended by this means to develop empirically a relationship between pilot workload and pilot performance. From the scatter in the data in Figures 27 through 30, no such relationship is evident. It is suspected that, although explicit instructions were given, the pilot subjects have a desire to perform well in weapon delivery that is difficult to subordinate. The data for test subject 2 exhibits to a slight degree the expected relationship between workload and performance.

What is evident in the data, however, is that whatever the skills of the individual subjects, the automatic mode is an equalizer providing consistent steering accuracy under 25 feet. The manual steering results reflect the individual skills of the pilots.

THIS REPORT HAS BEEN DELIMITED
AND CLEARED FOR PUBLIC RELEASE
UNDER DOD DIRECTIVE 5200.20 AND
NO RESTRICTIONS ARE IMPOSED UPON
ITS USE AND DISCLOSURE.

DISTRIBUTION STATEMENT A

APPROVED FOR PUBLIC RELEASE;
DISTRIBUTION UNLIMITED.